# THE INFLUENCE OF HIGH MEAN STRESS AND HIGH R RATIO ON THE FATIGUE BEHAVIOR OF COMPONENTS

By
Shugen Peng

A Thesis submitted to
the Faculty of Graduate Studies
In Partial Fulfillment of the Requirements for the Degree of

MASTER OF SCIENCE

Department of Mechanical and Manufacturing Engineering
University of Manitoba
Winnipeg, Manitoba


The Faculty of Graduate Studies
500 University Centre, University of Manitoba
Winnipeg, Manitoba R3T 2N2

THE UNIVERSITY OF MANITOBA

FACULTY OF GRADUATE STUDIES

*****

COPYRIGHT PERMISSION

# THE INFLUENCE OF HIGH MEAN STRESS AND HIGH R RATIO ON THE FATIGUE BEHAVIOR OF COMPONENTS

BY

Shugen Peng

A Thesis/Practicum submitted to the Faculty of Graduate Studies of The University of Manitoba in partial fulfillment of the requirement of the degree

Master Of Science

# ABSTRACT

This thesis investigates the influence of high mean stress and high R ratio on the fatigue behavior of components. Specifically, high tensile mean stress fatigue tests for R ratios of 0.7 and 0.8 were first conducted on notched, $K_t = 3.64$, axial loaded SAE 1045 steel specimens with hardness Rc 37. The abilities of the conventional stress and strain life methods of fatigue analysis to predict the fatigue life of the test specimens were subsequently evaluated. To do so, fully reversed fatigue tests were additionally conducted on smooth fatigue specimens to determine the cyclic material properties necessary for the application of the life prediction methods. Finally, fractographic examinations were conducted on the fractured notched specimens using scanning electron microscopy.

During testing, the cyclic creep was observed and increased with increasing mean stress. The fracture surfaces of the higher mean stress, or shorter fatigue life samples, were characteristic of monotonic failures while the longer life samples showed indications of fatigue. Fatigue life calculations based on the Stress-Life models were up to four orders of magnitude in error. However, when either Neuber's rule or the Equivalent Strain Energy Density method were used in conjunction with either the Morrow or Smith-Watson-Topper Strain-Life models to calculate the fatigue life of the notched specimens, the maximum error was one order of magnitude.

ACKNOWLEDGEMENTS

I wish to thank my parents, my aunt family and Peng Li for their endless encouragement and support during this long journey.

I would also like to thank:

Paul Krueger for his help on adaptor collet design and load frame setup.

Don Mardis and Lin Xiao for their assistance on specimen design and experimental setup.

Irwin Penner for machining the specimens and adaptor collets.

John Van Dorp for his help on fractographic examinations.

Robert Thom for his seasoned training in stain gauge installation and data acquisition system operation and programming.

Tim Schmidt for providing technical support for the optical deformation measurement device.

In addition, all those individuals and friends who helped on this research are also acknowledged.

Special thanks to Professors Nipon Rattanawangcharoen and Christine (Qiong) Wu for for being on the thesis committee. Special thanks are extended to Professor R. Jayaraman for his seasoned suggestions for this thesis.

Finally, special thanks to Dr. Meera N.K. Singh for her valuable guidance, motivation and encouragement for this research program.

TABLE OF CONTENTS

# LIST OF TABLES

LIST OF FIGURES

# CHAPTER ONE

# INTRODUCTION

This chapter first gives a general overview of and the motivation for the research conducted. The objectives of this research, the outline of the research conducted to meet the objectives, and the scope of the thesis are subsequently presented.

## 1.1 Background

Engineering components are often subjected to fluctuating or fatigue type loads in service. These cyclic loads can result in component failure at an applied load level below that which would result in the component material reaching its ultimate strength under monotonic loading. Such fatigue failures are common, are often associated with substantial economic loss, and pose a serious compromise to human safety. As such, the fatigue behavior of materials has been the topic of extensive research for over a century and components used in fatigue applications are designed based on developed fatigue design methodologies. These methodologies aim to predict the number of service loading cycles a component can withstand before an associated defined failure occurs.

One of the most fundamental factors that influences the fatigue behavior of a component made of a given material is the magnitude and configuration of the applied loading cycle since it influences the fluctuating stress state within the component. The most basic loading cycle is shown in Fig. 1.1, where a constant amplitude fluctuating load results in a uniaxial nominal maximum stress, $S_{max}$, and minimum stress, $S_{min}$. The mean stress, $S_m$, the alternating stress, $S_a$, and the stress ratio, R, are defined respectively on the basis of the maximum and minimum stress as:

$$S_m = \frac{S_{max} + S_{min}}{2}, \tag{1.1}$$

$$S_a = \frac{S_{max} - S_{min}}{2}, \tag{1.2}$$

and

$$R = \frac{S_{min}}{S_{max}}. \tag{1.3}$$

It is well known that the mean stress has a substantial influence on the fatigue behavior of a component. That is, in components made of conventional engineering materials, compressive mean stresses generally improve fatigue life while tensile mean stresses have a detrimental effect on fatigue life. This is shown in Fig. 1.2, where the alternating stress is plotted against the number of cycles identical components can withstand before failure, $N_f$, when cycled at different mean stresses. Since components (such as pressure vessels, bolts, gear teeth, etc.) are often either exposed to a mean stress due to the applied loading configuration or due to residual stresses induced during manufacturing, fatigue design methodologies incorporate relations that account for the mean stresses experienced in service.

Although mean stress correction relations are well established, they have been largely validated against data from laboratory tests conducted on fatigue specimens subjected to low to moderate mean stresses and R ratios. That is, for mean stresses below sixty percent of the materials ultimate strength, $S_u$ (i.e. $S_m < 0.6S_u$), and R ratios less

than 0.5 [1]. Figure 1.3 illustrates that for higher mean stresses and R ratios, there is little fatigue data available.

It should be noted that Eqs. (1.1) and (1.3) imply that a high mean stress and high R ratio loading cycle has a low alternating stress component. A typical such loading cycle is shown in Fig. 1.4. Although in many applications loading cycles fall within the range in which the fatigue design methods have been validated, there are many common applications where components are subjected to high mean stresses and high R ratios. Some of such specific industrial applications include pre-tightened bolts, airplane wings and turbine engine blades. More generally, however, high mean stresses may be experienced at a geometric discontinuity in any component. That is, although nominal mean stresses may be low, due to the effect of the associated stress concentration, local mean stresses may be higher than the aforementioned limit of model validity.

Components exhibit different fatigue behavior under high mean stresses than they do at lower mean stresses. This was initially discovered by Bell and Benham [2] who tested stainless steel (18Cr-9Ni) specimens at various stress ratios ranging from R= -1 to 0.91 under cyclic axial loads. In their work, they tested both smooth specimens and those that contained a geometric discontinuity (notch). Their results, shown in Figs. 1.5-1.6 for smooth and notched specimens respectively, indicate that for a given $S_{max}$, as the R ratio (and thus from Eqs. (1.1) and (1.3), the mean stress) increases, the slopes of the nominal stress versus cycles to failure plots become shallow. This implies that at higher R ratios, a small change in the maximum stress results in a vast difference in fatigue life. It was also indicated in [2] that cyclic creep occurred at high R ratios in both the smooth and notched specimens subject to high R ratio loading. The cyclic creep resulted in a ductile rupture

rather than a fatigue failure.

The concept of cyclic creep is detailed in [3] where it is emphasized at intermediate to high stress levels under load control test conditions, cyclic creep or ratcheting, can occur in the presence of mean stresses. Figure 1.7 shows the cyclic creep/ratcheting of a SAE 1045 steel rod subjected to a tensile mean stress [4]. It should be noted that since ratcheting increases the mean strain values, it results in an increase in the detrimental effects of tensile mean stress on the fatigue life of components. It should be noted that conventional fatigue life prediction models do not have the ability to account for cyclic creep or ratcheting since this phenomenon not only depends on material properties but also on loading mode. Furthermore it is unclear, even for a given material, what stress level or R ratio results in cyclic creep, and it is thus difficult to incorporate into fatigue life prediction models.

## 1.2 Motivation and Objective

Since the conventional fatigue life prediction models have not been sufficiently validated for R ratios greater than 0.7, the Society of Automotive Engineers Fatigue Design and Evaluation, SAE FD&E, committee recently embarked on a cooperative research effort to study the fatigue behavior of materials under high mean stress and high R ratios. This work is part of this broad SAE FD&E high mean stress research program.

The objective of this research is to investigate the influence of high mean stress and high R ratio on the fatigue behavior of components. The investigation is carried out by analyzing the behavior of notched fatigue samples when subjected to high mean stress cyclic loading and examining their fracture surfaces post failure. The investigation

additionally assesses the ability of existing fatigue life prediction models to predict the fatigue life of components subjected to high mean stress, high R ratio loading.

## 1.3 Outline of This Research

To meet the objectives, the following tasks are carried out in this thesis:

- Conduct a critical literature review of existing fatigue life prediction models.
- Experimentally evaluate fatigue behavior under high mean stress and high R ratios.
  - Determine material properties needed in analytical fatigue life calculations.
  - Perform high mean stress fatigue tests on sharply notched specimens.
- Perform fractographic analysis of the fractured specimens after high mean stress cyclic loading to investigate the fatigue crack nucleation and propagation morphology.
- Calculate the fatigue lives of the notched specimens using known life prediction models and compare them to the experimental data obtained.

## 1.4 Scope of Thesis

In Chapter Two, fatigue life prediction methods are reviewed with specific reference to high mean stress applications. In Chapter Three, the experimental facilities, setup, and procedures are detailed. In Chapter Four, the experimental results are given. In Chapter Five, an evaluation of the life prediction methods is performed by comparing the calculated fatigue lives with experimental data. In Chapter Six, conclusions and recommendations for future research are presented.

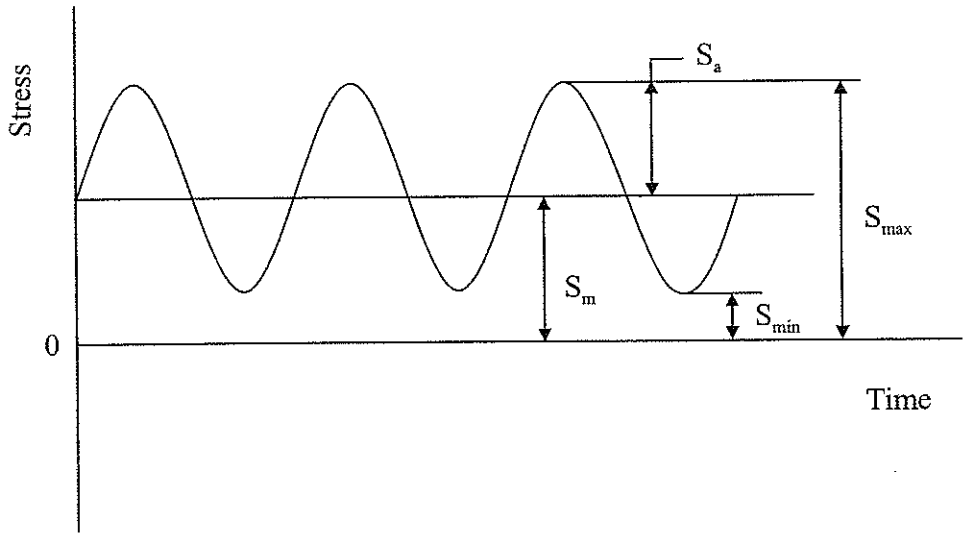


Figure 1.1 Nomenclature for Constant Amplitude Loading

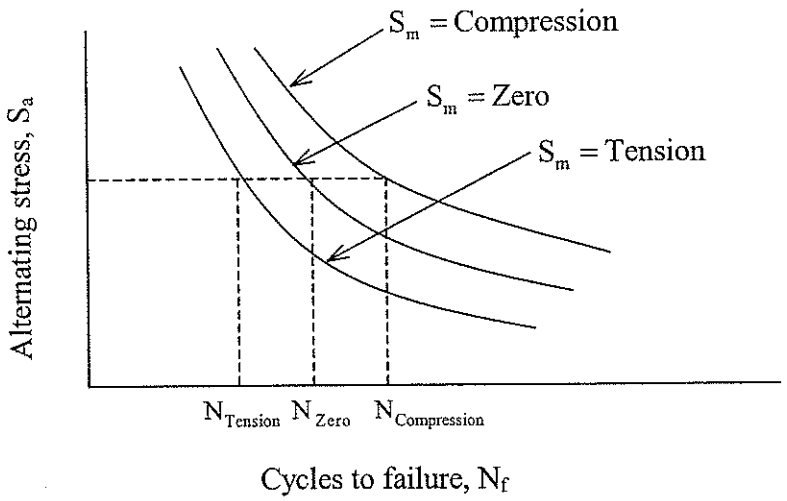


Figure 1.2 Effect of Mean Stress on Fatigue Life

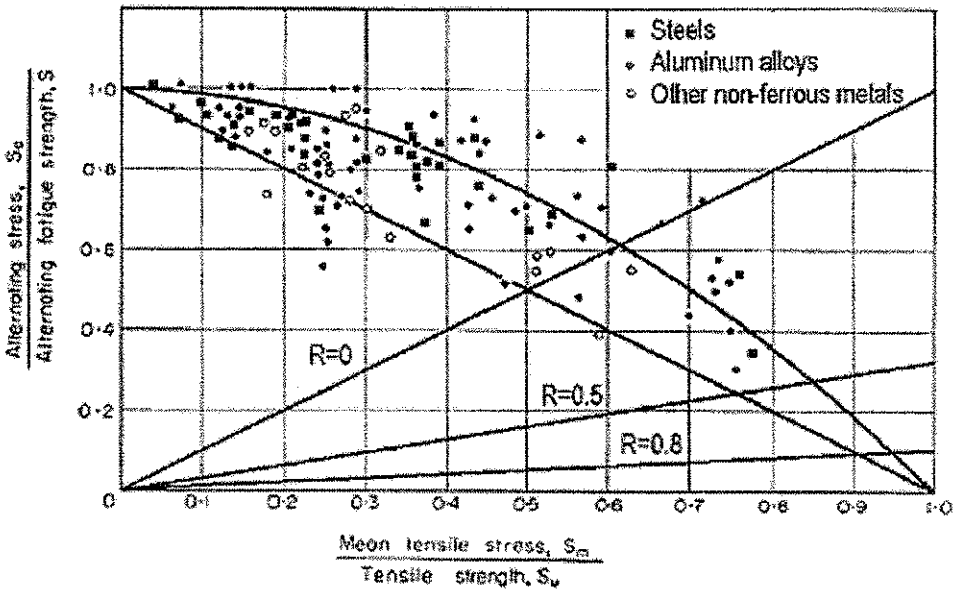


Figure 1.3 A Compilation of Mean Stress Experimental Research at Different R Ratios [1]

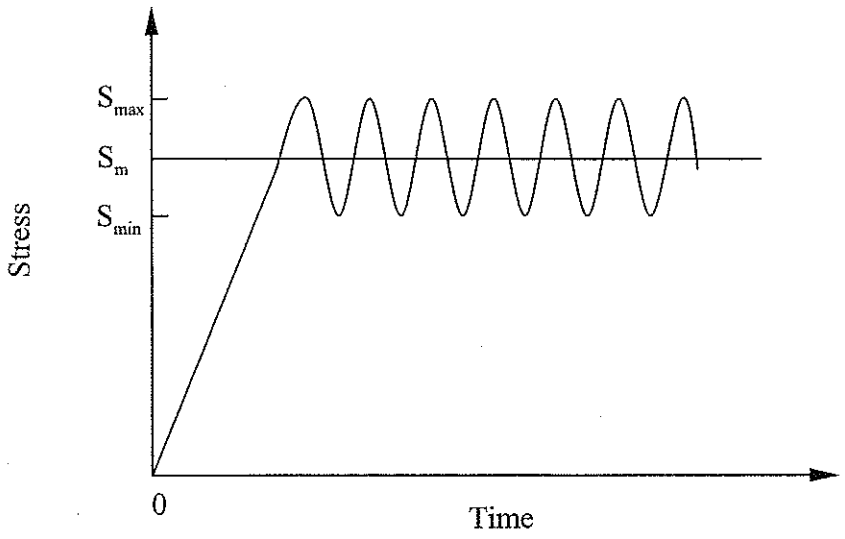


Figure 1.4 A Typical Load Pattern of High Mean Stress and High R Ratio

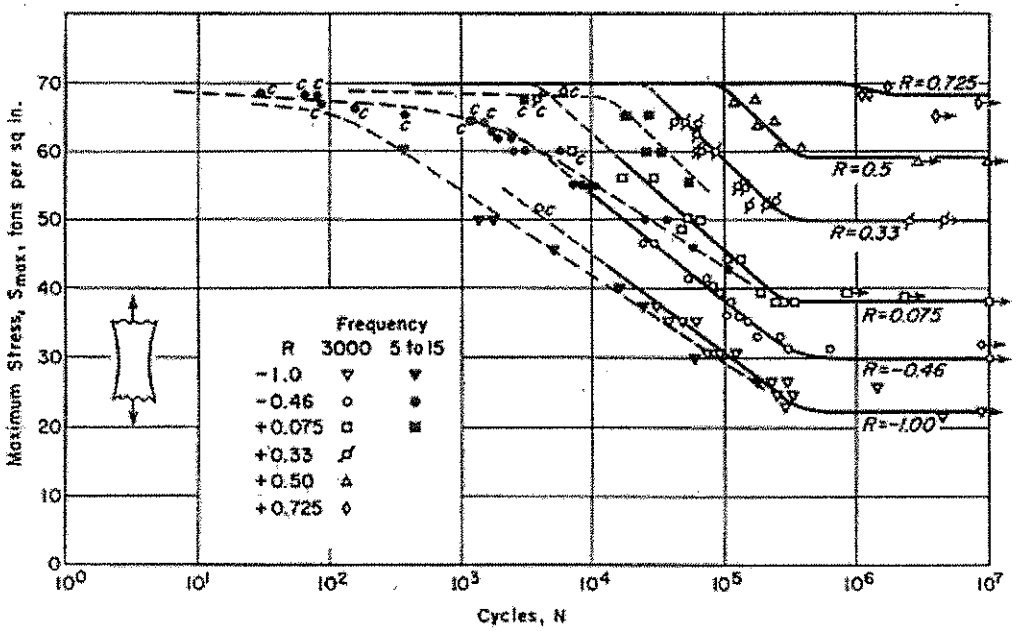


Figure 1.5 Effects of R Ratios on Smooth Specimens of Cr-Ni Stainless Steel [2]

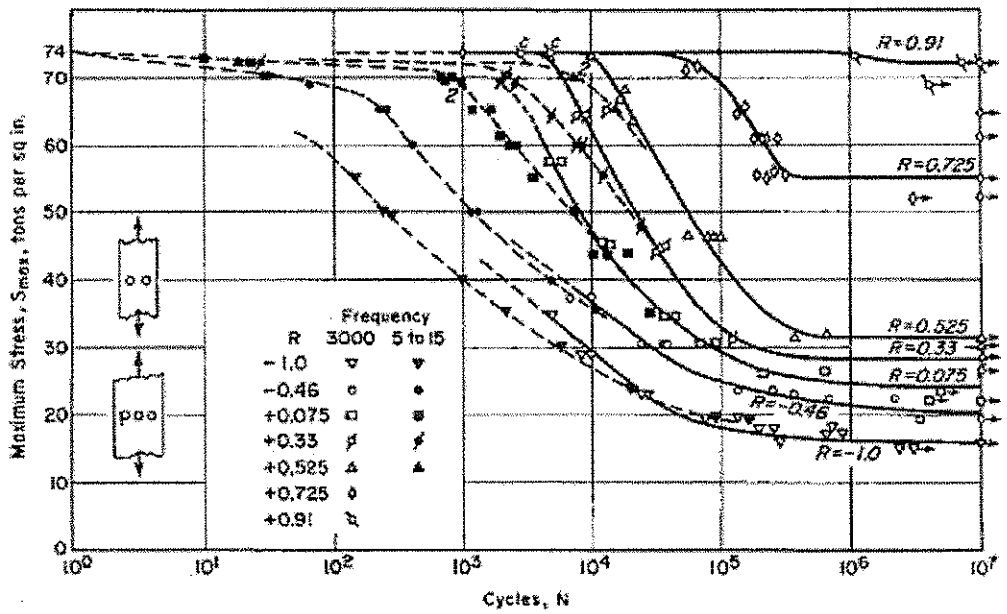


Figure 1.6 Effects of R Ratios on Notched Specimens of Cr-Ni Stainless Steel [2]

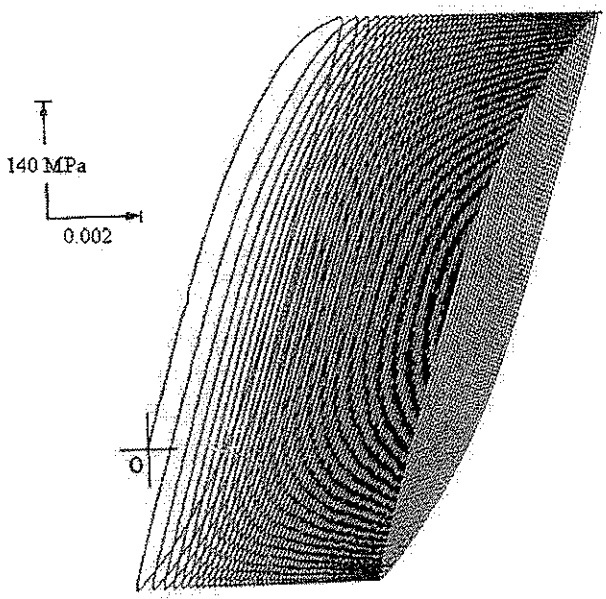


Figure 1.7 SAE 1045 Steel Cyclic Creep/Ratcheting Under Tensile Mean Stress [4]

# CHAPTER TWO

# FATIGUE LIFE PREDICTION MODELS

There are three methods used in fatigue analysis to predict the life of components subjected to cyclic loads. These include the nominal stress-life (S-N), the local strain-life (ε-N), and the linear elastic fracture mechanics (not considered in this research) approaches. In this Chapter, the S-N and the ε-N approaches to fatigue analysis are first detailed. The governing relations that include conventional methods of accounting for moderate mean stresses are presented. Additionally, more recent analytical and experimental research that has, in the realm of these methods, addressed components in the high mean stress and high R ratio regime, is detailed. A summary of the literature presented is given in Section 2.3.

## 2.1 Stress-life (S-N) Models

The stress-life, S-N, method of fatigue analysis is used in high-cycle ($>10^4$ or $10^5$ cycles) fatigue applications, where stresses generally fall within the elastic range of the material. Basic fatigue data in the high-cycle life range can be conveniently displayed on a plot of the nominal experimental cyclic stress level versus the logarithm of number of cycles to failure or life. In 1910, Basquin [5] observed that stress-life data could be plotted linearly on a log-log scale and correlated using:

$$S_a, S_{Nf} = A\left(N_f\right)^B, \tag{2.1}$$

where $S_a$ is the amplitude of the alternating stress, $S_{Nf}$ is the fully reversed ($R = -1$) fatigue strength at $N_f$ cycles, A is the coefficient and represents the value of $S_a$ or $S_{Nf}$ at one cycle, and B is the fatigue strength exponent, which is the slope of the log-log S-N curve. Although S-N curves are generally obtained at fully reversed loading conditions where the mean stress is zero, many engineering components are subjected to nonzero mean stresses in service. In order to determine the fatigue life of smooth (unnotched) mechanical components under nonzero mean stresses, several models have been developed. The most commonly used equations that correlate the tensile mean stress with the fatigue strength for smooth specimens at the infinite fatigue life or a long life of about $10^6 - 10^8$ cycles include the Modified Goodman, Gerber, and Morrow [3]. These equations are given as:

Modified Goodman

$$\frac{S_a}{S_f} + \frac{S_m}{S_u} = 1, \tag{2.2}$$

Gerber

$$\frac{S_a}{S_f} + \left(\frac{S_m}{S_u}\right)^2 = 1, \tag{2.3}$$

Morrow

$$\frac{S_a}{S_f} + \frac{S_m}{\sigma_f} = 1. \tag{2.4}$$

In Eqs. (2.2)-(2.4), $S_f$ is the completely reversed fatigue strength, $S_u$ is the material

ultimate strength, and $\sigma_f$ is the true fracture strength. The Modified Goodman and Morrow equations can be extrapolated into the compressive mean stress region since they predict that the compressive mean stresses at long lives are beneficial. However, the Gerber equation incorrectly predicts a detrimental effect of a compressive mean stress on the fatigue life of a component. The fatigue lives of smooth specimens can be predicted by substituting the Basquin equation (Eq. (2.1)) for $S_f$ in the mean stress correction models (Eqs. (2.2)-(2.4)).

Most mechanical components contain some kind of geometrical discontinuity, such as keyways, holes and splines (notches). The maximum local stress at the discontinuity, $\sigma_{max}$, can be many times higher than the nominal stress, $S$, in the member. The elastic stress concentration factor, $K_t$, is used to relate the maximum local stress to the nominal stress in an ideally elastic member. It is defined as,

$$K_t = \frac{\sigma_{max}}{S}. \tag{2.5}$$

The elastic stress concentration factor is only dependent on the geometry and mode of loading. In the stress-life method, the fatigue strength of a notched member cannot be determined only by the elastic stress concentration factor since a stress gradient and localized plastic deformation may be present at the notch root [3]. The ratio of smooth to notched fatigue strength, called fatigue notch factor, $K_f$, is defined as,

$$K_f = \frac{\text{Smooth specimen fatigue strength}}{\text{Notched specimen fatigue strength}}. \tag{2.6}$$

The fatigue notch factor can be determined by Peterson's formula [6] as,

$$K_f = 1 + \frac{K_t - 1}{1 + a/r}, \tag{2.7}$$

where a is material constant, and r is the radius of the notch root.

Modifications are needed to the aforementioned empirical mean stress correction models (Eqs. (2.2)-(2.4)) developed for smooth specimens to predict the fatigue lives of notched members. Since the fatigue crack initiation process is a local phenomenon, and any stress concentration can be very detrimental, the permissible nominal alternating stress is normally reduced by dividing it by the fatigue notch factor. A simple approach for estimating the long life fatigue strength of a component that is subjected to a tensile or compressive mean stress involves dividing the fatigue strength by the fatigue notch factor in the Modified Goodman equation as,

$$\frac{S_a}{(S_f/K_f)} + \frac{S_m}{S_u} = 1. \tag{2.8}$$

The obvious shortcoming of Eq. (2.8) is that it does not incorporate non-linear behavior at the notch tip upon material yielding. Therefore, the modification is only valid when the notch root material is in the elastic range.

Equations (2.1)-(2.8) represent the conventionally used relations that define the stress-life approach to fatigue analysis. However, as stated in the introduction, these relationships have only been experimentally validated for moderate mean stress and R ratios applications for smooth and notched components. There have been few attempts to incorporate the effect of high mean stresses into the S-N approach to fatigue analysis. Cook [7] and Gunn [8] proposed two alternate life prediction models that account for the local plasticity that is associated with the presence of high mean stresses in notched members. Cook's [7] equations for high mean stress are given as:

$$S_a = \frac{S_f(S_u - K_f S_m)}{K_f S_u} \quad 0 \le S_m \le S_m^B,$$

$$S_a = \frac{S_f(S_y - S_u)}{K_f(S_f - S_u)} \quad S_m^B < S_m < S_m^{B'}, \tag{2.9}$$

and

$$S_a + S_m = S_y \quad S_m^{B'} \le S_m \le S_u.$$

In Eq. (2.9), $S_y$ is the material yield strength,

$$S_m^B = \frac{S_u(S_f - S_y)}{K_f(S_f - S_u)},$$

and

$$S_m^{B'} = S_y - \frac{S_f(S_y - S_u)}{K_f(S_f - S_u)}.$$

Gunn's [8] model for high mean stress is given as:

$$S_a = \frac{S_f}{K_t}\left[1-\left(\frac{K_t S_m}{S_u}\right)^{4/3}\right] \quad 0 \le S_m \le S_m^{'},$$
$$S_a = \frac{S_f}{K_t}\left[1-\left(\frac{S_y - K_t S_a}{S_u}\right)^{4/3}\right] \quad S_m^{'} \le S_m \le S_y. \tag{2.10}$$

In Eq. (2.10), $S_m^{'}$ is the intersection of the curve of Gunn's equations and the straight line joining the points $(S_y/K_t)$ plotted on both axes shown in Fig. 2.1.

A plot of the mean stress models including the Modified Goodman for smooth components, and the Modified Goodman, Gunn and Cook models for notched components is shown in Fig. 2.1. As can be seen from the figure, Cook's equations divide the S-N curve into three distinct portions . In the first portion, the slope of line AB is the same as the Modified Goodman equation (Eq. (2.8)) for a notched member before the onset of local yielding when $K_f(S_m + S_a) = S_y$ at B. The second portion, $BB^{'}$, implies that Cook's equations assume that a further increase in mean stresses after the onset of local yielding has no effect on the fatigue strength until point $B^{'}$, where point $B^{'}$ denotes gross yielding when $S_m + S_a = S_y$.

Before local yielding, the first part of the Gunn's model is obtained from smooth specimen data by reducing both the stress amplitude and the mean stress by the elastic stress concentration factor. In Gunn's model, it is assumed that the range of stress does not change with the increase in mean stress after local yielding has occurred. This

assumption is modelled in the second portion of Eq. (2.10), which is similar to Cook's model, and the exponent 4/3 is taken to consider the work-hardening effect.

Burguete and Patterson [9] conducted tests on bolts under different levels of mean stress and compared the test results to those predicted by Cook and Gunn's models. It was found that these models provided a good correlation with the test data when the mean stresses were below the material yield strength.

Recently, Vantiger, et.al.[10-12] investigated the fatigue behavior of SAE 1045 steel rods subjected to high tensile mean stress for unnotched, mildly notched, and sharply notched test specimens with three different hardness Rc 10, 37 and 50. All fatigue tests were run in load control using a sinusoidal waveform between 25 and 30 Hz at R ratios of 0.8 and 0.9. In their work, the conventionally used mean stress correction models (Eqs.(2.2)-(2.4)) were assessed for their ability to model high mean stress conditions. Slightly modified versions of the Modified Goodman, Gerber, and Morrow equations were proposed and used with the Basquin equation to determine the fatigue lives of their test specimens. Specifically, they observed that the values of $S_{max}$ and $S_m$ often exceeded the unnotched ultimate tensile strength due to the notch strengthening effect. On that basis, they proposed that the ultimate stress should be replaced by the notched specimen ultimate strength in the Modified Goodman and Gerber equations to calculate the fatigue lives of notched specimens. The calculated fatigue lives based on the proposed mean stress models were inaccurate by up to 5 orders of magnitude when compared to the actual lives, and thus were not meaningful. It should be noted that the parameters in Basquin's equation were taken from published testing data which was not strictly applicable to the testing material.

Other research studies aimed at evaluating the effect of high mean stress have not evaluated the fatigue life prediction models but rather presented high mean stress fatigue data. As mentioned in Chapter One, the earliest research work about high mean stresses was done by Bell et. al. [2] in 1962. More recently, Morrissey and McDowell [13] performed high cycle fatigue tests on Ti-6Al-4V smooth specimens at a range of loading frequencies for three different stress ratios, i.e. 0.1, 0.5 and 0.8. It was observed that cyclic creep was clearly present at R=0.8. Their fractographic analyses further showed that the fracture mode is quite different for R=0.5 compared to that for R=0.8. Specifically, at R=0.5 fatigue crack growth followed by ductile tearing and shear lip formation were observed as the cycles progressed. However, fracture surfaces at R=0.8 showed strong evidence of ductile void growth and initiation. The differences in the two fracture modes may have been caused by cyclic creep/ratcheting. Another experimental investigation involving high mean stresses was conducted for Ti-6Al-4V by Maxwell and Nicholas [14]. In their study, they concluded that the maximum stress is a critical parameter in fatigue design for high R ratios (R>0.5) and that the fatigue failure mode was similar to that in a creep or sustained load test at very high R ratios.

## 2.2 Strain-Life (ε-N) Models

Machine components are often subjected high cyclic loads that induce significant amounts of deformation during each cycle. Since this loading is associated with short lives, failure under this high loading is commonly referred to as low-cycle fatigue. In this case, fatigue behavior is best described in terms of strain.

The ε-N approach to fatigue analysis can explicitly account for the plastic

deformation that may occur at a stress raiser or notch and has thus become increasingly popular to predict the number of cycles a component can withstand before a crack will initiate at a notch root.

Using the strain-life approach, fatigue life predictions are made using a two-step process. Firstly, the elastic-plastic strain and stress history at a components critical location is determined. The second step is to substitute the calculated local stresses and strains into a strain-life fatigue failure model to calculate the number of cycles to crack initiation. The methods used to determine the notch root elastic-plastic strain and stress history are first presented in Section 2.2.1. The ε-N failure theories are subsequently presented in Section 2.2.2.

### 2.2.1 Notch Root Elastic-Plastic Strain-Stress Analysis

As previously mentioned, when a notched component is loaded, a stress gradient arises in the plane of the notch, with the highest stress being located at the notch root. Furthermore, the deformation of the notch root is constrained by the lower stressed bulk material away from the higher stressed material at the notch root. In response to this constraint, off-axis stresses are generated at the notch root. As a result, even when a uniaxial load is applied to a notched body, a non-uniform triaxial stress field, as shown in Fig. 2.2, arises in the plane of the notch. In this case, at the notch root, the state of stress is biaxial since the stress normal to the traction free surface is zero. Figure 2.3 shows this stress state on an element taken from the notch root of a loaded body. Referring to the coordinate system shown in the figure, the corresponding stress and strain tensors can be represented respectively as:

$$\sigma_{ij} = \begin{bmatrix} 0 & 0 & 0 \\ 0 & \sigma_{22} & 0 \\ 0 & 0 & \sigma_{33} \end{bmatrix}, \tag{2.11}$$

and

$$\varepsilon_{ij} = \begin{bmatrix} \varepsilon_{11} & 0 & 0 \\ 0 & \varepsilon_{22} & 0 \\ 0 & 0 & \varepsilon_{33} \end{bmatrix}. \tag{2.12}$$

Equations (2.11) and (2.12) indicate that when a body is subjected to a uniaxial load, there are five unknowns (two stresses and three strains) at the notch root. The strain-life method of fatigue design necessitates the knowledge of these five components throughout a loading history for application. Unlike the stress-life method of fatigue analysis, inherent in the strain-life method is the relaxation of the assumption of local elastic behavior. As such these parameters cannot be determined by simply applying the equations of elasticity.

There are three methods of determining the elastic-plastic notch root strains and stresses throughout a components loading history. These include numerical methods such as the finite element analysis (FEA), experimental measurements, and simplified analytical techniques. Comparing the three methods, experimental measurements are not only time-consuming but also often constrained by the component geometry and testing equipment. For example, it is impossible to mount the traditional strain gauges at the notch root of sharply notched samples. Numerical techniques, such as the finite element

method, can give good accuracy for nonlinear stress-strain analyses, but are often expensive and time-consuming.

All of the simplified models for elastic-plastic notch analysis proposed to date are based on a comparison between the notch tip behavior in two geometrically identical bodies that have the same elastic properties illustrated in Fig. 2.4. These bodies are further assumed to be subjected to the same external loads. The difference between the bodies is that one is made of an elastic material, with the other, of an elastic-plastic material. By making such a comparison, the notch root behavior in the elastic-plastic body can be determined from a relatively simpler elastic analysis. The approximate analytical models can be easily applied in a nonlinear stress-strain analysis so long as the geometry, loading condition, and material stress-strain curve are known. Simplified analytical techniques thus give the ability to provide simple analytical calculations in design.

Early researchers into simplified analytical techniques made assumptions regarding to the state of stress in order to reduce the number of required equations to define the notch root parameters. These included the assumption of plane stress and plane strain. The plane stress assumption is particularly applicable to thin plates where the associated state of stress at a notch root is uniaxial due to the lack of lateral constraint. On the other hand, the plane strain assumption is made when the lateral strain can be assumed negligible, as in the case of a thick plate. Referring to the coordinate system shown in Fig. 2.3, the stress and strain states at the notch root in a uniaxially loaded member under the plane stress and plane strain assumptions are given respectively as:

Plane Stress

$$\sigma_{ij} = \begin{bmatrix} 0 & 0 & 0 \\ 0 & \sigma_{22} & 0 \\ 0 & 0 & 0 \end{bmatrix} \quad \varepsilon_{ij} = \begin{bmatrix} \varepsilon_{11} & 0 & 0 \\ 0 & \varepsilon_{22} & 0 \\ 0 & 0 & \varepsilon_{33} \end{bmatrix} \tag{2.13}$$

Plane Strain

$$\sigma_{ij} = \begin{bmatrix} 0 & 0 & 0 \\ 0 & \sigma_{22} & 0 \\ 0 & 0 & \sigma_{33} \end{bmatrix} \quad \varepsilon_{ij} = \begin{bmatrix} \varepsilon_{11} & 0 & 0 \\ 0 & \varepsilon_{22} & 0 \\ 0 & 0 & 0 \end{bmatrix} \tag{2.14}$$

As can be seen from Eqs.(2.13)-(2.14), the number of unknown notch root parameters is reduced by one relative to the case where no assumption is made. The four remaining notch root parameters therefore can be found by defining four mechanical behavioral equations. Three of the required equations are generally defined by the material constitutive relations. In light of the application of the simplified analytical techniques, the fourth equation is defined by making the previously described comparison illustrated in Fig. 2.4.

The most frequently used approximation model that relates the notch root elastic-plastic strains and stresses to the nominal values was first proposed by Neuber [15] in 1961. Neuber's rule, originally derived for a prismatic body subjected to pure shear loading, is commonly expressed as,

$$K_t^2 = K_\sigma K_\varepsilon = \frac{\sigma}{S}\frac{\varepsilon}{e}, \tag{2.15}$$

where $K_\sigma$ and $K_\varepsilon$ are the stress and strain concentration factors respectively, $\sigma$ is the local stress, $S$ is the nominal stress, $\varepsilon$ is the local strain, and $e$ is the nominal strain. If the material away from notch is elastic then by Hooke's law, $e = S/E$, and the relation that correlates the nominal elastic stress with the local stress and strain can be found using Eq. (2.15) as:

$$\sigma\varepsilon = \frac{(K_t S)^2}{E}. \tag{2.16}$$

Neuber's rule also can be written in the form,

$$\sigma^e\varepsilon^e = \sigma^N\varepsilon^N, \tag{2.17}$$

where the superscript "e" and "N" stand for the local stress and strain components determined from the ideal elastic material law and real material law respectively. The physical meaning hidden in Eq. (2.17) is that the actual total strain energy density (the sum of the strain energy density and the complementary strain energy density) at the notch tip in an elastic-plastic body is equal to that which would be obtained if the material were to remain elastic as the external loads were applied. A graphical representation of Neuber's rule is illustrated in Fig. 2.5. For two identical notch bodies, as shown in Fig. 2.4, Neuber's rule assumes that the total strain energy density at the notch tip of the right hand elastic-plastic body is identical with the ideal elastic body under the same loading conditions.

Combining Eq. (2.16) with the material constitutive law in a Ramberg-Osgood form, the notch tip elastic-plastic strain and stress can be determined for given stress concentration factor and nominal stress by,

$$\begin{cases} \dfrac{\sigma^2}{E}+\sigma\left(\dfrac{\sigma}{K}\right)^{1/n}=\dfrac{(K_t S)^2}{E} \\ \varepsilon=\dfrac{\sigma}{E}+\left(\dfrac{\sigma}{K}\right)^{1/n} \end{cases} \tag{2.18}$$

In Eq.(2.18), n is the strain hardening exponent, and K is the strength coefficient. These parameters are obtained by linearly fitting the true stress versus the true plastic strain curve in log-log coordinates. The strength coefficient is taken as the stress coordinate at a true plastic strain of unity. The strain hardening exponent is the slope of the linear fit line. It should be noted that the Ramberg-Osgood relation is valid up to the ultimate strength since only the experimental data between the yield strength and the ultimate strength can be used to generate the relation to avoid the necking effect.

Topper et. al.[16] extended Neuber's rule to make it applicable to cyclic loading. In their work, the monotonic stress-strain curve is replaced by the cyclic stress-strain curve and the stresses and strains are replaced by their corresponding amplitudes.

Neuber's rule has been shown to provide a good agreement with measurements for thin sheets and plates (e.g. plane stress) and conservatively predicts higher strains than measured values for bodies in plane strain [3].

In 1981, Molski and Glinka [17] proposed an alternate approximation model, the equivalent strain energy density (ESED) method, for determining the elastic-plastic notch

root strain-stress histories. The method states that the strain energy density at the notch tip in an elastic-plastic body can be approximated by that in an elastic body if the plastic zone at the notch root in the elastic-plastic body is surrounded by an elastic stress field. It has been shown [17] that this relationship has produced good results even after the net section has yielded. The ESED method can be expressed in terms of strains and stresses as,

$$\frac{1}{2}\sigma^e\varepsilon^e = \int_0^{\varepsilon^E} \sigma^E d\varepsilon^E, \tag{2.19}$$

where superscript "E" refers to the elastic-plastic notch tip strain and stress components as estimated by the ESED method. The Ramberg-Osgood material constitutive law can be used in conjunction with Eq. (2.19) as:

$$\begin{cases} \dfrac{\sigma^2}{E} + \dfrac{2\sigma}{n+1}\left(\dfrac{\sigma}{K}\right)^{1/n} = \dfrac{(K_t S)^2}{E} \\ \varepsilon = \dfrac{\sigma}{E} + \left(\dfrac{\sigma}{K}\right)^{1/n} \end{cases}, \tag{2.20}$$

to determine the axial components of the elastic-plastic strains and stresses. A schematic representation of the ESED method is illustrated in Fig. 2.5. As can be seen from Eq. (2.20), the notch tip elastic-plastic strain and stress can be found knowing the stress concentration factor, the nominal stress, and the material properties. Glinka [17] has also extended the ESED method to address cyclic loading.

By comparing the Eqs. (2.18) and (2.20), the only difference between Neuber's

rule and the ESED method is the factor $\left[2/(n+1)\right]$. Since the strain hardening exponent, $n$, is always less than unity, a smaller stress value at a notch tip is predicted by the ESED method than is by Neuber's rule [3]. Correspondingly, a smaller strain value is obtained by the ESED method, which results in a longer fatigue life prediction than that calculated by applying Neuber's rule.

Equations (2.15) and (2.19) were derived for the plane stress state where a uniaxial stress state dominates at the notch root of a thin plate specimen. In order to take account for the biaxial stress state at the notch tip for a plane strain case, Dowling et al. [18] proposed a modified stress-strain relation. By using the modified stress-strain curve, Neuber's rule and the ESED method can be extended to predict the stress-strain behavior at a notch tip in a body that is under plane strain conditions as:

Neuber's Rule

$$\begin{cases} \dfrac{\sigma^2}{E^*}+\sigma\left(\dfrac{\sigma}{K^*}\right)^{1/n^*}=\dfrac{(K_tS)^2}{E^*} \\ \varepsilon=\dfrac{\sigma}{E^*}+\left(\dfrac{\sigma}{K^*}\right)^{1/n^*} \end{cases}, \tag{2.21}$$

ESED Method

$$\begin{cases} \dfrac{\sigma^2}{E^*}+\dfrac{2\sigma}{n^*+1}\left(\dfrac{\sigma}{K^*}\right)^{1/n^*}=\dfrac{(K_tS)^2}{E^*} \\ \varepsilon=\dfrac{\sigma}{E^*}+\left(\dfrac{\sigma}{K^*}\right)^{1/n^*} \end{cases}, \tag{2.22}$$

where $E^* = E/(1-\nu^2)$, $K^*$ and $n^*$ are the strength coefficient and the strain hardening exponent of the modified stress-strain relation respectively.

In general, a body is somewhere between the plane stress and plane strain states. Therefore, for a body subjected to uniaxial loading, there are five unknown notch tip stress and strain components as identified by Eqs. (2.11) and (2.12). There have been several simplified analytical models proposed for calculating notch root stress-strain histories in bodies subjected to multiaxial loads. These models can be reduced to address bodies subjected to uniaxial loads that are neither in a plane stress nor in a plane strain state. In 1998, Singh [19] proposed incremental ESED and Neuber's rule for calculating notch tip multiaxial stress-strain histories in elastic-plastic components.

In [19], an incremental form of Neuber's rule was proposed. Specifically, it was stated that for a given increment in the applied load, the increment in the total strain energy density at the notch tip in the elastic-plastic body can be approximated by that obtained if the body were to remain elastic throughout the loading history. Incremental Neuber's rule was in [19] mathematically expressed as:

Incremental Neuber's Rule

$$\sigma_{22}^{e}d\varepsilon_{22}^{e} + \varepsilon_{22}^{e}d\sigma_{22}^{e} = \sigma_{22}^{N}d\varepsilon_{22}^{N} + \varepsilon_{22}^{N}d\sigma_{22}^{N}$$
$$\sigma_{33}^{e}d\varepsilon_{33}^{e} + \varepsilon_{33}^{e}d\sigma_{33}^{e} = \sigma_{33}^{N}d\varepsilon_{33}^{N} + \varepsilon_{33}^{N}d\sigma_{33}^{N} \qquad (2.23)$$

In [19], an incremental form of the ESED method was also presented. Specifically, it was stated that for a given incremental in applied load, the corresponding

increment in the strain energy density at the notch tip in an elastic-plastic body can be approximated by that obtained if the body were to remain elastic throughout the loading history. This was expressed mathematically as:

Incremental ESED Rule

$$\sigma_{22}^{e} d\varepsilon_{22}^{e} = \sigma_{22}^{E} d\varepsilon_{22}^{E}$$
$$\sigma_{33}^{e} d\varepsilon_{33}^{e} = \sigma_{33}^{E} d\varepsilon_{33}^{E} \qquad (2.24)$$

Eqs. (2.23) and (2.24) are shown graphically in Fig. 2.6.

Either the incremental Neuber's or ESED method can be used in conjunction with an appropriate constitutive relation for defining the notch root elastic-plastic strains and stresses. For the case of uniaxial monotonic loading where the biaxial stress-state prevails at the notch root, the incremental or the deformation theory of plasticity are applicable on the notch tip element shown in Fig. 2.3, the incremental theory of plasticity can be written as:

$$\Delta\varepsilon_{11} = \left[\frac{-\nu}{E} + \frac{9\gamma}{4\sigma_{eq}^2} S_{11}S_{22}\right]\Delta\sigma_{22} + \left[\frac{-\nu}{E} + \frac{9\gamma}{4\sigma_{eq}^2} S_{11}S_{33}\right]\Delta\sigma_{33},$$
$$\Delta\varepsilon_{22} = \left[\frac{1}{E} + \frac{9\gamma}{4\sigma_{eq}^2} S_{22}^2\right]\Delta\sigma_{22} + \left[\frac{-\nu}{E} + \frac{9\gamma}{4\sigma_{eq}^2} S_{22}S_{33}\right]\Delta\sigma_{33}, \qquad (2.25)$$

and

$$\Delta\varepsilon_{33}=\left[\frac{-\nu}{E}+\frac{9\gamma}{4\sigma_{eq}^2}S_{22}S_{33}\right]\Delta\sigma_{22}+\left[\frac{1}{E}+\frac{9\gamma}{4\sigma_{eq}^2}S_{33}^2\right]\Delta\sigma_{33}.$$

In Eq.(2.25), $S_{ij}$ are the deviatoric components of stress and are defined as,

$$S_{ij}=\sigma_{ij}-\frac{1}{3}\sigma_{kk}\delta_{ij}\quad\begin{cases}\delta_{ij}=0 & i=j\\ \delta_{ij}=1 & i\neq j\end{cases}\quad i,j=1,2,3,$$

and

$$\gamma=\frac{2}{3K_p^{(n)}},\quad K_p^{(n)}=\frac{2}{3}\left[\frac{1}{1/E_p^{t(n)}-1/E}\right].$$

If the material hardening law is descretized into n segments, as shown in Fig. 2.7, then $E_p^{t(n)}$ and $K_p^{(n)}$ represent the tangent and hardening moduli of the portion of the curve where the local equivalent stress lies.

By combining Eqs. (2.25) with (2.23) or (2.24), the incremental stress and strain components at the notch tip can be determined. The yield point can be chosen as the start point to perform the incremental calculation since the stress and strain components can be calculated using Hooke's Law in elastic regime. By progressively adding the incremental elements to the previous stress and strain components, the states of stress and strain at notch root can be obtained for the whole loading history. It should be noted that the form of the constitutive relations presented here permits calculations for monotonic loading only. In [19], a cyclic constitutive model was used to allow for cyclic calculations.

Hoffmann and Seeger [20-21] proposed an alternate approach for estimating multiaxial, elastic-plastic notch strains and stresses. Two steps are required for applying

this method. First a relationship between the applied load and equivalent notch stress and strain is established by an extension of Neuber's rule to multiaxial states of stress and strain by replacing the involved uniaxial quantities $\sigma$, $\varepsilon$ and $K_t$ in Eq. (2.15) by the equivalent quantities $\sigma_{eq}$, $\varepsilon_{eq}$ and $K_{tq}$ obtained from the von Mises or Tresca yield criterion. In the second step, the principle stresses and strains at the notch tip are correlated to the equivalent quantities obtained from the first step by applying appropriate constitutive theory. Two of the six principal stresses and strains have to be known for solving the set of equations obtained in the second steps. Since the stress component normal to the notch root surface is zero, one assumption has to be made concerning another principle stress or strain components.

The proposed equations in [20] of the extended Neuber's rule for a piecewise power material law are given as:

$$\sigma_{eq} = \sigma_y \left(\varepsilon_{eq} E/\sigma_y\right)^{n_1}, \varepsilon_{eq} E \geq \sigma_y, \tag{2.26}$$

$$\varepsilon_{eq} = \frac{\sigma_y}{E} \cdot \left[\frac{K_{tq} S}{\sigma_y}\right]^{2/(1+n_1)}, \sigma_y \leq K_{tq} S \leq K_p \sigma_y, \tag{2.27}$$

and

$$\varepsilon_{eq} = \frac{\sigma_y}{E} \cdot \left[\frac{K_{tq} S}{\sigma_y}\right]^{1/n_1} \cdot K_p^{\frac{n_1-1}{n_1(n_1+1)}}, K_{tq} S \geq K_p \sigma_y. \tag{2.28}$$

In the above equations, $n_1$ is material strain hardening exponent used in material power law, $K_p$ is limit load factor that describes the ratio of the ultimate load, $L_p$, to the yield initiation load for an elastic perfectly-plastic material. The ultimate load can be determined by performing a finite element analysis using an elastic-perfectly plastic material law.

In order to determine the stress-strain histories using Hoffmann and Seeger method for a notched circumferential bar (Fig. 2.2) under uniaxial loading conditions, one assumption is required as mentioned in the second step of the method. Referring to the coordinates in Fig 2.2, it may be assumed that the elastic ratio of the circumferential to axial strain remains constant ($\varepsilon_{33}/\varepsilon_{22} = \text{const.}$) for whole loading history neglecting the plastic effect. Subsequently, by applying the total deformation theory of plasticity and the von Mises yield criterion, the relationship between the equivalent and unknown principal quantities can be expressed [21] as:

$$\frac{\varepsilon_{11}}{\varepsilon_{22}} = -\nu' \frac{1+\alpha}{1-\nu'\alpha}, \tag{2.29}$$

$$\sigma_{22} = \frac{1}{\sqrt{1-\alpha+\alpha^2}}\sigma_{eq}, \tag{2.30}$$

and

$$\varepsilon_{22} = \frac{1-\nu'\alpha}{\sqrt{1-\alpha+\alpha^2}}\varepsilon_{eq}. \tag{2.31}$$

In Eqs. (2.29)-(2.31),

$$\nu' = \frac{1}{2} - \left(\frac{1}{2} - \nu\right)\frac{\sigma_{eq}}{E\varepsilon_{eq}},$$

and

$$\alpha = \frac{\sigma_{22}}{\sigma_{33}} = \frac{\varepsilon_{33}/\varepsilon_{22} + \nu'}{1 + \nu'\,\varepsilon_{33}/\varepsilon_{22}}.$$

Combining Eqs. (2.26)-(2.31), the principal stress and strain components at a notch tip can be determined.

It has been shown for uniaxial loading that Neuber's rule and the ESED method when used together, predict a band within which experimentally determined strains fall. This band has been shown to exist from the point at which the notch root material yields through to general net section yielding. The band, however, is definitely tighter when the local elastic-plastic strains are small, where each individual method yields results close to those experimentally determined. Therefore, for components subject to high mean stress conditions, where the assumption associated with the methods, that of localized plasticity, is violated, Neuber's rule and the ESED method should provide useful results if strain calculations are made using each method and compared.

The extension of Neuber's rule proposed by Hoffmann and Seeger [20-21] was specifically formulated to address the condition of net section yielding. As such, it seems that it would be more applicable to high mean stress applications than those defined in [15] and [17]. It should be noted, however, that they reported over a 30% error in strain values when compared to those obtained from a finite element analysis in the high deformation regime.

### 2.2.2 ε-N Life Prediction Methods

Once the notch root elastic-plastic strains have been determined, they can be used in strain-life models to predict the fatigue life of the component. In 1910, Basquin [5] found that the true stress amplitude could be related to the fatigue life of a component through the following power law equation:

$$\frac{\Delta\sigma}{2} = \sigma_f' \left(2N_f\right)^b, \tag{2.32}$$

where $\frac{\Delta\sigma}{2}$ is the true stress amplitude, $\sigma_f'$ is fatigue strength coefficient, and $b$ is the fatigue strength exponent.

In the 1950s, Coffin [22] and Manson [23] found that the plastic strain amplitude also could be related to the fatigue life by a power law function given as,

$$\frac{\Delta\varepsilon_p}{2} = \varepsilon_f' \left(2N_f\right)^c, \tag{2.33}$$

where $\frac{\Delta\varepsilon_p}{2}$ is plastic strain amplitude, $\varepsilon_f'$ is fatigue ductility coefficient, and $c$ is fatigue ductility exponent.

The total strain amplitude can be related to the fatigue life by combining Eqs. (2.32) and (2.33) given as,

$$\frac{\Delta\varepsilon}{2} = \frac{\sigma_f'}{E}(2N_f)^b + \varepsilon_f'(2N_f)^c . \tag{2.34}$$

Equation (2.34) is the fundamental relation that defines the strain-life method of fatigue analysis. The cyclic fatigue properties in Eq. (2.34) are obtained from fully reversed constant amplitude strain-controlled tests.

As mentioned earlier, components seldom experience fully reversed loadings and mean stresses or strains are usually present. Modifications to the strain-life relations have been made to incorporate mean stress effects. Morrow [24] proposed a model that takes mean stress effects into account by replacing $\sigma_f'$ with $\sigma_f' - \sigma_m$ for the elastic term in Eq. (2.34) as,

$$\frac{\Delta\varepsilon}{2} = \varepsilon_a = \frac{\sigma_f' - \sigma_m}{E}(2N_f)^b + \varepsilon_f'(2N_f)^c , \tag{2.35}$$

where $\sigma_m$ is the local mean stress, $\varepsilon_a$ is the local alternating strain.

The predictions made using Eq. (2.35) are consistent with the observations that mean stress effects are significant at low values of plastic strain, where the elastic strain dominates [25]. The local mean stress is taken to be positive for tensile values and negative for compressive values in Eq. (2.35). The equation correctly predicts that a tensile mean stress is detrimental and compressive mean stress is beneficial to the fatigue life of a component.

Manson and Halford [26] suggested an alternate version of Morrow's mean stress parameter given by,

$$\frac{\Delta\varepsilon}{2} = \varepsilon_a = \frac{\sigma_f' - \sigma_m}{E}(2N_f)^b + \varepsilon_f'\left(\frac{\sigma_f' - \sigma_m}{\sigma_f'}\right)^{c/b}(2N_f)^c. \qquad (2.36)$$

The Manson-Halford equation inserts the effect of mean stresses in both its elastic and plastic terms and it tends to overestimate the mean stress effect at short lives since mean stress relaxation may occur at high plastic strains.

Smith, Watson and Topper (SWT) [27] have proposed another equation to incorporate the mean stress effects into a strain-life model give as,

$$\sigma_{max}\varepsilon_a E = (\sigma_f')^2(2N_f)^{2b} + \sigma_f'\varepsilon_f' E(2N_f)^{b+c}, \qquad (2.37)$$

where $\sigma_{max} = \sigma_m + \sigma_a$. This equation assumes that for different combinations of strain amplitude and mean stress, the product $\sigma_{max}\varepsilon_a$ remains constant for a given life. This equation predicts an infinite life when $\sigma_{max}$ is zero, and becomes undefined when $\sigma_{max}$ is negative and no fatigue fracture occurs. Using Eq.(2.37), fatigue life calculations can only be performed when a tensile load is present. Among the three equations used to account for mean stress effects, the SWT parameter has been shown to provide better predictions for a wider range of different materials and thus is of more general use in engineering design [3].

In [10-12], the Morrow, the Manson-Halford, and the SWT models given by Eqs.(2.35)-(2.37), were used to calculate the fatigue lives of unnotched, mildly notched, and sharply notched bars under high tensile mean stress conditions. The results were

compared to those obtained from corresponding experiments. For notched specimens, the local stress and strain histories were calculated using the cyclic stress-strain curve in conjunction with the plane stress form of Neuber's rule given in Eq.(2.16). The computed lives were far from the experimental fatigue lives. As mentioned in their papers, the errors may have been caused by considering a local uniaxial state of stress and therefore neglecting the multiaxiality at the notch root. That is, a notched circumferential bar under tensile loading is not in a state of plane stress. Thus the local stress-strain behavior was inaccurately determined and resulted in an inaccurate prediction of fatigue lives by the strain-based models. Another important reason for the large errors in the fatigue life calculation was that the material fatigue properties and the cyclic stress-strain curve used were taken from published testing data, and the data was not strictly applicable to the material used in their experimental work.

It should be noted that all the ε-N models presented do not incorporate the effect of cyclic creep that occurs at high mean stresses. In 1996, Xia, et. al. [28] suggested an energy-based fatigue theory to correlate properly the effect of mean stress and ratcheting strain. In their model, the mean stress and ratcheting effects were taken account independently. That is, a modified energy parameter, $\Psi_m$, that takes into account the mean stress effect was used for the pure mean stress effect and is given by,

$$\psi_m = \Delta W^p + f\left(\frac{\sigma_m}{\sigma_a}\right)\Delta W^e = \kappa_u N_{ff}^{\alpha} + C_u. \tag{2.38}$$

The rate form parameter, $\Psi_r$, is defined to account for the ratcheting effect and is given

by,

$$\psi_r = \sigma_{max}\dot{\varepsilon}^r_{aver} = \kappa_r N_{fr}^{\beta} + C_r. \tag{2.39}$$

The total fatigue life is found from the results of Eqs. (2.38) and (2.39) as:

$$\frac{1}{N_{ff}} + \frac{1}{N_{fr}} = \frac{1}{N_f} \tag{2.40}$$

In Eqs. (2.38)-(2.40), $\Delta W^p$ is the plastic energy per cycle, $\Delta W^e$ is the elastic energy per cycle, $\kappa_u, \alpha$ and $C_u$ are the material constants obtained from the fully reversed uniaxial fatigue tests, $\kappa_r, \beta$ and $C_r$ are also the material constants related to the ratcheting effect, $N_{ff}$ is the number of cycles to failure if there is no ratcheting effect, $N_{fr}$ is the envisaged "pure ratcheting" life, and $N_f$ is the predicted fatigue life. The stress-controlled fatigue tests with tensile mean stresses on ASTM A-516 Gr. 70 steel were conducted in [28]. A good agreement was found between the experimental results and predicted lives calculated by Eqs. (2.38)-(2.40).

## 2.3 Conclusions of Literature Review

The stress-life (S-N) method of fatigue analysis uses the nominal or applied stress in its analysis, which is generally within the elastic range of the material. However, the applied nominal maximum stress can be greater than the yield stress of the material under high mean stress conditions, where the S-N methods cannot be applied efficiently.

Moreover, the applied nominal mean stress may be greater than the ultimate strength at high mean stress and high R ratio conditions, and therefore the Modified Goodman and Gerber methods cannot be applied.

The strain-life (ε-N) method of fatigue analysis takes into account the local or notch root stresses and strains where plastic deformation may occur. The analytical approximation methods such as Neuber's rule and the ESED method are commonly used to determine the local stress-strain behavior based on the assumption of local plasticity. Since large-scale yielding occurs under high mean stress conditions, the assumption of the local plasticity in Neuber's rule and the ESED method is violated. However, Neuber's rule and the ESED method, when used together, do predict a band from the material yield point through to general net section yielding, within which the actual strains fall. The Hoffmann and Seeger model may be more useful for high mean stress conditions since it was developed to specifically take into account the large-scale plasticity. Among the three ε-N mean stress correction models, the SWT model is more commonly used in design. However, it does not incorporate the effect of cyclic creep, which may occur in high mean stress applications.

This literature search shows that very few papers exist that address the effect of high tensile mean stresses on the fatigue life of unnotched or notched test specimens. Most of the research work on high mean stresses has presented S-N data. Their papers highlighted the general trend of S-N data and the existence of cyclic creep. Only several papers presented by the same research team [10-12] have tried to evaluate the ability of the stress-life and strain-life methods to predict the fatigue life under high mean stress conditions. Their S-N results highlighted the methods inability to predict the fatigue life

of specimens under high mean stresses. However, they did not evaluate existing S-N models such as Cook [7] and Gunn [8] that well designed to handle high mean stress applications. They furthermore did not account for notch root biaxiality. Their ε-N results were inconclusive due to both experimental and model application errors. It is necessary that a systematic evaluation of the methods need to be conducted for components under high mean stress conditions.

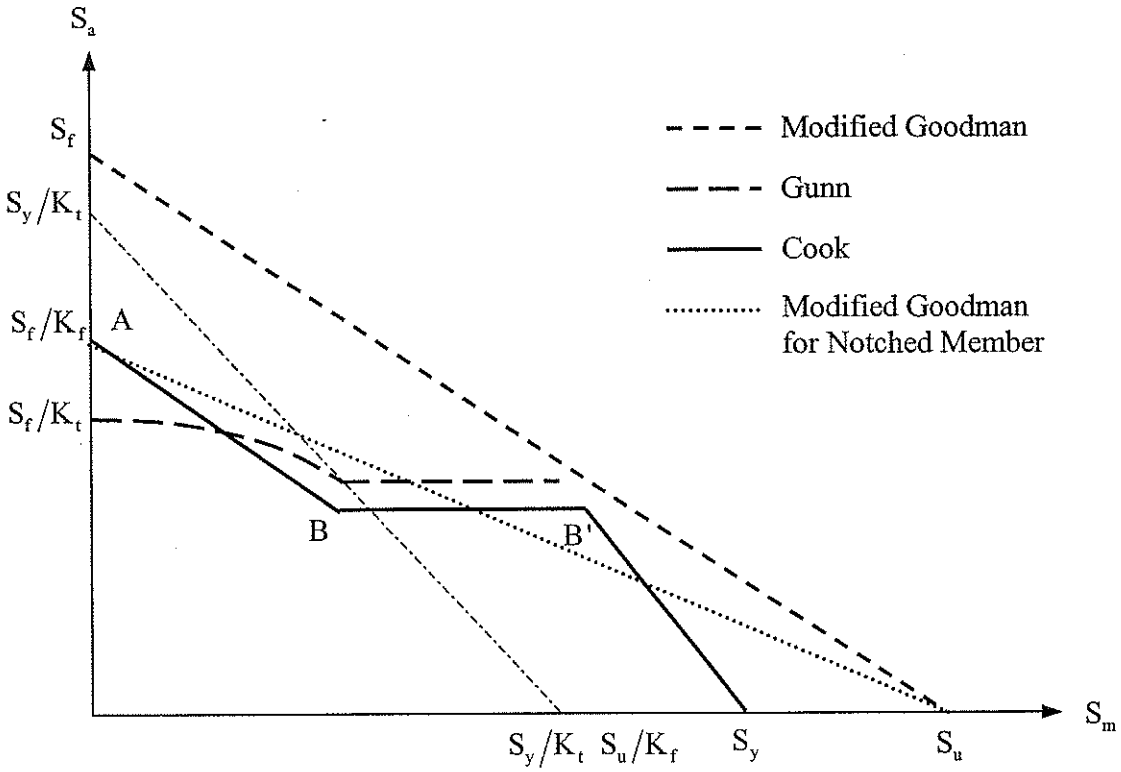


Figure 2.1 Haigh Diagram Showing Different Empirical Models

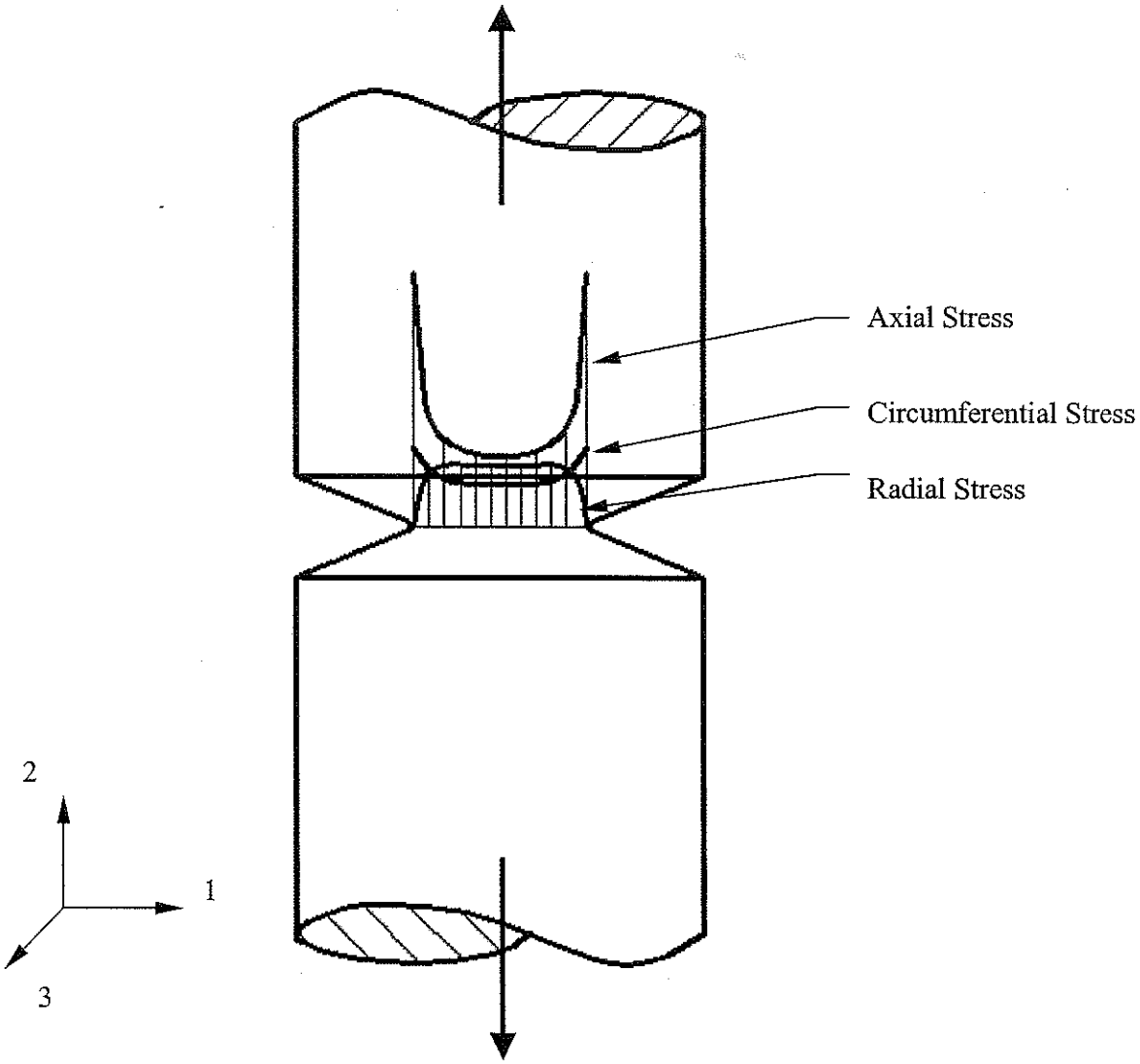


Figure 2.2 Stress Distribution at a Notch

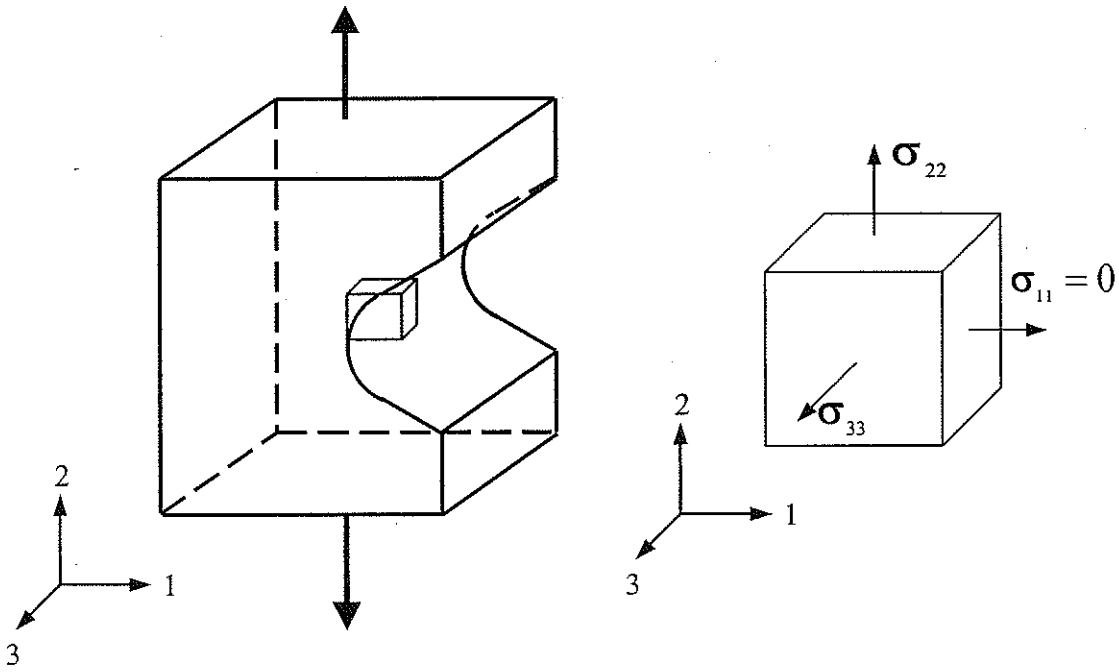


Figure 2.3 Stress State on Notch Tip Element in Body under Uniaxial Load

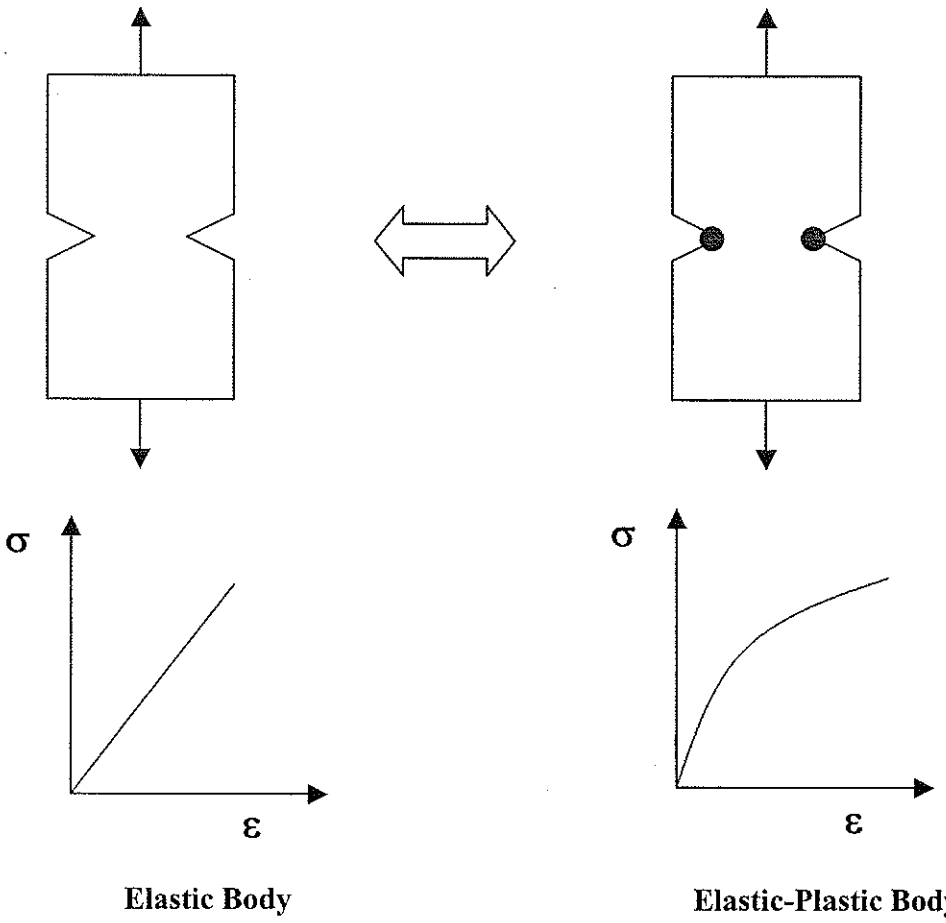


Figure 2.4 Simplified Analytical Techniques for Notch Root Elastic-Plastic Strain Determination - Local Plasticity Assumption

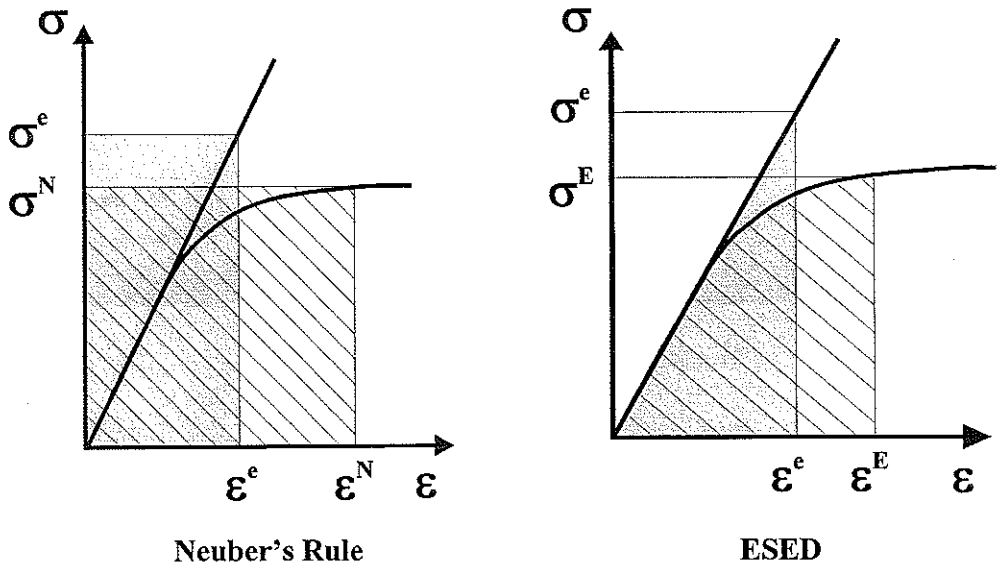


Figure 2.5 Graphical Representation of Neuber's rule and the ESED Method

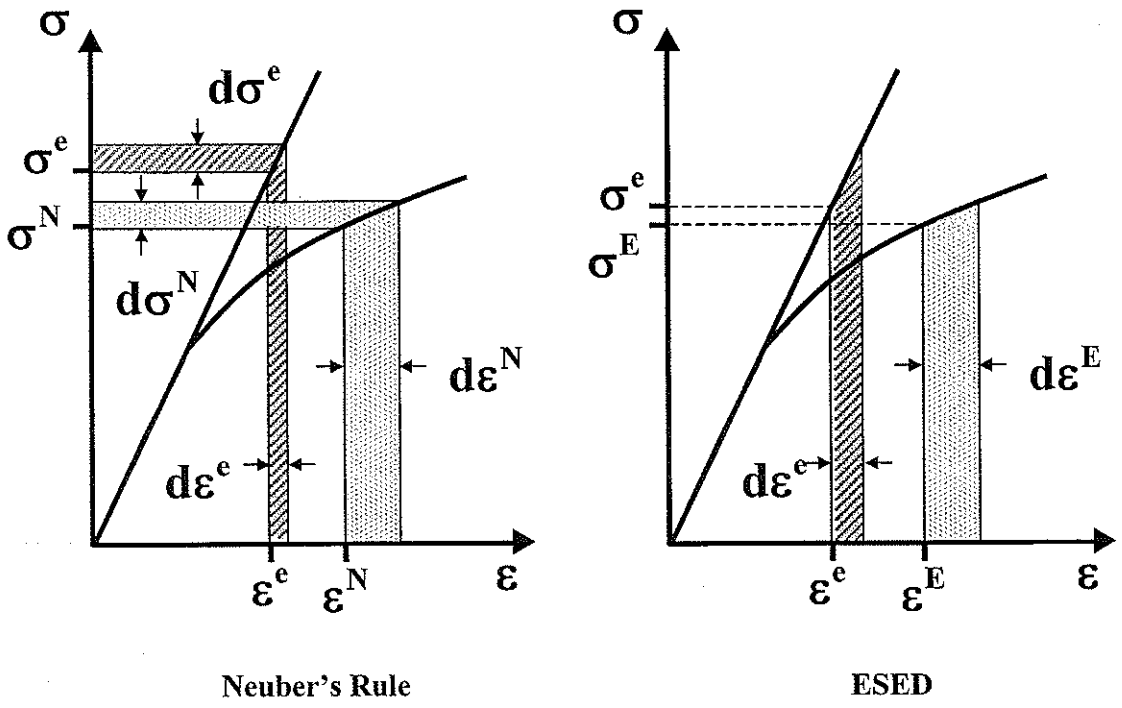


Figure 2.6 Incremental Neuber's Rule and ESED Method

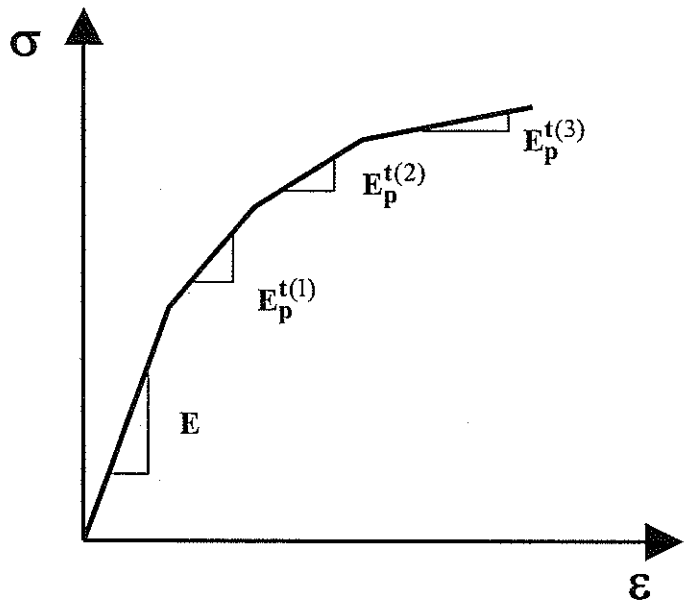


Figure 2.7 Multi-linear Material Law

# CHAPTER THREE

# EXPERIMENTAL PROGRAM

As mentioned in Chapter One, one of the objectives of this thesis is to analytically and experimentally assess the ability of the existing fatigue life prediction models to predict the fatigue life of components subject to high mean stress and high R ratio loading cycles. To meet the objective, three sets of experimental tests were conducted in this research. The first set was designed to determine the monotonic tension properties of the material tested. These are necessary to apply the S-N methods. The second set, the fully reversed fatigue tests, were designed to determine the fatigue properties necessary to apply the ε-N method. The monotonic and cyclic stress-strain curves used in notch root stress-strain determination were obtained from the first and second testing sets respectively. The last set was designed to examine the fatigue behavior of the test material when subjected to a high mean stress. In this chapter, a description of the specimens used in these tests is first presented in Section 3.1. The laboratory equipment used is subsequently described in Section 3.2. Finally, all experimental procedures are described in Section 3.3.

## 3.1 Material Used and Specimen Design

All specimens used in this investigation were machined from 12.7 mm diameter hot rolled SAE 1045 steel. The material was either provided by the University of Iowa or obtained from their suppliers. A chemical composition analysis of the provided material had been conducted and constituent percentages were within the allowable according to

the ASM Handbook on SAE 1045 steel [29].

The steel rods as received were cut into approximately 130 mm length segments. This length was chosen to minimize any bending during testing but provide an adequate length for gripping and for mounting the extensometer. All specimens were then heat treated to the same hardness, Rc 37, by Tri-City Heat Treatment in Rock Island, Illinois, USA. To avoid distortion caused by the heat treatment, the specimens were held at both ends with a gripping device during the heating process. During heat treatment, the specimens were first recrystallized at 870°C for two hours in a controlled atmosphere of 0.45% carbon to avoid surface decarburization. The specimens were then taken out of the furnace and quenched in agitated oil at 46°C for 15 minutes. Finally, the specimens were tempered by reheating them to 427°C and holding them at this temperature for two hours. The surface hardness of the test piece was checked on randomly selected specimens by using the Versitron Rockwell Hardness Test Machine with a diamond cone indenter, provided by the Metallurgical Sciences Laboratory at the University of Manitoba. The average values collected from these hardness tests showed that the hardness of this material was Rc 37.

Three different cylindrical specimen designs were prepared for this study including smooth monotonic tension (Fig. 3.1), smooth fatigue (Fig. 3.2), and sharply notched (Fig. 3.3) samples. Two smooth monotonic tensile specimens were used to obtain material monotonic properties and were designed in accordance with ASTM Standard E08 [30]. Sixteen smooth fatigue samples were prepared according to ASTM Standard E606 [31]. These samples were used in the fully reversed low cycle fatigue tests performed to obtain the material cyclic stress-strain curve and the fatigue properties.

Twenty 60° V-shape sharply notched samples were machined with a notch root radius of 0.25 mm. This design can introduce a high elastic stress concentration factor, typically ranging from two to five, similar to those found in bolt threads [32].

The machining of all specimens consisted of centerless grinding, reduced section machining, and polishing. The centerless grinding was conducted by Standard Manufacturers Services Limited, Winnipeg, MB, to reduce any eccentricity in the specimens. The ground finish diameter was $11.9 \pm 0.025$ mm. It should be noted that all specimens, except for the sharply notched samples, were centerless ground after heat treatment. Although the sharply notched centerless ground specimens were held in a gripping device during heat treatment, several samples had to be discarded due to distortion. All remaining sharply notched samples used in the study were tested and found to exhibit negligible distortion. The reduced section machining of the smooth samples was conducted on the CNC lathe at the University of Manitoba.

Since the surface finish of a specimen significantly affects its fatigue limit, all samples were polished to eliminate machining marks and residual stresses that may have been introduced into the surface layers during the machining process. For the smooth specimens, the gauge length of each specimen was circumferentially polished with three different grades of emery paper having 240, 600, and 1200 grit size. The surface finish of each specimen was both visually and microscopically checked using a 5x magnifier to ensure that no machining marks existed. Particular attention was given to any circumferential marks perpendicular to the loading direction since their presence significantly affects the fatigue limit. After polishing, the reduced section diameter of the smooth specimen was measured by a vernier caliper. Three measurements were taken on

each specimen at different locations within the gauge section, and the diameter was determined by taking the average value.

The polishing of the sharply notched specimens focused on the notch root portion where fatigue cracks would normally initiate. To do so, these specimens were clamped into a drill, and then the notch root was polished by applying a diamond abrasive with a cotton yarn in the circumferential direction while the drill was running. After polishing the notch roots, the finish was checked by using a 20x microscope, and machining marks were not found. In order to determine the net section diameter in the plane of the notch in the sharply notched specimens, a microscope caliper was used. Similar to the smooth samples, three measurements were taken for each notched specimen at 120° diametric intervals and the average values were used for net section area calculations.

## 3.2 Testing Equipment Description and Application

The equipment used in this research consists of a servo-hydraulic load frame, an optical strain measurement system, point strain measurement equipment, and a data acquisition system. An overall layout of testing equipment used in this study is illustrated in Fig. 3.4. A scanning electron microscope (SEM) was additionally used after testing to examine the fracture surfaces.

### 3.2.1 Instron Load Frame

All tests were performed on the Instron 8800 closed loop servo-hydraulic bi-axial load frame (Fig. 3.5). The full capacity of the load frame is $\pm 250\,\text{kN}$ in tension and $\pm 2\ \text{kN}\cdot\text{m}$ in torsion. The system essentially consists of an adjustable crosshead, a load

cell, two actuators (one tensile and one rotary), two collet type grips, and a FastTrack© 8800 controller. Additionally for user interface, the system contains two manual control panels and a FastTrack© console computer. In this study, only the tensile axis was used, while the torsion axis was kept idle.

It should be noted that the hydraulic grip system consists of four-finger collets that are only suitable to grip 25.4 mm diameter bars. Since the diameter of the shank portions of all specimens used in this study was 11.9 mm, medi-fixtures were needed to mount the small diameter samples to the hydraulic grips. For this purpose, two smaller collets were designed to transfer the pressure from the hydraulic grips to specimen shank and clamp them tightly.

A high hardness 25.4 mm diameter solid steel bar, cut into two 61 mm segments, was used as the base material for the medi-collets. The 61 mm length of the medi-collets was chosen so that each collet could fully fit into the upper and lower hydraulic grip of the load frame. In order to provide a cavity to hold the specimen, 48 mm in depth and 11.9 mm diameter dead holes were drilled into one side of each segment. After the holes were drilled, reduced sections (see Fig. 3.6) were machined into the opposite side of each segment. Four 0.25 mm width and 50 mm length slots at 90° circumferential intervals were subsequently machined through the holes by making two perpendicular wire cuts along the longitudinal axis. These slots were machined to provide room for the collets to shrink when gripped and thus insure that the test specimens could be tightly clamped. It should be noted that the slots were machined into the reduced section to a 5 mm depth. This provided the collet fingers the capacity to shrink more freely and with less constraint at their bottoms. A drawing and a photograph of the small collets are illustrated in Figs.

3.6 and 3.7 respectively. For specimen installation, each finger of the small collets was aligned with those of the hydraulic grips to insure that the clamping pressure could be transferred evenly to the sample shanks. This additionally acted to minimize the bending effect that may have otherwise been introduced during clamping.

### 3.2.2 Deformation Measurement System

In order to assess the ability of the strain-life approach of fatigue analysis to predict the life of components under high mean stresses, the strains at the point of highest stress concentration in the test specimens resulting from the applied load are required. Due to the V-shape notch geometry, the traditional strain gauge measurement method could not be used. This is primarily due to the fact that it was impossible to affix the smallest available strain gauge at the depth of the notch. However, even if possible, there would be errors in the peak strain measurements caused by using a finite gauge length in a steep gradient area. To overcome these constraints, a non-contact optical deformation measurement device was used in this study as shown in Fig. 3.8. This device, the ARAMIS©, can measure a strain range from 0.1% up to >100% with 0.02% accuracy. This optical deformation measurement device consists of two high resolution CCD (Charge Coupled Device) cameras, a trigger unit, a PC with two image processing cards, and a post-processing software package. To measure 3D deformations and surface strains using the ARAMIS©, a pattern is first applied to the area of the test object where strain measurement is required. As loads are applied, the pattern deforms with the test object. Images of the deforming pattern are captured using two CCD cameras. Using image processing, the deformation and surface strain fields are calculated. Descriptions of the

steps required in specimen preparation, image acquisition, and a general overview of the image processing software are given below.

Specimen Preparation

The surface of the object of measurement must exhibit a pattern in order for the image processing software to unambiguously match the pixels of recorded images as the specimen deforms. A pixel in a reference image can thus be matched to the corresponding pixel in the destination images and the material displacement can be determined. The optimal pattern on the object should exhibit highly contrasted colors (i.e. white and black) and be of a moderate size. In this study, the patterns on the specimens were painted using flat white and black enamel. Specifically, an even base layer of flat white enamel was first spray painted onto the portion of the specimen under investigation. Since the pattern deforms along with the object and it reflects the deformation of the object, the ideal thickness of the base layer is normally barely enough to cover the specimen surface. After drying, flat black enamel was applied over the base layer using an airbrush to produce a random pattern of small dots. Caution was used in spraying the background on the sharply notched specimens so as to prevent too much enamel from accumulating at the notch root. A typical arbitrary pattern and the pattern applied onto a sharply notched sample are shown in Figs. 3.9 and 3.10 respectively.

Image Acquisition

Before taking any images using the CCD cameras, the optical deformation measurement device requires calibration. To do so, images of a supplied calibration

object (with a given arrangement of white dots) in different orientations and positions are taken by the measurement system. The image-forming parameters of the cameras are subsequently determined by the software by computing the coordinates of the individual dots in the calibration object using the least squares adjustment method. The parameters are saved into a configuration file that is later used for deformation calculation.

After calibration, in order to obtain clear images, the cameras are manually adjusted so that the centers of left and right images of an area under investigation (taken from the left and right camera) are located on a common point. A video window on the computer monitor showing images of the desired test area is used to focus the cameras. Images of the measurement area can subsequently be recorded at desired time, load levels, or other trigger modes.

Image Processing

Initially, the image processing software defines unique correlation areas called macro image facets across the entire imaging area. The center of each facet is analogous to a strain rosette. The size of these facets, defined by the distance between the centers of adjacent facets, is chosen by the user, and is typically 5-20 pixel square. These facets are tracked in each successive image with sub-pixel accuracy. Using photogrammetric principals, the 3D coordinates of the imaging area are subsequently calculated. The software then calculates the 3D shape of the area, the 3D displacements, and the surface strain components.

### 3.2.3 Point Strain Measurement Equipment

A 120 Ω three-element rosette strain gauge (VISHAY Micro-Measurement,

CEA-06-125UR-120, Fig. 3.11) and an eight-channel signal conditioner (VISHAY Micro-Measurement, 2120, Fig. 3.12) were used in this study. The three-element rosette has three independent grids oriented at 0, 45, and 90 degrees. The principal strains and their directions about a point can be calculated with the three independent measurements from each grid. The eight-channel strain gauge conditioner functions to convert low-level signals from strain gauges to high-level outputs for recording.

An Instron 2620-601 dynamic extensometer (Fig. 3.13) with a ±5 mm full-scale range and a 12.5 mm default gauge length was used to control the fully reversed strain-controlled fatigue tests. The extensometer is able to send feedback signals to the Instron load frame to enable dynamic strain-controlled tests at up to 40 Hz.

### 3.2.4 Data Acquisition System

A PCI-DAS6402/16 analog and digital I/O board (Measurement Computing Corporation at Middleboro, MA, US) was used in this study for data acquisition. All the analog test data, such as load, strain gauge and extensometer data were collected by the data acquisition board and converted into digital data for storage. A graphical programming application, Agilent VEE OneLab 6.1 [33], was used to acquire and store the data during testing. Dynamic motion windows were provided by the program to monitor the load, displacement and strain values during the testing process.

### 3.2.5 Scanning Electron Microscope

A JEOL JSM 5900LV Scanning Electron Microscope (SEM) was used to investigate the fracture mechanism of the failed test specimens. This SEM is part of the

Metallurgical Sciences Laboratory at the University of Manitoba. The magnification of this SEM ranges from x18 to 300,000. The SEM has a conical lens and a fully automatic vacuum system. The 18x and 1500x magnifications were chosen for macroscopic and microscopic examinations respectively of the fracture surfaces of the monotonic tension and sharply notched fatigue specimens.

## 3.3 Test Procedure

The experimental testing carried out in this study include verification tests, monotonic tension tests of smooth and sharply notched specimens, strain-controlled fully reversed cyclic fatigue tests of smooth fatigue samples, and load-controlled high mean stress tests on sharply notched specimens. The procedure followed in conducting these tests is detailed in the subsections below.

### 3.3.1 System Verification Tests

Before any tests were conducted for the purpose of this research using the equipment described in Section 3.2, two verification tests were necessary. The first was designed to test the alignment of the system, and the second was designed to provide personal confidence in the strain field results obtained using the ARAMIS©.

Alignment Tests

Bending stresses that inadvertently occur due to misalignment between the point of load application and the specimen axes during tensile loading can significantly affect any test results. For ideal alignment, the top and bottom grip centerlines should be

precisely in line with one another, other components of the loading train, and the centerline of the symmetric test specimen.

It was suspected that any misalignment that may have occurred during the tests would be caused solely by the adaptive collets. That is, all specimens were centerless ground and checked for any eccentricities in their longitudinal axis, and the load frame had been recently purchased and rated for alignment. Nonetheless, two alignment tests were carried out. The first test was designed to test the alignment of the load frame components, and the second to test whether alignment was compromised when the adaptive collets were used. Both alignment tests were conducted in accordance with ASTM Standard E1012 [34].

To test the alignment of the upper and lower grips of the load frame, a 230 mm in length bar, centerless ground to a 25.4 mm diameter, was prepared. After installing the alignment specimen into the servohydraulic collet grips on the load frame, the load frame was set to zero load. The Instron 2620-601 extensometer was then mounted on the specimen and the load was increased to a rated force. The force was calculated to insure that it would cause only elastic deformations within the bar, and thus the elastic bending relations given in [34] could be applied. While holding the load constant, the extensometer was moved circumferentially to the opposite side of the bar, and the load was then removed. The extensometer was then rotated 90° from its position and the rated load was re-applied to the bar. Finally, the extensometer was again rotated circumferentially to the opposite side of the bar, and the bar was unloaded. During the test, the strain readings were recorded by the data acquisition board. A small Aglient VEE One program was written for the purpose. From the recorded strains, the maximum

bending strain was calculated according to the ASTM Standard E1012. The maximum bending strain was found to be much less than 5 % of the minimum axial strain. According to ASTM Standard E606, this indicated that the testing system was aligned.

To test the alignment of the adaptive collets a 127 mm in length bar, centerless ground to a 11.9 mm diameter, was prepared. This specimen was then installed into the adaptive collets that were positioned in the upper and lower grips of the load frame. The same procedure as detailed above was followed in this adaptive collet alignment test. Since the maximum bending strain within the bar was calculated to be much less than the 5 % axial strain, it was concluded that the adaptive collets designed and machined for this research did not introduce any misalignment into the test set up.

ARAMIS© Confidence Tests

Although the developers of the ARAMIS© have well-documented [35] the validation of their equipment, confidence in our ability to use the equipment to obtain accurate strain results was evaluated. This confidence was obtained by conducting a tensile test on a bar while measuring the strains using the ARAMIS© and for comparison the more conventionally accepted strain gauge measurement technique.

The 25.4 mm tensile sample was machined according to ASTM Standard E08 [30]. After machining, a 120 Ω, three-element rosette, as described in Section 3.2.3, was mounted on the uniform gauge section of the sample. The diametrically opposite side of the bar from where the gauge was mounted was prepared for optical measurement, as described in Section 3.2.2. After connecting the gauge to the described signal conditioner, and creating a program for the data acquisition in Aglient VEE One, the sample was

loaded to failure. The nominal stress versus axial strain curves obtained by strain gauge and the optical deformation measurement device were plotted together in Fig. 3.14. As can be seen, the two stress-strain curves are nearly identical up to 0.02 mm/mm strain value, where the strain gauge fell off due to large plastic deformation. This simple test verified our confidence in our ability to use the ARAMIS© and further highlighted its ability to easily measure strains at large plastic deformations.

### 3.3.2 Monotonic Tension Tests

Since the material monotonic properties are necessary for fatigue analysis, two smooth (Fig. 3.1) and two sharply notched (Fig. 3.3) samples were used in the monotonic tension tests. The equipment used to perform these tests included the Instron load frame, the ARAMIS©, and the Instron extensometer described in Sections 3.2.1, 3.2.2, and 3.2.3, respectively.

Before performing each test, the gauge sections of the smooth samples and the notch portions of the sharply notched specimens were prepared with spray patterns for optical measurement as described in Section 3.2.2. The Instron extensometer was calibrated to insure that it would provide an accurate feedback signal to the load frame control computer. The automatic calibration was enabled by the load frame control unit. The calibration of the optical deformation measurement device was also performed using the smallest 10x8 mm calibration block following the procedure as described in Section 3.2.2. The smallest calibration block was chosen since it would provide the highest resolution of the captured images and thus the best accuracy in the measured strain values.

After sample preparation and equipment calibration, each sample was clamped into the upper grip of the load frame and the optical measurement device was adjusted. The two cameras of the measurement device were manually adjusted to the right working position for each sample, where the centers of left and right images of the area under investigation could be located on a common point as mentioned earlier in Section 3.2.2. In order to verify that the captured images of the investigated area would be processed for strain calculations, two sets of images were taken. As shown in Fig. 3.15, the green area at the notch portion of a sharply notch specimen indicates the acceptable facets recognized by the optical measurement device. Thus these facets could be used for strain calculations. It should be noted that it was very difficult to obtain the acceptable facets for the sharply notched samples due to the notch depth. Since the strains are determined by the optical measurement device through tracking the deformation of the recognized facets in spite of the applied external loads, small strains caused by environmental noises were found by processing the first two set images. These strains were recorded and used later to offset the noise effects in the actual tests.

When all above preparations were finished, the free end of the testing sample was clamped into the lower grip of the load frame. The setup of the sharply notched specimen for a monotonic tension test is shown in Fig 3.16. All monotonic tension tests were performed in a load control mode at a rate of 0.25kN/sec in laboratory air at room temperature. The successive images of the area under investigation were taken by the two CCD cameras during loading in 0.5kN increments. This was enabled by a data cable between the load frame controller and the ARAMIS©. As a result, the smooth stress-strain curves could be generated using the results from the optical measurement device.

The Instron extensometer was used for the second monotonic tension test of the smooth specimen for further verification of the optical deformation measurement device. The small Aglient VEE One program described in Section 3.3.1 was used to record the applied load and extensometer displacement data.

### 3.3.3 Fully Reversed Fatigue Tests

Since the material cyclic stress-strain curve and fatigue properties are necessary to apply the strain-life method of fatigue analysis, the smooth specimens shown in Fig. 3.2 were subjected to fully reversed (R= -1) fatigue tests. The equipment used to perform these tests included the Instron load frame and the Instron extensometer described in Sections 3.2.1 and 3.2.3 respectively.

Before conducting each test, the extensometer was calibrated and mounted on the specimen being tested. The extensometer was calibrated using the automatic calibration function mentioned in Section 3.3.2. After installing the specimen into the adaptive collets and the upper grip of the load frame, the extensometer was mounted onto the gauge section of the specimen using rubber bands and was balanced to zero. The lower grip of the load frame was subsequently clamped, introducing a small load that resulted in a small displacement of the extensometer. The load frame was then set to zero, and the displacement reading was noted. That is, proper contact between the extensometer knife edges and the specimen was assumed if this displacement reading was zero. The installation of the specimen and the extensometer was further verified by applying small loads to specimen and calculating the elastic modulus using the load and displacement data. This elastic modulus test, conducted automatically by the LCF control software,

was generally repeated two or three times to ensure a consistent elastic modulus, and therefore provide further confidence in the extensometer installation.

In general there are three experimental techniques used to determine the material cyclic fatigue properties. These are detailed in [36] and include the companion specimen method, and the multiple and incremental step methods. In this study, the companion specimen method was used. The companion test method consists of cycling identical test samples at different total strain amplitudes until failure, and recording the resulting hysteresis loops and number of cycles to failure for each sample. This data enables both the material cyclic stress-strain and strain-life curves to be generated.

This procedure followed in conducting the tests is detailed in ASTM Standard E606. To obtain a representative cyclic stress-strain curve, the total strain amplitudes applied ranged from 0.3% to 1 %. With feed back from the extensometer to insure a constant strain amplitude, a triangular axial load waveform was applied to the specimen at a constant frequency of 0.2 Hz. This procedure was followed for all specimens except for the test specimen subjected to the 0.3 % strain amplitude. Since the small strain amplitude did not result in plastic deformation, the test was expedited by running the load frame in load control at a frequency of 5 Hz. In all tests, failure was assumed to have occurred when the maximum tensile load level dropped by 50 %. The maximum tensile load was taken as the peak load recorded during the tenth cycle of the test. The tenth cycle was chosen since it was found that the material generally becomes cyclically stable subsequent to this cycle. The load, displacement, and number of cycles to failure were automatically stored in the load frames associated control computer.

### 3.3.4 High Mean Stress Fatigue Tests

As mentioned in Chapter One, the objective of this thesis is to study the high tensile mean stress effects on fatigue behavior. To achieve this task, stress control fatigue tests were performed on the sixteen sharply notched SAE 1045 steel specimens shown in Fig. 3.3. The equipment used to perform these tests included the Instron load frame and the optical deformation measurement device as described in Sections 3.2.1 and 3.2.2 respectively. On all sharply notched specimens patterns were applied to the notch portion (Fig. 3.10) for the ARAMIS© measurements. Following the same procedure as described in Section 3.3.2, the positions of the two cameras were adjusted for each sample and the small strains caused by environmental noise were calculated and recorded.

All tests were conducted in load control and the load levels were adjusted in all tests to insure stress ratios of R=0.7 and R=0.8 were maintained. The ultimate strength for the sharply notched specimen is much higher than that of the smooth specimen due to the notch hardening effect, which allowed the mean stresses used in some tests to exceed the un-notched ultimate strength. The first test for both R ratios was performed with a net section nominal maximum stress equal to 95% of the notch ultimate strength, $S_{un}$. The maximum stresses for subsequent tests were decreased by 5-10% of $S_{un}$. The net section nominal minimum stress was calculated by multiplying the maximum stress by the corresponding R ratio. The maximum and minimum loads used to control the tests were then determined by multiplying the stress values with the net section area of the test specimen. The mean stress was then calculated using Eq. (1.1) for each test. The mean stress applied to each sample is given in Tables 3.1 and 3.2 for R ratios R=0.8 and R=0.7 respectively. All high mean stress tests were preformed using a sinusoid axial waveform

at room temperature. The frequencies used in these tests ranged from 0.2-5Hz.

One of the objectives of high mean stress tests was to investigate the material behavior at notch tip under high mean stress conditions. To achieve this, the hysteresis loops of the net section nominal stresses versus the notch tip strain curves were obtained using the optical measurement device. Two out of sixteen sharply notched specimens were used to obtain the hysteresis loops. The optical measurement system can take three images at the standard image capture mode in which the applied loads can be recorded. As a result, a 0.2 Hz frequency was used to perform the two tests and thus 15 images of the notch portion were taken for each fatigue cycle. The 15 images were processed by referring to the undeformed notch portion images that were taken before clamping the lower end of the test specimen and subsequently the strains at the notch root were calculated.

Another objective of the high mean stress tests was to investigate the cyclic creep/ratcheting behavior of the material under high mean stress conditions. To do so, the maximum notch root strains of each fatigue cycle needed to be recorded. In other words, the optical deformation measurement device was required to take images when the maximum strains occurred at each fatigue cycle during the testing process. The optical measurement system was thus changed into the external trigger mode in which the two cameras take images and save them into the computer memory only when an input analog signal reaches the trigger level. Since the maximum strain occurred at the maximum load at each loading cycle, the notch portion images could be recorded at the maximum loads to obtain the maximum notch root strains. The load outputs in the analog voltage mode were sent via a coaxial cable from the Instron load frame controller to the trigger unit of

the optical deformation measurement device. For each test, the trigger level was carefully set to the maximum load value to insure the cameras could be triggered and thus images taken at the maximum load. Due to the limitation of the computer memory capacity, the notch portion images were taken at every 100-400 cycles instead of being taken images at each cycle. A VEE OneLab program was complied to monitor the actual load values at which the images were taken. This program functioned to record the load values only when it was triggered by the camera synchronous TTL signal that was sent out when the images were taken.

### 3.3.5 Fractographic Investigation

In order to investigate the morphology of the monotonic tension and the cyclic fatigue fracture surfaces and to compare similarities and differences between the two, macroscopic and microscopic investigations were performed on representative samples. These investigations were carried out using the scanning electron microscope discussed in Section 3.2.5.

The selected samples were cut into approximate 1-2 cm lengths using hand saw. The length was chosen to insure that the samples would fit into the vacuum chamber of the SEM. One side of the cut piece was the fracture surface. Afterwards, pressure air was applied to the fracture surfaces in order to blow off any dust and metal chippings that may have developed during the sawing process. The reduced length test specimens were then placed onto an aluminum SEM tray and put into the vacuum chamber. The macroscopic and microscopic examinations were carried out using a 18x and 1500x magnification respectively. All SEM observations were done with the electron beam

perpendicular to the sample fracture surface.

| R ratio | R=0.8 | | | | | | | | |
|---|---|---|---|---|---|---|---|---|---|
| No. | #11 | #06 | #02 | #03 | #09 | #12 | #14 | #16 | #05 |
| $S_m$ (MPa) | 1868 | 1868 | 1770 | 1672 | 1573 | 1475 | 1278 | 1082 | 885 |

Table 3.1 Mean Stresses for Specimens at R=0.8

| R ratio | R=0.7 | | | | | | |
|---|---|---|---|---|---|---|---|
| No. | #17 | #07 | #08 | #15 | #04 | #13 | #10 |
| $S_m$ (MPa) | 1764 | 1672 | 1486 | 1300 | 1114 | 929 | 743 |

Table 3.2 Mean Stresses for Specimens at R=0.7

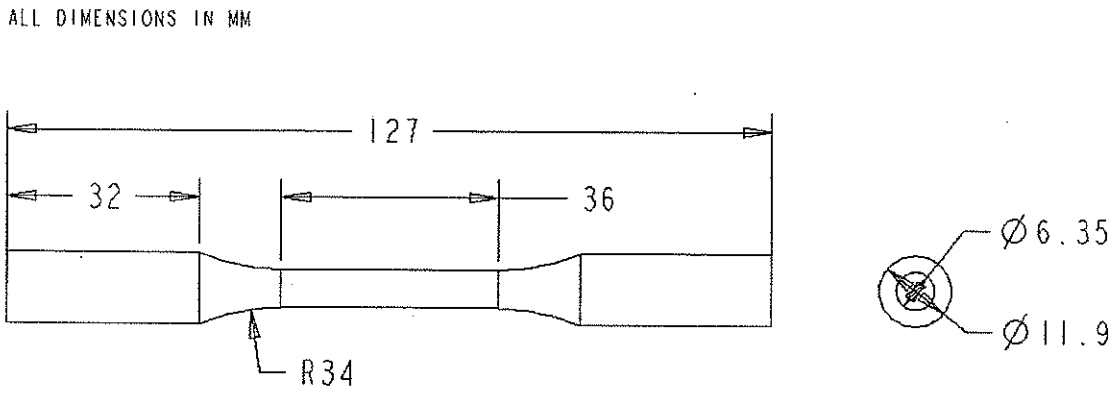


Figure 3.1 Smooth Monotonic Tension Test Specimens

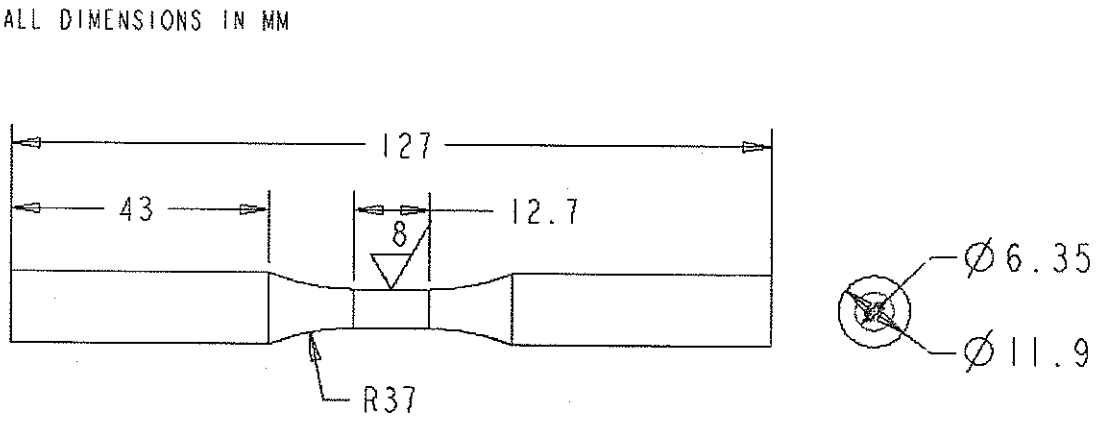


Figure 3.2 Smooth Fatigue Test Specimens

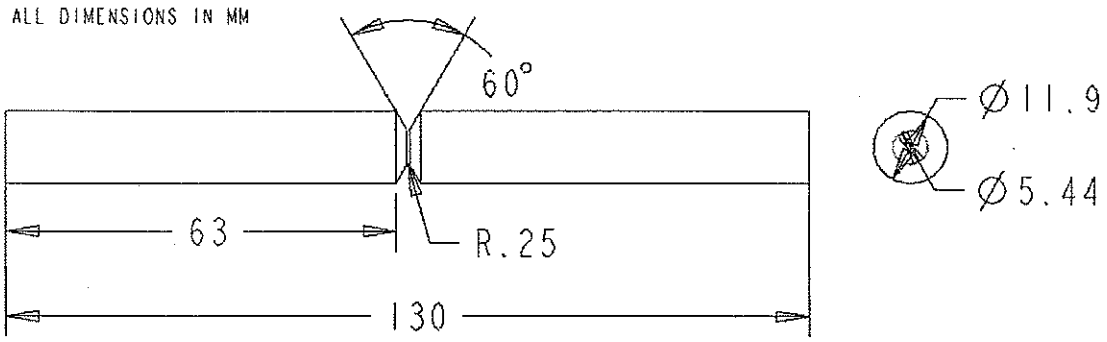


Figure 3.3 Sharply Notched Specimens

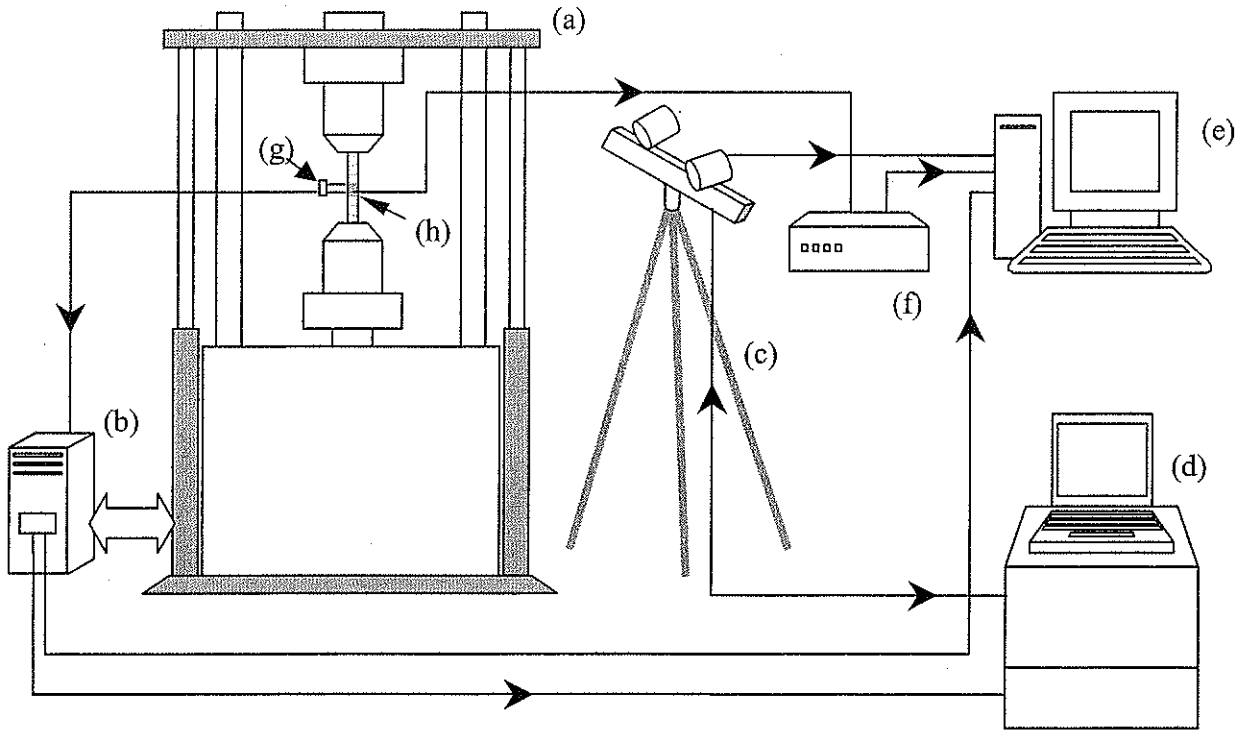


Equipment:
(a) Load Frame
(b) Load Frame Controller
(c) CCD Cameras
(d) THE OPTICAL DEFORMATION MEASUREMENT DEVICE Computer with Trigger Unit
(e) Data acquisition system
(f) Signal Conditioner
(g) Extensometer
(h) Strain Gauge

Figure 3.4 Layout of Equipment

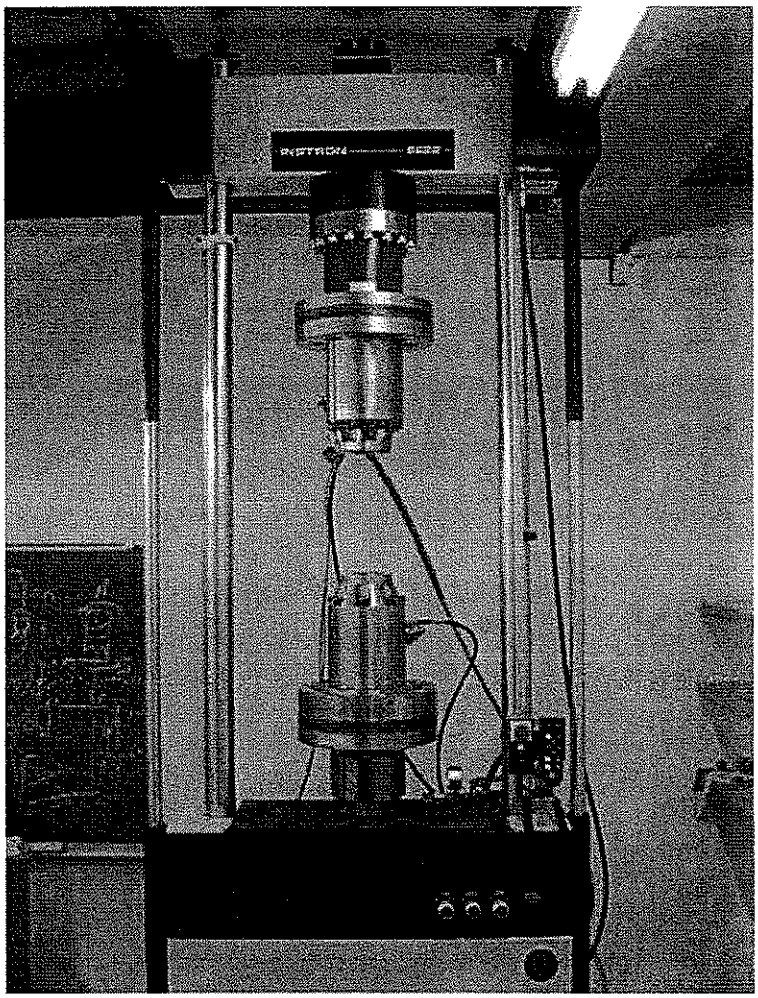

Figure 3.5 Instron 8800 Bi-Axial Load Frame

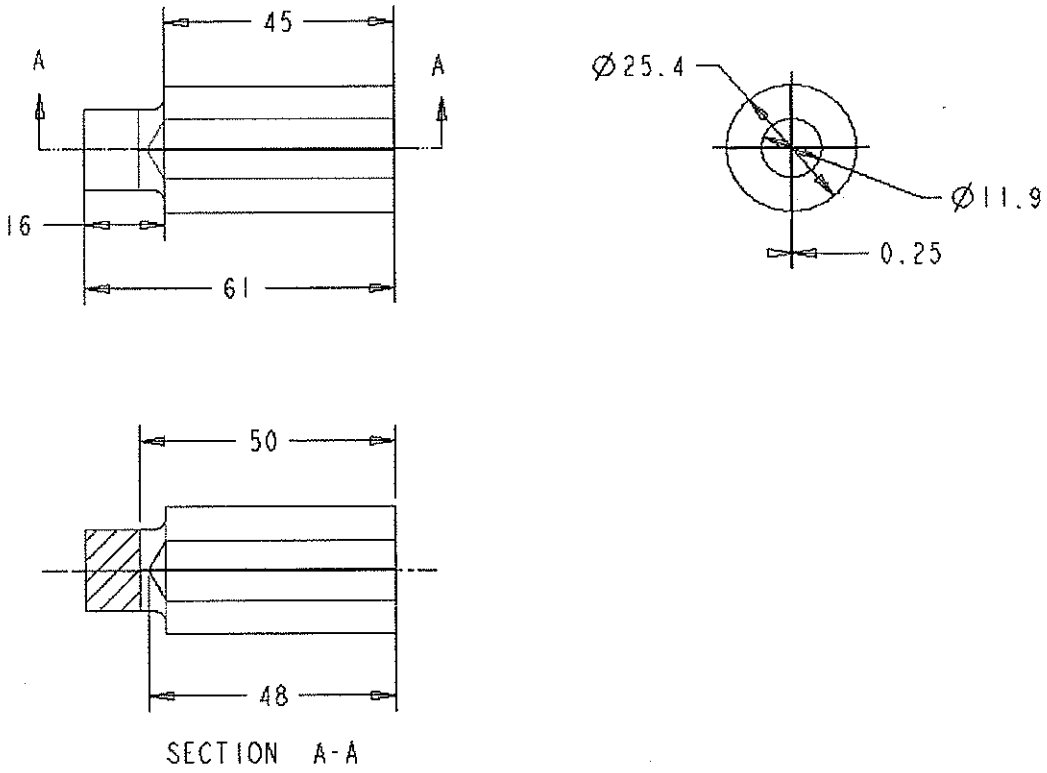


Figure 3.6 Adaptive Collets

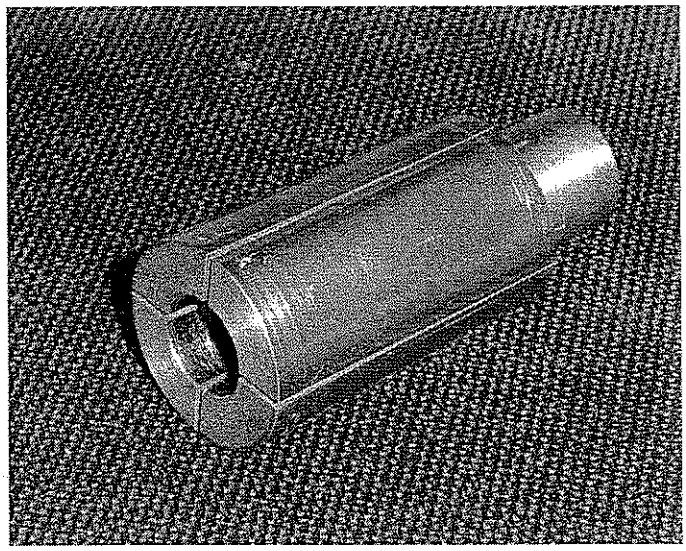

Figure 3.7 Photograph of an Adaptive Collet

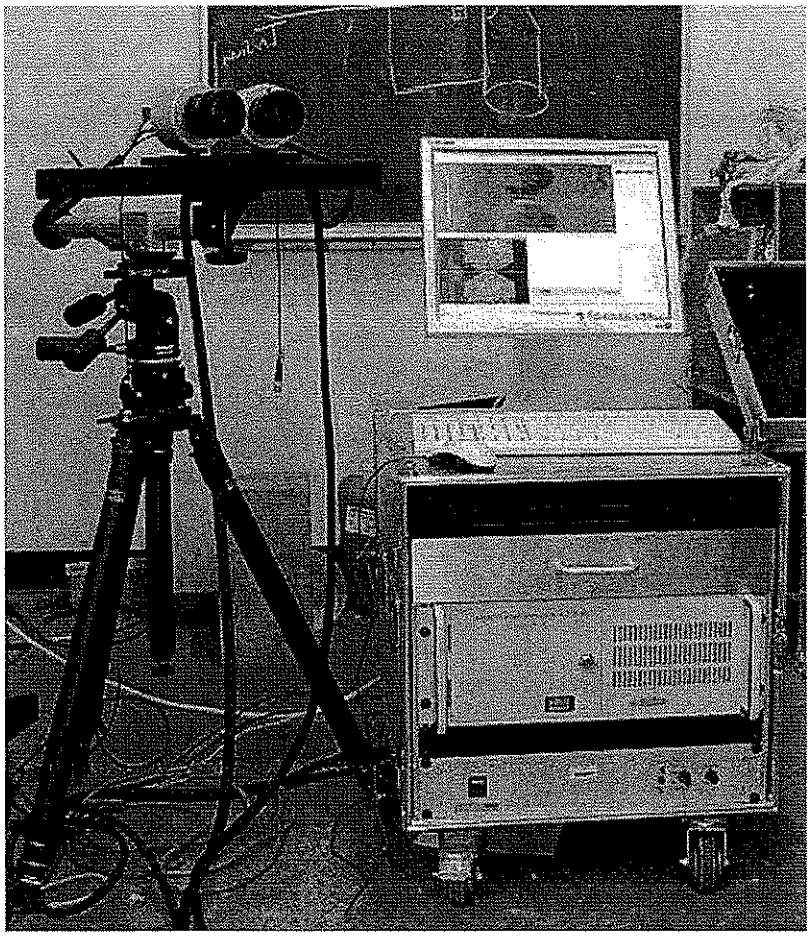

Figure 3.8 Optical Deformation Measurement System

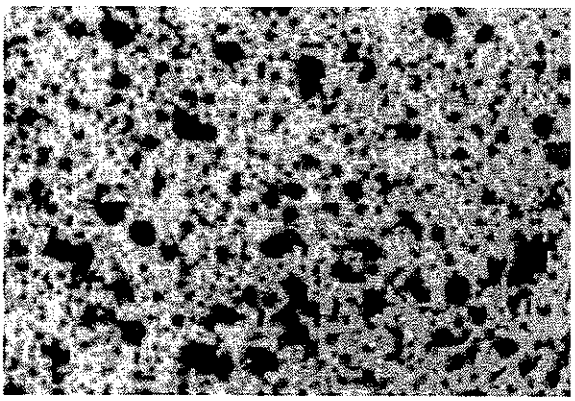

Figure 3.9 Typical Arbitrary Pattern

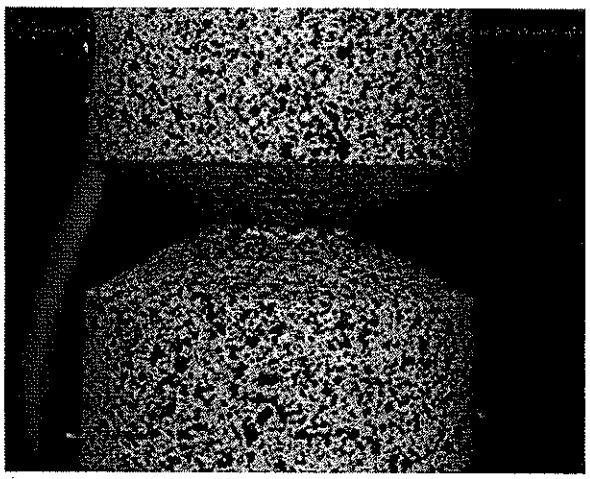

Figure 3.10 Typical Patterns Applied to a Sharply Notched Specimen

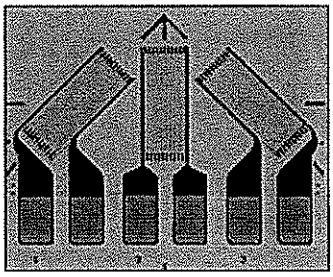

Figure 3.11 Three-Element Rosette Strain Gauge

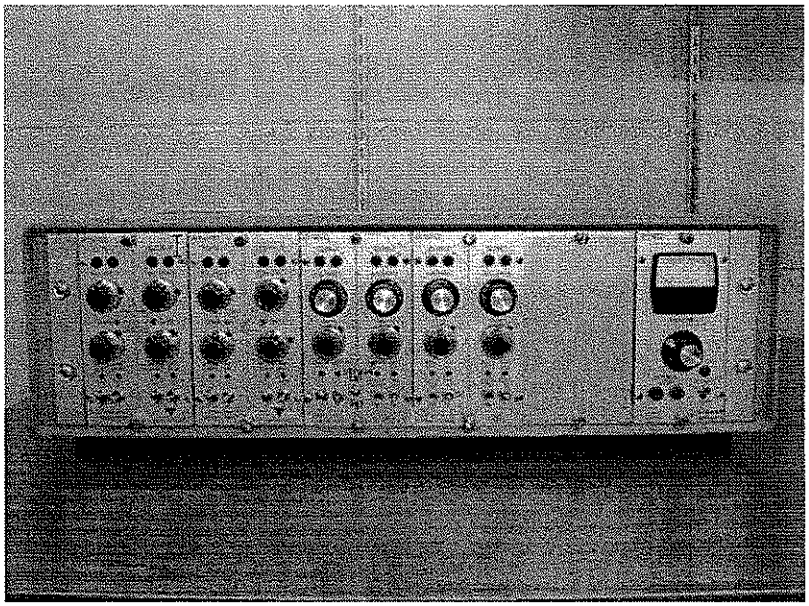

Figure 3.12 Signal Conditioner

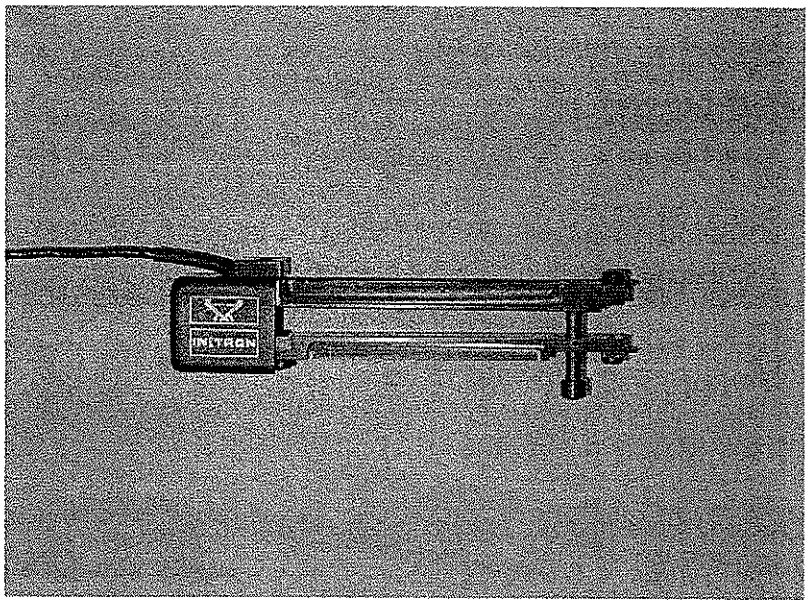


Figure 3.13 Instron Extensometer

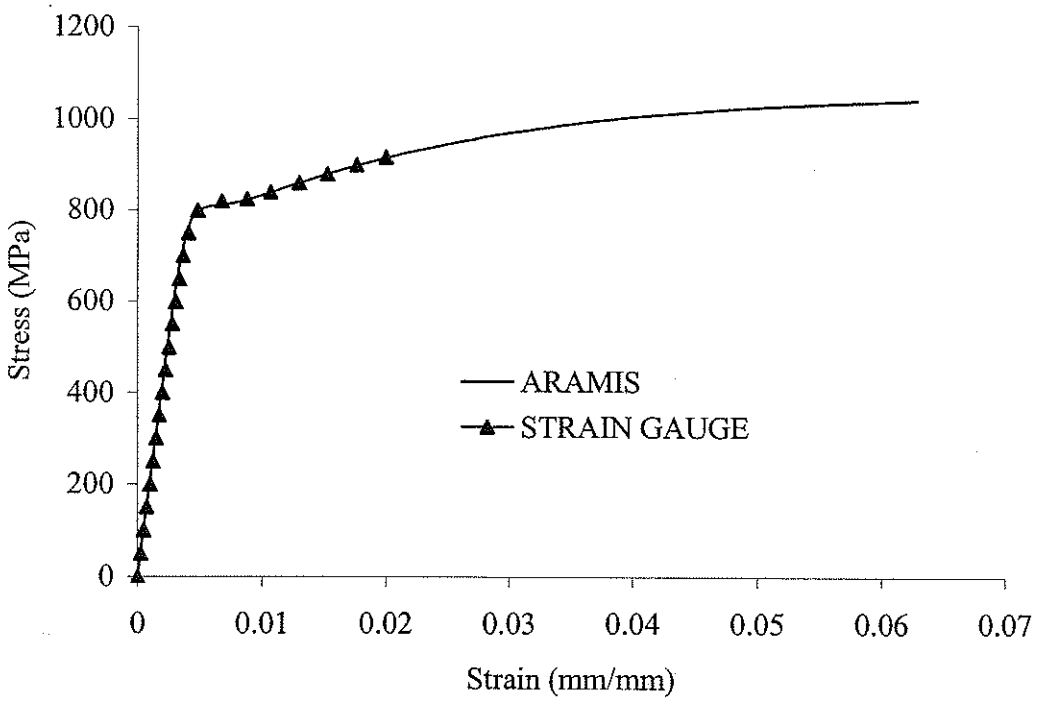


Figure 3.14 Verification of the Optical Deformation Measurement System

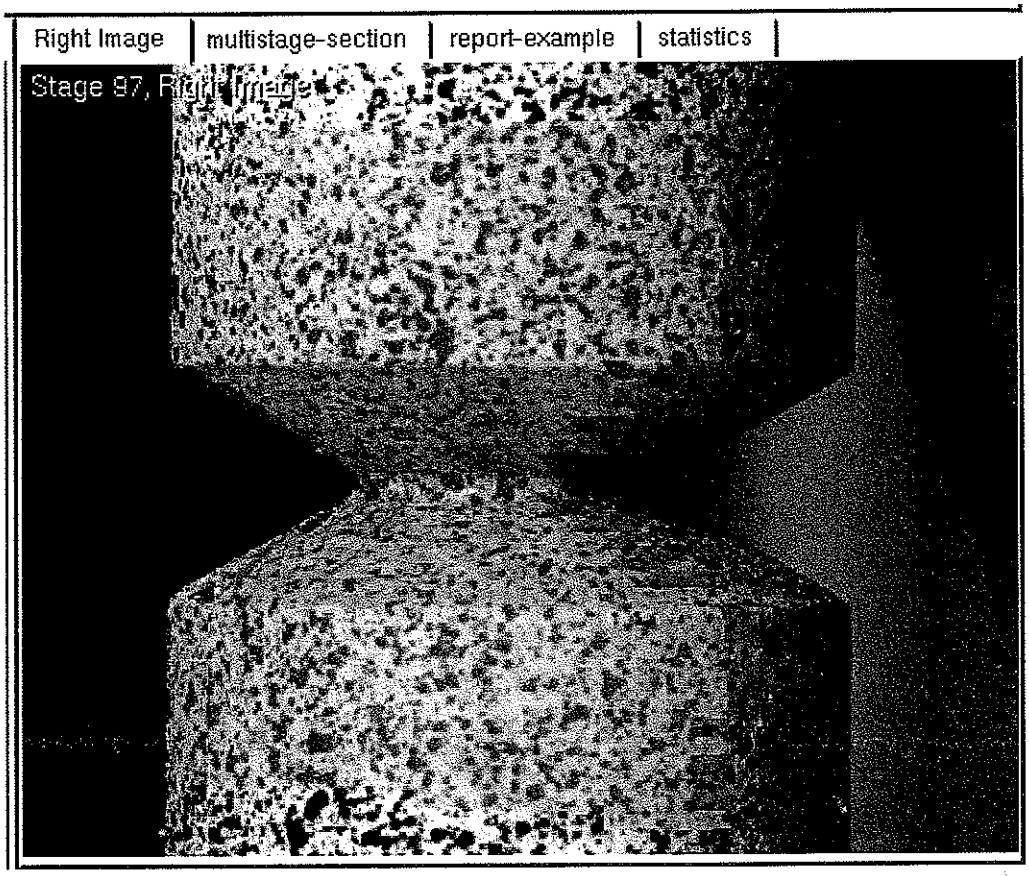


Figure 3.15 Facets Recognized by the ARAMIS©

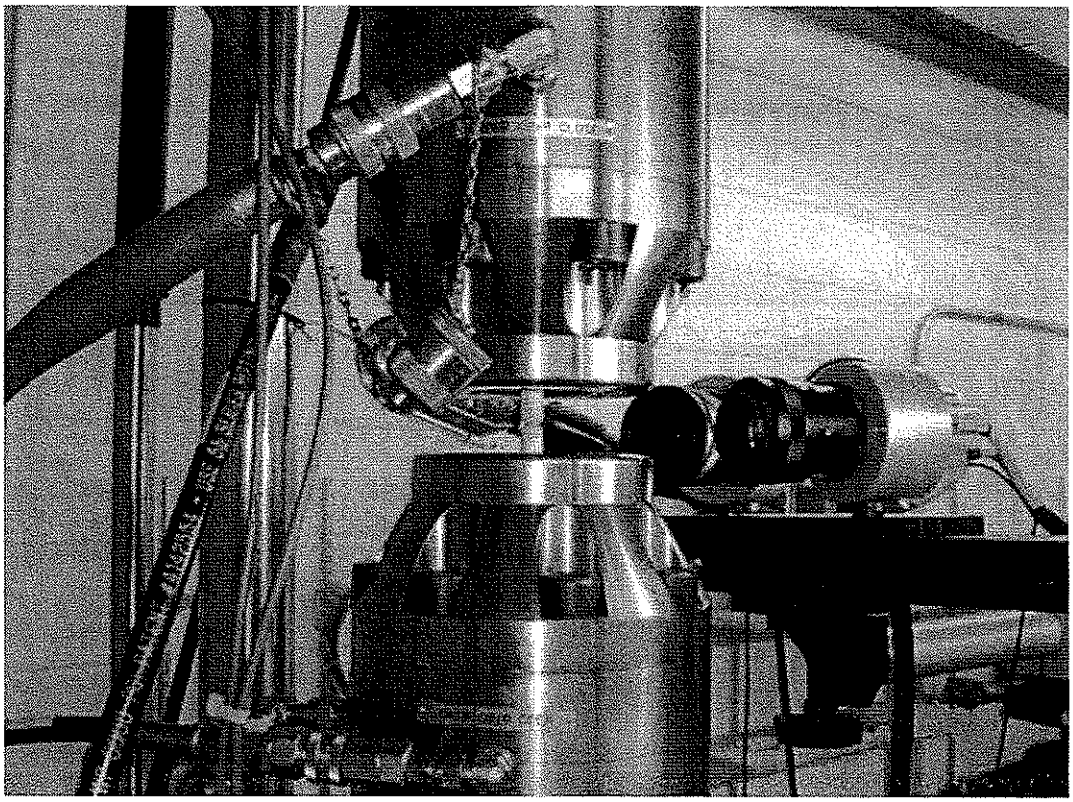

Figure 3.16 The Experimental Setup for a Sharply Notched Fatigue Specimen

# CHAPTER FOUR

# TEST RESULTS

This chapter presents the results obtained from the experimental program detailed in Chapter Three. Specifically, the monotonic and cyclic material properties are presented in Sections 4.1 and 4.2 respectively. The results of the high mean stress tests are subsequently presented in Section 4.3. Finally, in Section 4.4, an analysis of the fracture surfaces of the high mean stress test specimens is given.

## 4.1 Monotonic Tension Test Results

The monotonic material properties are fundamental for the fatigue analysis of components. The required properties for such an analysis consist of the elastic modulus, E, the yielding stress, $S_y$, the ultimate stress, $S_u$, and the general shape of the plastic portion of the curve. It should be noted that even if a smooth and a notched specimen are made of the same material, their material curves may exhibit different characteristics due to the notch strengthening effect. Specifically, when the notch root material reaches its yield point, it attempts to plastically deform. However, its deformation is constrained by the lower stressed bulk material away from the notch root. In response to this constraint, off-axis stresses are generated at the notch root, and the axial stress must be raised to initiate plastic deformation. Consequently the yield stress and plastic portions of the material curves are expected to be different for the notched and smooth specimens.

This section details the results of the monotonic tension tests described in Section 3.3.2. Specifically, the experimental smooth and notched specimen material curves and

properties for the Rc 37 SAE 1045 steel are presented in Sections 4.1.1 and 4.1.2 respectively.

### 4.1.1 Smooth Specimen Material Properties

Two tension tests were conducted on identical specimens to determine the monotonic properties of SAE 1045 steel with hardness Rc 37. The stress-strain curve obtained from one test specimen using the optical measurement was plotted together with the one obtained from the other test specimen using the extensometer in Fig. 4.1.

As can be seen in Fig. 4.1, only partial material curves were obtained using the extensometer since it was taken off after the yield point to avoid possible damage, while curves up to sample failure were obtained by the optical deformation measurement device. As shown in Fig. 4.1, the optical deformation measurement device and the extensometer yielded identical results. It also can be observed that the material has a very flat stress-strain curve after yielding. This indicates that a small increase in load after the yield point results in a large increase in plastic strain.

In this study, the monotonic stress-strain behavior was represented by the Ramberg-Osgood relationship (Eq. (2.18)). To determine the parameters K and n in Eq. (2.18), the stress was plotted against plastic strain in log-log coordinates between the yield and the ultimate strength. The plot from one monotonic tension test is shown in Fig. 4.2. The strain-hardening exponent is the slope of the linear fit line, and the strength coefficient is taken as the stress coordinate at a plastic strain of unity ($\varepsilon_p = 1$). Their values were found to be K=1342 MPa and n=0.0269. The stress-strain curves found from the experiment and from the resulting Ramberg-Osgood relationship are plotted in Fig.

4.3.

The elastic modulus and the yield strength of the material were determined by taking the average values of those obtained from each of the tension tests. The ultimate strength was calculated using the maximum load dividing by the original cross-sectional area. The average monotonic properties of the hardened SAE 1045 steel found from the two tension tests are given in Table 4.1. It should be noted that the ultimate strength, the strength coefficient, and the strain hardening exponent were obtained from one tension test due to an error of the optical measurement system in recording the test data during the other tension test.

### 4.1.2 Notched Specimen Results

The results of the monotonic tension tests of the sharply notched specimens described in Section 3.3.2 are plotted in Fig. 4.4. The figure shows two curves that represent the results of the tests conducted on the two identical samples shown in Fig. 3.3. Since the curves in Fig. 4.4 are continuously rising, the notched specimen ultimate strength, $S_{un}$, was taken as the maximum stress value. The notch strengthening ratio (NSR) for the sharply notched specimen was calculated by averaging $S_{un}$ values found from each test and dividing the result by the smooth specimen ultimate strength, $S_u = 1222\text{MPa}$. This value was calculated to be NSR=1.8. This high value for the NSR indicates the severity of the notch root constraint in the sharply notched specimens.

## 4.2 Fully Reversed Fatigue Test Results

In this section, the test results of the fully reversed strain-controlled tests

described in Section 3.3.3 are presented. From the experimental data, the cyclic stress-strain curve and strain-life fatigue properties of the SAE 1045 steel with hardness Rc 37 were determined.

### 4.2.1 Cyclic Stress-Strain Curve

The stabilized hysteresis loops, each corresponding to the half-life of a smooth sample tested, are plotted in Fig. 4.5. The tips of these loops have been connected in the figure and the resulting line represents the cyclic stress-strain curve of the SAE 1045 steel with hardness Rc 37. It was found that the modulus for unloading following a peak tensile stress is smaller than the modulus for loading following a peak compression for all tests. Thus the hysteresis loops were not perfectly symmetrical about the origin. At the half-life stabilized hysteresis loops, differences of 1-3 % between the maximum tensile and compressive stresses and 1-2 % between the maximum tensile and compressive strains were found. These differences between the maximum tensile and compressive stresses and strains were assumed negligible. It should be noted that an attempt was made to test specimens at strain amplitudes above 1 %. However, the tests resulted in the specimens buckling.

In general, as discussed in Chapter Two, the determination of the notch root strain and stress history using any simplified analytical model necessitates the use of a cyclic constitutive law. The material law is normally determined experimentally, and the experimental data is generally fit to a power law for use in calculations. This power law function is given by a Ramberg-Osgood type relation in the form of,

$$\frac{\Delta\varepsilon}{2}=\frac{\Delta\sigma}{2E}+\left(\frac{\Delta\sigma}{2K'}\right)^{1/n'}. \tag{4.1}$$

Similar to the procedure followed in Section 4.1.1 for determining the constants of the monotonic material curve, these cyclic constants are found by plotting the plastic strain amplitude, $\Delta\varepsilon_p/2$, versus the corresponding stress amplitude, $\Delta\sigma/2$ on a log-log scale shown in Fig. 4.6. The cyclic strain hardening exponent is taken as the slope of the plot, while the stress coordinate at a strain amplitude of unity corresponds to the cyclic strength coefficient. From the plot $K'$ and $n'$ were calculated to be 1773 MPa and 0.134 respectively.

Figure 4.7 shows the experimentally determined power law functions representing the monotonic and cyclic stress-strain curves of the material, and additionally the cyclic curve that was used in the previous high mean stress research [10-12] for the same material tested. The relative position of the monotonic and cyclic stress-strain curves indicates that the material cyclically softens. The cyclic yield strength was determined to be $S_y' = 771\text{MPa}$. This value was determined by the offset method provided in ASTM Standard E08 [30] that advocates the 0.2% offset method. Comparing this value to the monotonic yield strength of $S_y = 1147\text{MPa}$, suggests a 33% reduction in strength when the material is cyclically loaded. It can further be seen from Fig. 4.7 that the material properties that were used (not experimentally determined) in the previous high mean stress research [10-12] may have contributed to the erroneous life results that they obtained. It should be emphasized that the material used in this research was obtained from the same batch as used by the previous researchers.

4.2.2 Strain-Life Fatigue Properties

As indicated in the previous section, each of the companion test specimen stabilized hysteresis loops was plotted at the approximate half life when subjected to a strain-controlled fully reversed cyclic load. Table 4.2 shows the total strain amplitude applied and the number of reversals it took to actually fail each test specimen. The table also shows the stress amplitude and the corresponding plastic strain amplitude obtained from the half-life hysteresis loops of each specimen. It should be noted that the data shown in Table 4.2 was directly obtained from the LCF software records.

In order to determine the fatigue strength coefficient, $\sigma_f'$, and the fatigue strength exponent, $b$, the stress amplitude, $\Delta\sigma/2$, was plotted against reversals to failure, $2N_f$, in log-log coordinates shown in Fig. 4.8. The fatigue strength exponent is taken as the slope of the plot, while the stress coordinate at a reversal of unity corresponds to the fatigue strength coefficient. Similarly, the plastic strain amplitude, $\Delta\varepsilon_p/2$, was plotted against reversals to failure using a log-log scale shown in Fig 4.9. The fatigue ductility exponent is taken as the slope of the plot, while the strain coordinate at a reversal of unity corresponds to the fatigue ductility coefficient. The values of the fatigue and cyclic parameters for SAE 1045 steel with hardness Rc 37 are summarized in Table 4.3.

Referring to Eq. (2.34), the strain-life curves of SAE 1045 steel with hardness Rc 37, including total, elastic and plastic strain components, are plotted using the fatigue parameters in Table 4.3 on a log-log scale shown in Fig. 4.10. The experimental data were superimposed on these curves in Fig 4.10. As shown in Fig. 4.10, the elastic and plastic strain-life curves intersect at a point where the elastic and plastic strain amplitudes are equal. The life at this point is called the transition fatigue life, $2N_t$. The equation for

transition fatigue life can be derived by combining Eqs. (2.32) and (2.34), resulting in,

$$2N_t = \left( \frac{\varepsilon_f' E}{\sigma_f'} \right)^{1/(b-c)} . \tag{4.2}$$

The transition fatigue life, $2N_t$, is 1415 reversals for this material and occurs at a total strain amplitude of 0.0083 mm/mm. It can be observed that the deformation is mainly plastic when the fatigue life is less than the transition fatigue life, whereas, elastic deformation is dominant when the fatigue life is greater than $2N_t$.

## 4.3 High Mean Stress Fatigue Test Results

In this section, the results from the high mean stress tests detailed in Section 3.3.4 are presented. The S-N curves are given in Section 4.3.1. The material cyclic creep/ratcheting behavior at the notch root and the hysteresis loops are presented in Section 4.3.2.

### 4.3.1 Stress-Based Results

The fatigue test results of the high mean stress tests for sharply notched specimens at R ratios of R=0.7 and R=0.8, are listed in Table 4.4. In this table, the R ratios, the percentage of the notched ultimate strength used to calculate the maximum stress, the maximum stress, the mean stress, the ratios of mean stress to the ultimate strength of notched and un-notched specimens, and the experimental fatigue lives are presented. The fatigue lives of the sharply notched samples ranged from $10^3 - 10^5$ cycles, which were within the life regime where the fatigue properties were determined by the

fully reversed fatigue tests described in Section 3.3.3. Since the notch strengthening ratio is greater than unity, most of the mean stresses applied to the sharply notched specimens were greater than the yield strength and the un-notched ultimate strength of the material. The mean stresses applied in the tests were in the range of $0.72S_u < S_m < 1.53S_u$ and $0.41S_{un} < S_m < 0.85S_{un}$ for R=0.8, $0.61S_u < S_m < 1.44S_u$ and $0.34S_u < S_m < 0.81S_u$ for R=0.7.

The stress amplitude is plotted against cycles to failure and the maximum stress is plotted against cycles to failure for both R ratios in Figs. 4.11 and 4.12 respectively. Both plots show best fit curves obtained by fitting the experimental data to a power function in the form of Basquin's equation (Eq. (2.1)) using linear regression analysis. As shown in Figs. 4.11 and 4.12, the $S_a$-N and $S_{max}$-N curves for both stress ratios have similar steep slopes. The $S_a$-N curves show that the specimens subjected to the stress ratio of R=0.7 have a better fatigue resistance. However, the $S_{max}$-N curves show that specimens subjected to the stress ratio of R=0.8 have longer lives for a given $S_{max}$.

### 4.3.2 Strain-Based Results

A plot of the nominal stress versus notch root strain for specimen #6 (R=0.8, $S_{max}$=2076 MPa) is shown in Fig. 4.13. Since all loading paths guaranteed small load amplitudes about a high tensile mean stress, it was expected that the material at the notch root would experience elastic-plastic deformation upon initial load application, followed by repetitive elastic deformations during cyclic loading at high R ratios. The hysteresis loops as shown in Fig. 4.13 are straight lines, which indicates that elastic deformations in the loading and unloading cycles.

As mentioned earlier in Chapter One, cyclic creep/ratcheting may occur if a high enough level mean stress is involved in the loading history. If so, the average strains in each hysteresis loops increase with the applied cycles. The mean strain shift may decrease its rate and stop, it may establish an approximate constant rate, or it may accelerate and lead to a failure somewhat similar to the failure mode in a tension test [37]. The notch root maximum strains versus the number of applied cycles are shown in Figs. 4.14 and 4.15 for representative samples that were subjected to R=0.7 and R=0.8 respectively. Since the notch strain values were obtained by the optical deformation measurement device, the pseudo strains were still calculated even though fatigue cracks had existed at the notch root. To avoid the pseudo strains, the pattern images were checked for fatigue cracks. The images with obvious cracks were discarded and not used for the strain calculations. The remaining lives after cracks existed at the notch root were found to be 20-30% of the total lives. It can be observed that the notch root strains increase with applied cycles, which may indicate cyclic creep/ratcheting. It can be seen in Fig. 4.14 and 4.15 that the curves of the higher mean stress, shorter life specimens (#8 and #3) at both R ratios have steeper slopes compared to the lower mean stress, longer life samples (#4 and #5). This indicates that the rate of strain increase decreased with the applied mean stress levels. It should also be noted that for the lower mean stress, longer life samples at both R ratios, the maximum strains are approximately constant up to about half of the fatigue life. After the half life, the maximum strains increased with the applied cycles until a macrocrack initialized. It is assumed that no cyclic creep/ratcheting occurred for the samples that exhibited an approximately constant strain value up to about half of the fatigue life. The strain increase after half life may have been caused by

the visually undetected microcrack at the notch root instead of the cyclic creep/ratcheting effect.

## 4.4 Results of Fractographic Examinations

The results of the fractographic examinations described in Section 3.3.5 are detailed in this Section.

### 4.4.1 Macroscopic Examinations

The uniaxial stress-strain curve in Fig. 4.1 indicates that the material used, SAE 1045 steel with hardness Rc 37, is ductile. This indicates that a large amount plastic deformation occurred preceding final failure. The fracture surface of a ductile tension specimen generally has a cup-and-cone appearance. This cup-and-cone appearance is due to stress state shifting from uniaxial to triaxial in the necking section after the ultimate tensile strength is surpassed. The resulting highest shear stress in the necked section occurs at the center of the cross-section and causes microvoids nucleation, growth, and coalescence, or center cracks [38]. The cracks spread outward towards the surface of the necked-down area if the monotonic load continuously increases. Before the fracture reaches the surface of the specimen, the fracture suddenly changes direction from the generally transverse to the maximum shear stress direction (45°from the surface). It is the slant fracture, termed as "shear lip", that forms the cup-and-cone shape characteristic of ductile metal tensile fractures [39].

Unlike the fracture surfaces of the smooth specimens, the sharply notched samples did not exhibit a cup-and-cone fracture surface. Due to the large magnitude of

triaxial stresses located near the notch root, the crack was initiated at notch root and progressed towards the interior, resulting in the final fracture being located in the center of the cross section as shown in Fig. 4.16.

Figures 4.17 and 4.18 show the fracture surfaces of the short-life ($<10^4$ cycles) notched fatigue samples at both R ratios. It can be seen from these figures that fracture surfaces of the notched high mean stress specimens under both R ratios are very similar in appearance to those of the monotonic failures. This result was also reported in [10-12]. Large splits of approximately 3mm in length can be observed at the center of these fracture surfaces in the hot-rolling direction, which are caused by triaxial stresses. Adjacent to the splits (position A), knap like features (position B), approximately 1-2 mm in height, exist on the fracture surfaces of the monotonic and short-life samples. One side of these extrusive feature is perpendicular to the fracture surface (arrow 1), while the other side has approximately a $45^\circ$ slope (arrow 2). The extrusive features are the final fracture regions caused by the shear stresses. In the flat fracture region, many small sized splits exist.

Significant differences can be seen between the fracture surfaces of the short-life and long-life fatigue samples shown in Figs. 4.17-4.20. Specifically, the extrusive features around the central regions of the monotonic tension (Fig. 4.16) and short-life fatigue fractures (Figs. 4.17-1.18) declined with the increase of fatigue lives (Figs. 4.19-4.20) for both R ratios. It can be seen in Figs. 4.19 and 4.20, two different regions are present on the fracture surfaces of the long-life specimens, a crack growth region and a final fracture region. The fatigue crack growth region is located at the rim portion of the fracture surface as indicated by arrows in Figs. 4.19-4.20. The fatigue cracks initiated at

the rim portion and developed towards the central region. The final fracture region is at the central portion, which is caused by a sudden fracture of the specimen following crack growth. Comparing the two regions, the final fracture region is more fibrous than the outer region. Small size splits are also observed in the central region. It can be seen in Figs. 4.19 and 4.20 that the fatigue crack growth regions are symmetric about the center of the cross section. That is, the cracks propagated evenly from the circumferential notch root to the center. This indicates that the test apparatus was in good alignment during cyclic loading and bending stresses were not present.

### 4.4.2 Microscopic Examinations

The notched monotonic and cyclic specimens were examined microscopically to obtain more information about their fracture morphology. All microscopic observations were done at 1500x magnification. Two kinds of fracture modes were observed from these fractures surfaces, dimple rupture and fatigue. The dimple rupture is principally caused by overload where most common structural alloys fail by a process known as microvoid coalescence. The microvoids nucleate at the locations of localized strain discontinuity such as inclusions, grain boundaries, and dislocation pile-ups. As the strain in the material increases, the microvoids grow, coalesce, and eventually form a continuous fracture surface. This type of fracture exhibits numerous cuplike depressions that are caused by microvoid coalescence. The cuplike depressions are referred to as dimples, and the fracture mode is known as dimple rupture [38]. Unlike the dimple rupture forming process, the fatigue fracture is the result of repetitive or cyclic loading. A fatigue fracture generally occurs in three stages: initiation, propagation, and final rupture

[39]. The fatigue crack is initiated by repetitive shear stresses and all parallel to the shear stress direction. As the repetitive loading continues, the direction of tiny crack formed in the first stage changes to be perpendicular to the tensile stress direction in the propagation stage. As a result, fatigue striations, very tiny and closely spaced ridges, are formed. As the propagation of the fatigue crack continues, the area of the cross section is gradually reducing until final fracture occurs.

Figures 4.21-4.23 show the SEM views of the rim regions close to the notch tip for the monotonic, short-life, and long-life specimens, respectively. For the monotonic specimen (Fig. 4.21), dimple rupture mode, dominated by dimples and microvoids, can be observed. A large sized void, caused by the maximum shear stress, also exists on the monotonic notched specimen. Comparing the rim regions of the monotonic sample (Fig. 4.21) to that of the short life (Fig. 4.22) sample, similar features such as dimples and microvoids can be observed. However, a very different fracture morphology can be seen at the rim regions of the long-life sample (Fig. 4.23) where fatigue striations dominate.

Figures 4.24-4.26 show the representative central final fracture surfaces of the monotonic and the fatigue specimens for both short and long-life at R=0.7 and 0.8. As seen in these figures, all fracture surfaces are dominated by the ductile dimples, which indicates that the final fracture mechanism for all monotonic and fatigue specimens is dimple rupture fracture. Some large and small sulfide inclusions can be seen in the final fracture regions, which serve as microvoid-nucleating sites.

### 4.1.1 Summary

According to the appearances of the fracture surfaces, the fatigue specimens can

be classified as short-life or long-life. The fracture surfaces of the short-life specimens were similar in appearance to the monotonic tension fracture, where dimple rupture dominated the whole fracture area. Large splits existed at the central region of fracture surfaces of the monotonic and the short life specimens. Fatigue striations were observed on the fracture surfaces of the long-life specimens around the rim of the cross section. The fatigue crack propagated towards the center along the notch circumference. The appearances of the central regions, or the final fracture, were similar for the monotonic, short-life, and long-life specimens and were dominated by the dimple ruptures. Since fatigue striations did not exist on the fracture surfaces of the short life samples and the crack propagation lives of the long life samples were small, the strain-life method of fatigue analysis, a crack initiation method, seems to be the most appropriate method to use for the fatigue life prediction of the samples.

| Monotonic Property | SAE 1045 Steel |
|---|---|
| Hardness (Rc) | 37 |
| Elastic Modulus, E (GPa) | 207 |
| Yield Stress, $S_y$ (MPa) | 1147 |
| Ultimate Stress, $S_u$ (MPa) * | 1222 |
| True Fracture Strain, $\varepsilon_f$ | 0.578 |
| Strength Coefficient, K (MPa) * | 1342 |
| Strain Hardening Exponent, n * | 0.0269 |

Note: * Result from one tensile test

Table 4.1 Monotonic Properties of Hardened SAE 1045 Steel

| Total Strain Amplitude, $\Delta\varepsilon/2$ (mm/mm) | Stress Amplitude, $\Delta S/2$ (MPa) | Plastic Strain Amplitude, $\Delta\varepsilon_p/2$ (mm/mm) | Reversals to Failure, $2N_f$ |
|---|---|---|---|
| 0.0100 | 915 | 0.00584 | 514 |
| 0.0087 | 855 | 0.00449 | 1,504 |
| 0.0070 | 802 | 0.00299 | 2,788 |
| 0.0061 | 767 | 0.00241 | 5,000 |
| 0.0049 | 753 | 0.00126 | 8,530 |
| 0.0048 | 723 | 0.00135 | 8,344 |
| 0.0044 | 704 | 0.00102 | 25,240 |
| 0.0039 | 744 | 0.00026 | 34,882 |
| 0.0030 | 621 | 0.00000 | 162,664 |

Table 4.2 Fully Reversed Fatigue Test Results

| Material / Parameters | SAE 1045 Steel (Rc 37) |
|---|---|
| Fatigue Strength Coefficient, $\sigma_f^{'}$ (MPa) | 1421 |
| Fatigue Strength Exponent, b | -0.0713 |
| Fatigue Ductility Coefficient, $\varepsilon_f^{'}$ | 0.4083 |
| Fatigue Ductility Exponent, c | -0.6331 |
| Cyclic Strength Coefficient, $K^{'}$ (MPa) | 1773 |
| Cyclic Strain Hardening Exponent, $n^{'}$ | 0.134 |
| Cyclic Yield Strength, $S_y^{'}$ | 771 |

Table 4.3 Test Specimens Cyclic and Fatigue Properties

| No. | R ratio | $S_{max}/S_{un}$ (%) | $S_{max}$ (MPa) | $S_m$ (MPa) | $S_a$ (MPa) | $S_m/S_{un}$ (%) | $S_m/S_u$ (%) | Life (cycles) |
|---|---|---|---|---|---|---|---|---|
| #11 | 0.8 | 0.95 | 2076 | 1868 | 208 | 0.85 | 1.53 | 1,857 |
| #6 | 0.8 | 0.95 | 2076 | 1868 | 208 | 0.85 | 1.53 | 3,737 |
| #2 | 0.8 | 0.9 | 1967 | 1770 | 197 | 0.81 | 1.45 | 5,817 |
| #3 | 0.8 | 0.85 | 1857 | 1672 | 185 | 0.77 | 1.37 | 11,411 |
| #9 | 0.8 | 0.8 | 1748 | 1573 | 175 | 0.72 | 1.29 | 13,687 |
| #12 | 0.8 | 0.75 | 1639 | 1475 | 164 | 0.68 | 1.21 | 20,613 |
| #14 | 0.8 | 0.65 | 1420 | 1278 | 142 | 0.59 | 1.05 | 36,535 |
| #16 | 0.8 | 0.55 | 1202 | 1082 | 120 | 0.50 | 0.89 | 62,412 |
| #5 | 0.8 | 0.45 | 983 | 885 | 98 | 0.41 | 0.72 | 115,804 |
| | | | | | | | | |
| #17 | 0.7 | 0.95 | 2076 | 1764 | 311 | 0.81 | 1.44 | 1,165 |
| #7 | 0.7 | 0.9 | 1967 | 1672 | 295 | 0.77 | 1.37 | 2,800 |
| #8 | 0.7 | 0.8 | 1748 | 1486 | 262 | 0.68 | 1.22 | 5,895 |
| #15 | 0.7 | 0.7 | 1530 | 1300 | 229 | 0.60 | 1.06 | 10,144 |
| #4 | 0.7 | 0.6 | 1311 | 1114 | 197 | 0.51 | 0.91 | 18,560 |
| #13 | 0.7 | 0.5 | 1093 | 929 | 164 | 0.43 | 0.76 | 33,136 |
| #10 | 0.7 | 0.4 | 874 | 743 | 131 | 0.34 | 0.61 | 57,577 |

Table 4.4 High Mean Stress Fatigue Test Results

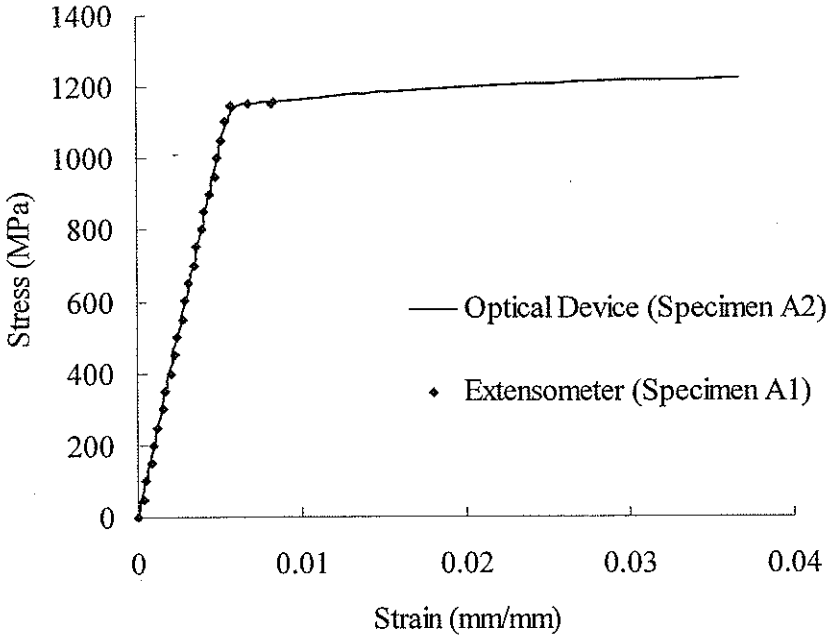


Figure 4.1 Stress-Strain Curves of a Smooth Monotonic Sample

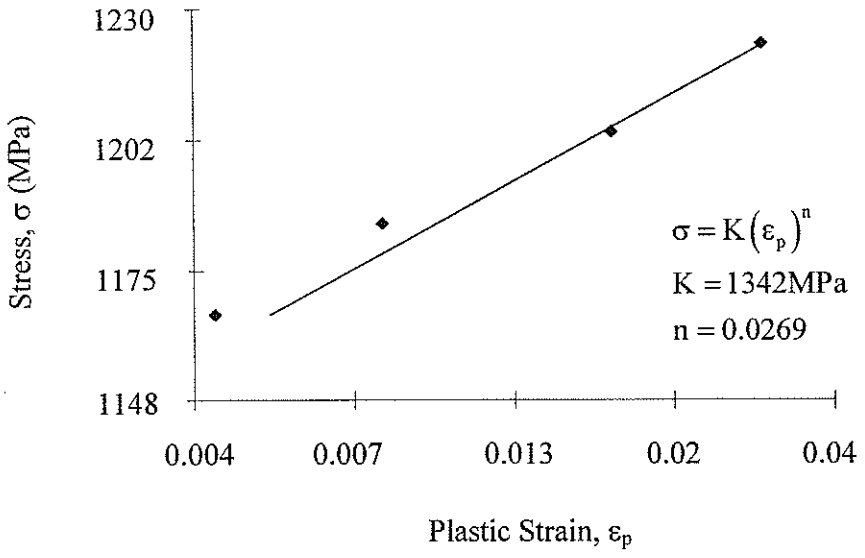


Figure 4.2 Stress versus Plastic Strain Behavior for Hardened SAE 1045 Steel

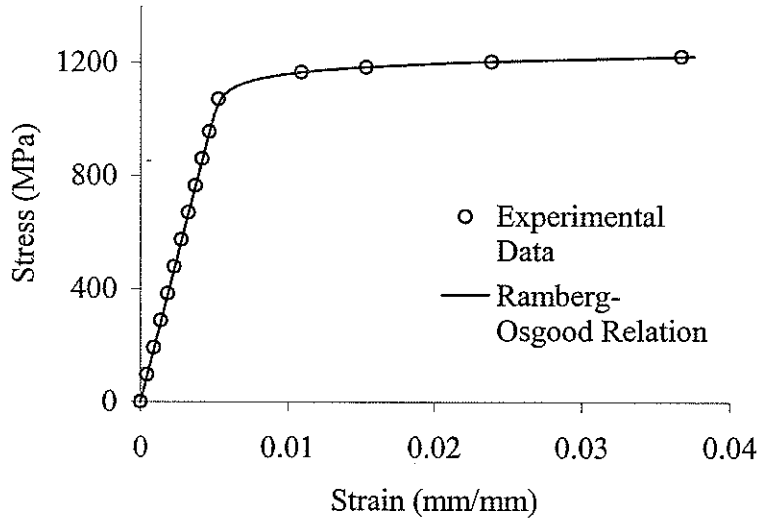


Figure 4.3 Uniaxial Stress-Strain Curve and Ramberg-Osgood Relation

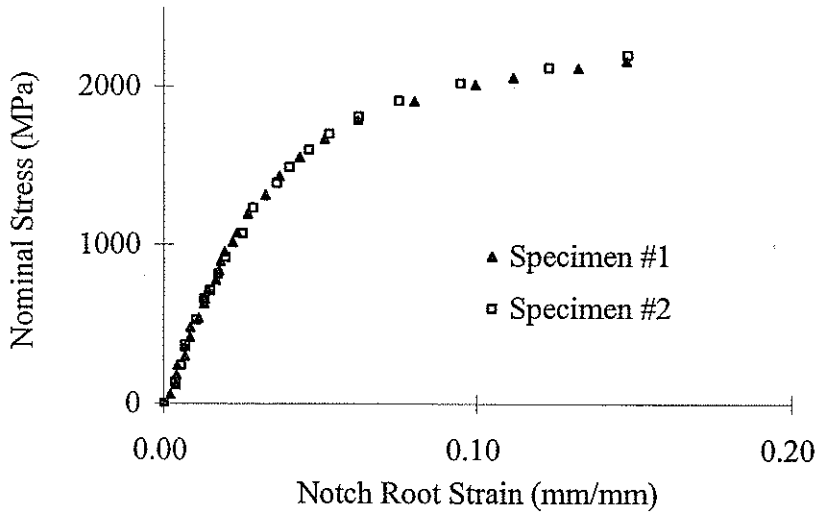


Figure 4.4 Stress versus Strain Curves of Sharply Notched Specimens

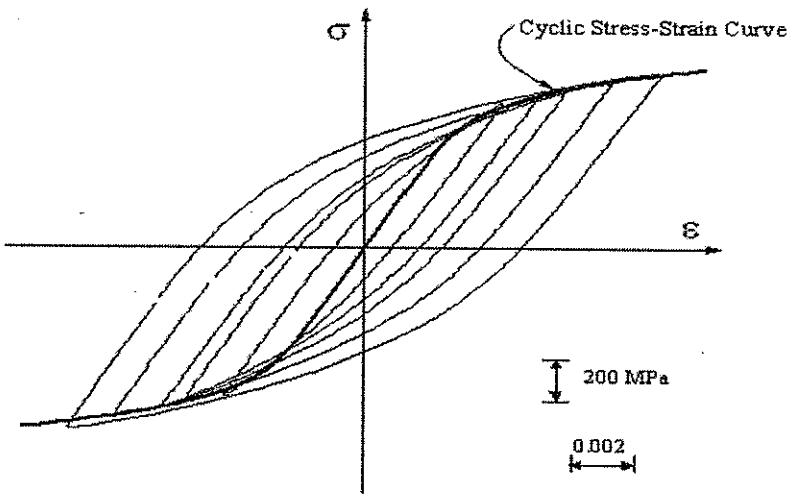


Figure 4.5 Stable Hysteresis Loops

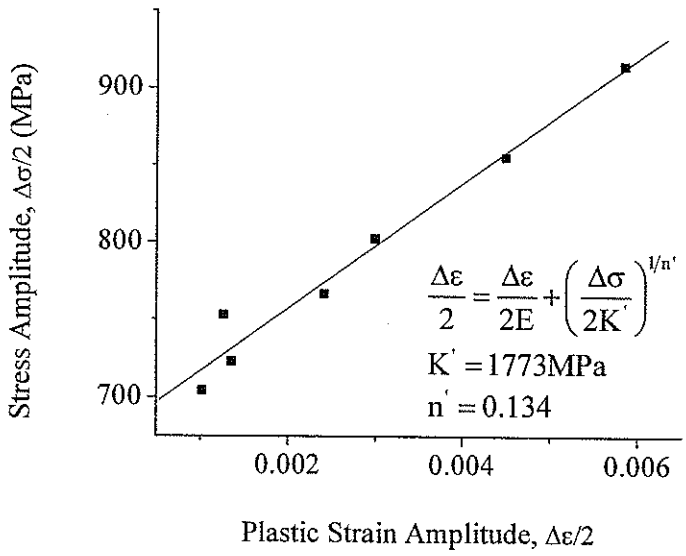


Figure 4.6 Stress Amplitude versus Plastic Strain Amplitude Behavior for Hardened SAE 1045 Steel

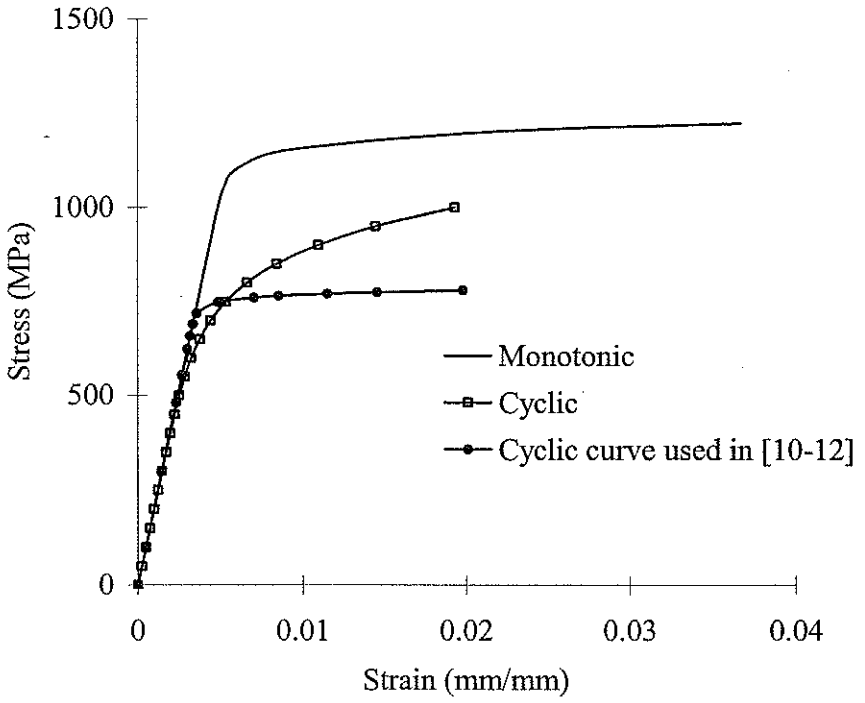


Figure 4.7 Monotonic and Cyclic Stress-Strain Curves

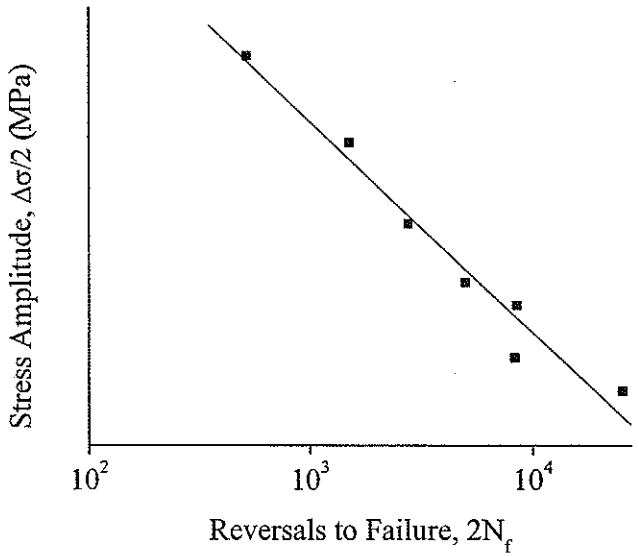


Figure 4.8 Stress Amplitude versus Reversals to Failure for Hardened SAE 1045 Steel

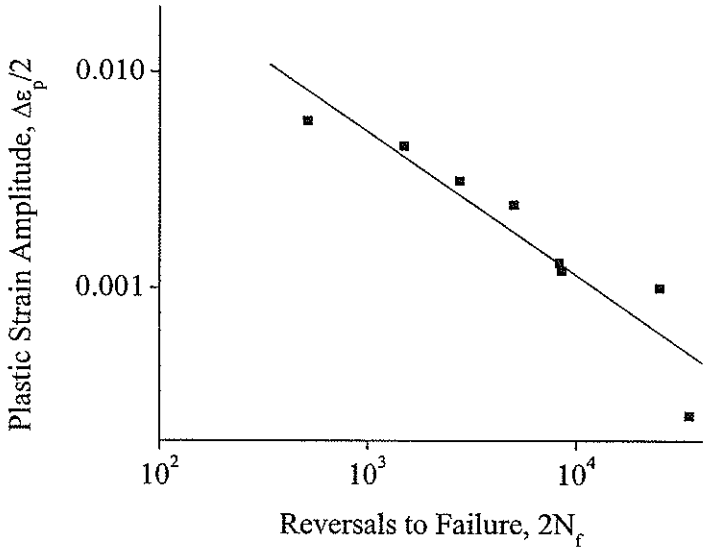


Figure 4.9 Plastic Strain Amplitude versus Reversals to Failure for Hardened SAE 1045 Steel

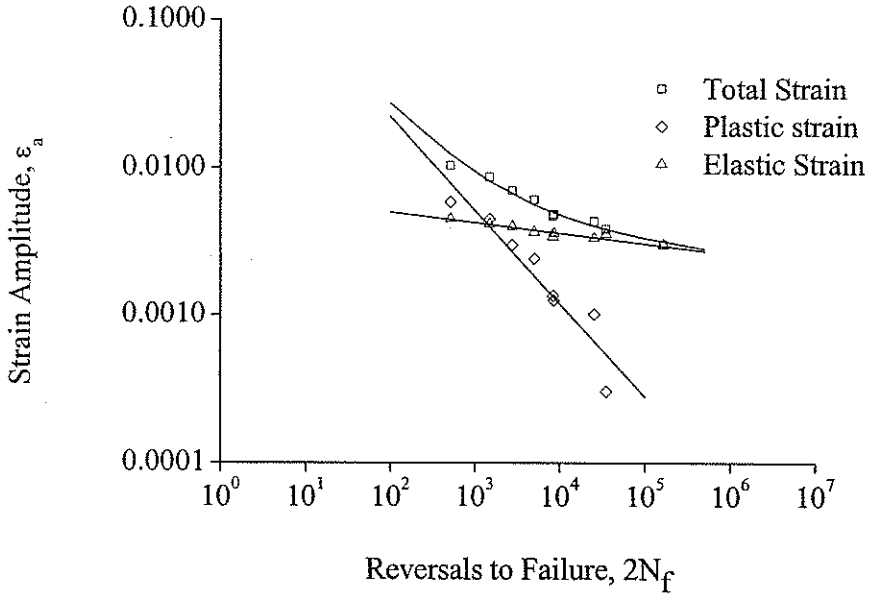


Figure 4.10 Strain-Life Curves Showing Total, Elastic and Plastic Strain Components

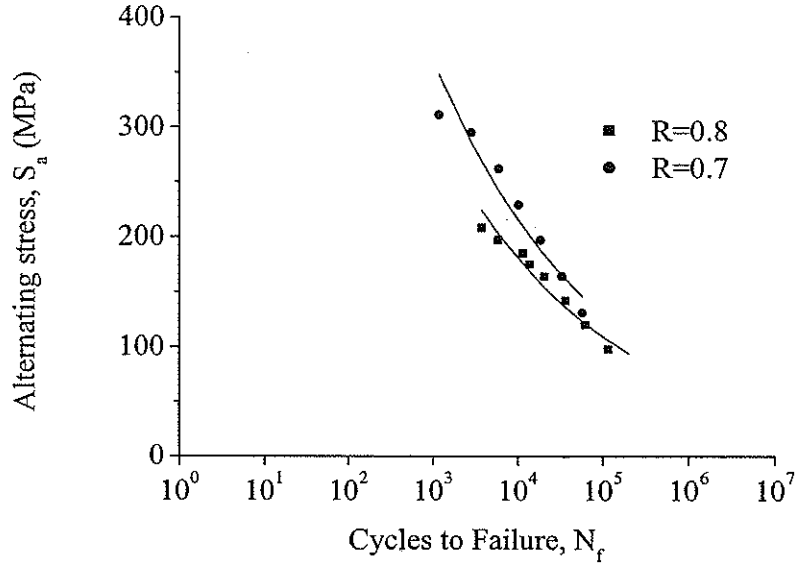


Figure 4.11 $S_a$-N Curves

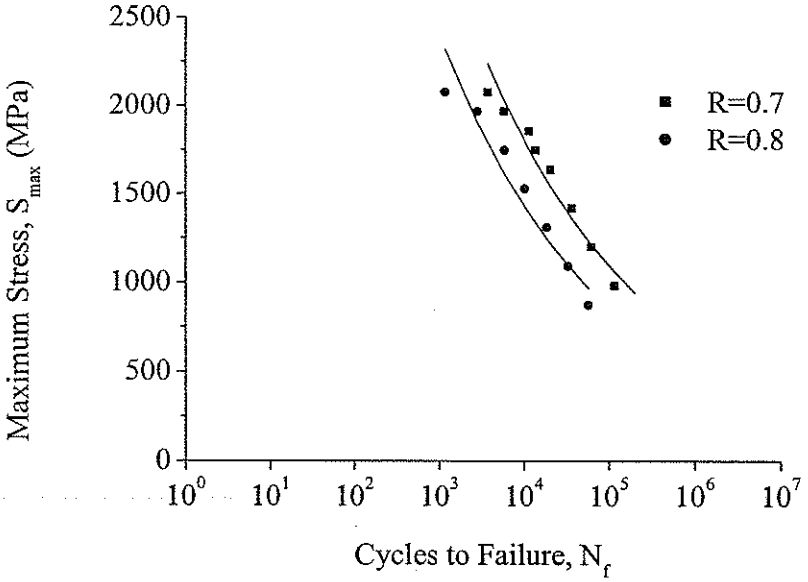


Figure 4.12 $S_{max}$-N Curves

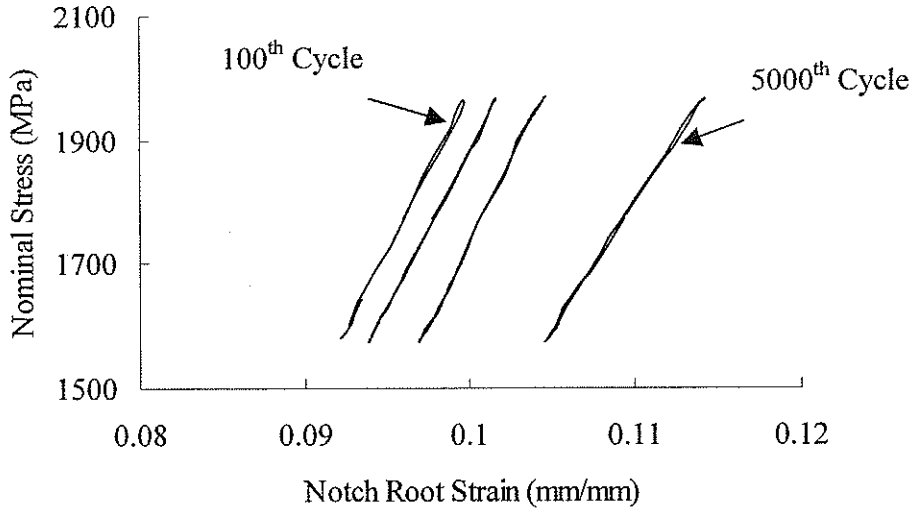


Figure 4.13 Stress versus Strain Hysteresis Loops for #6 Sample

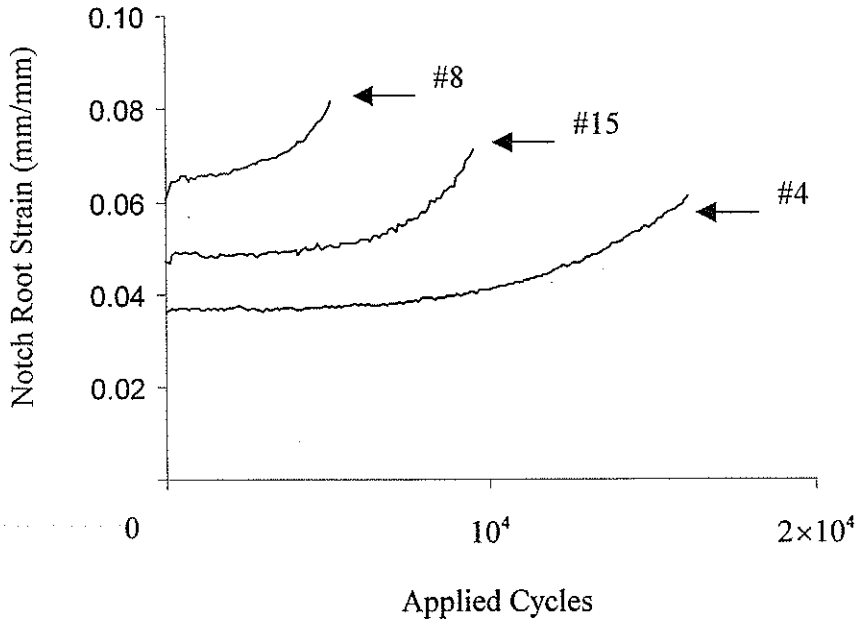


Figure 4.14 Strain versus Applied Cycles for R=0.7

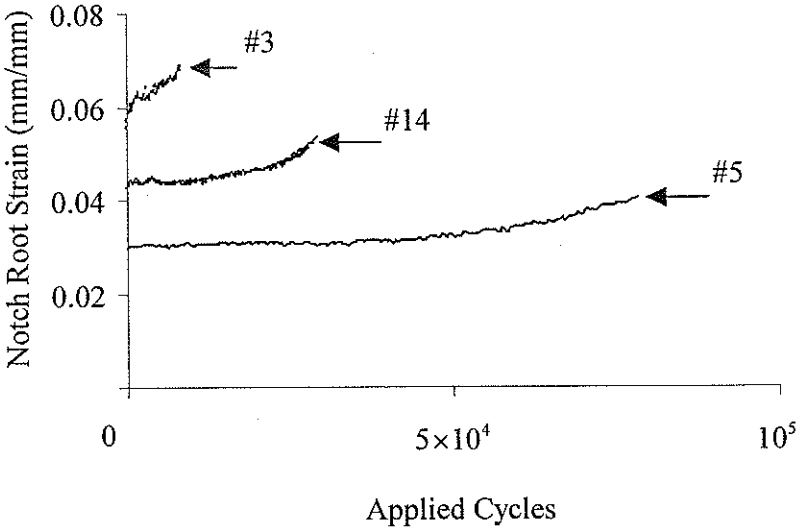


Figure 4.15 Strain versus Applied Cycles for R=0.8

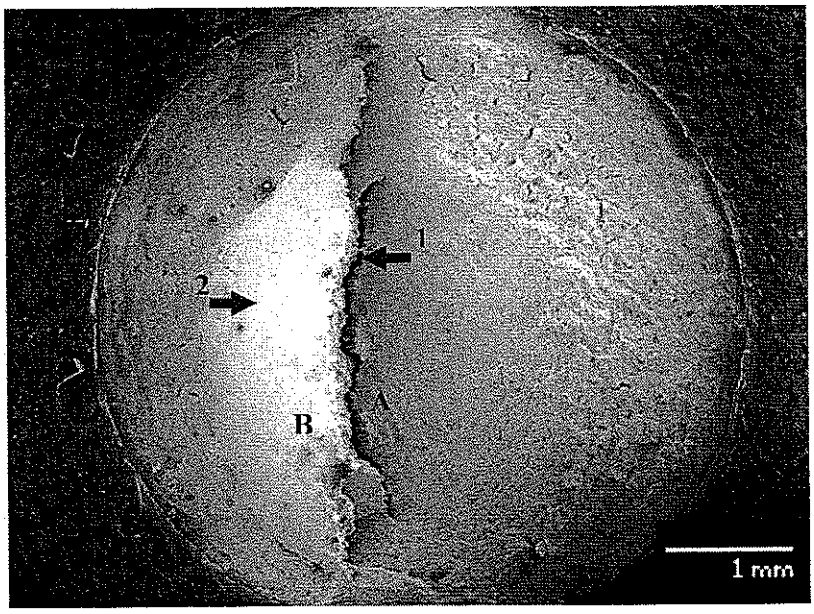


Figure 4.16 Macroscopic View of a Notched Monotonic Tension Sample

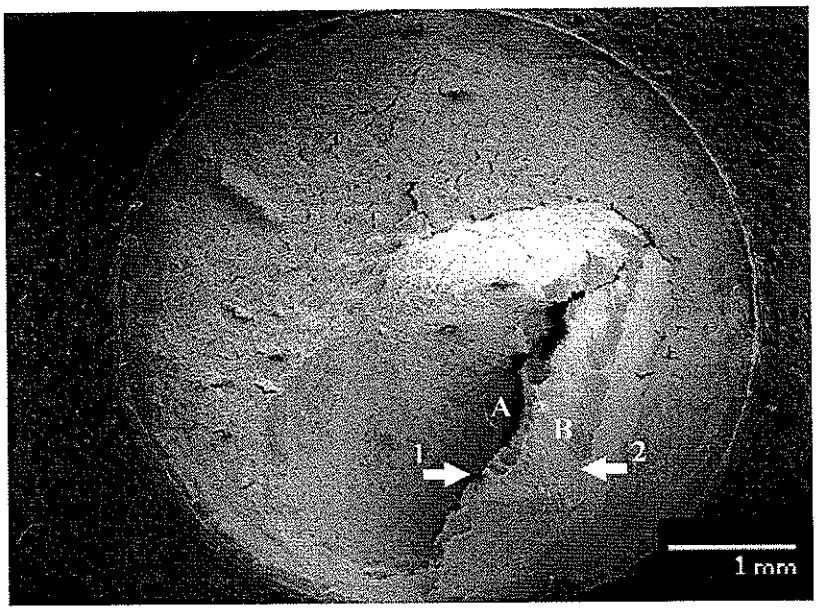


Figure 4.17 Macroscopic View of Short Life Fatigue Sample (R=0.7, #7)

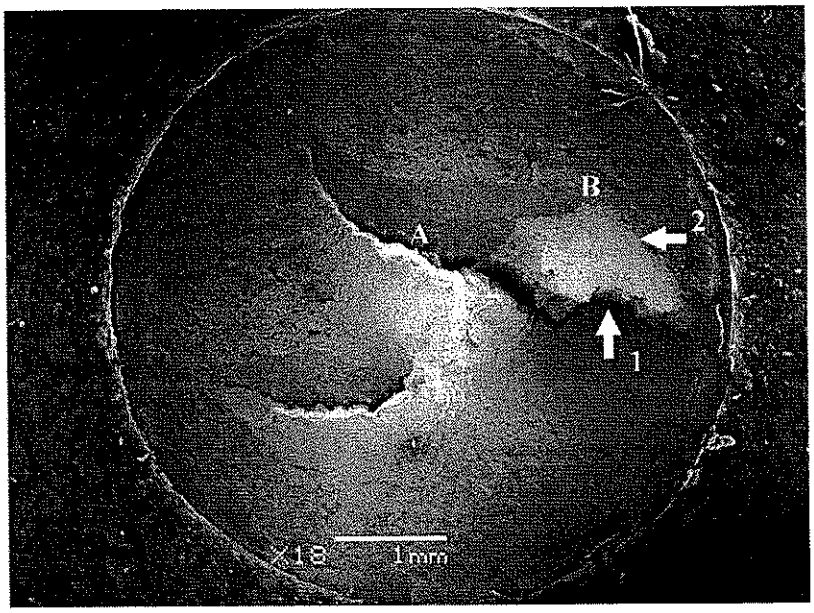


Figure 4.18 Macroscopic View of Short Life Fatigue Sample (R=0.8, #6)

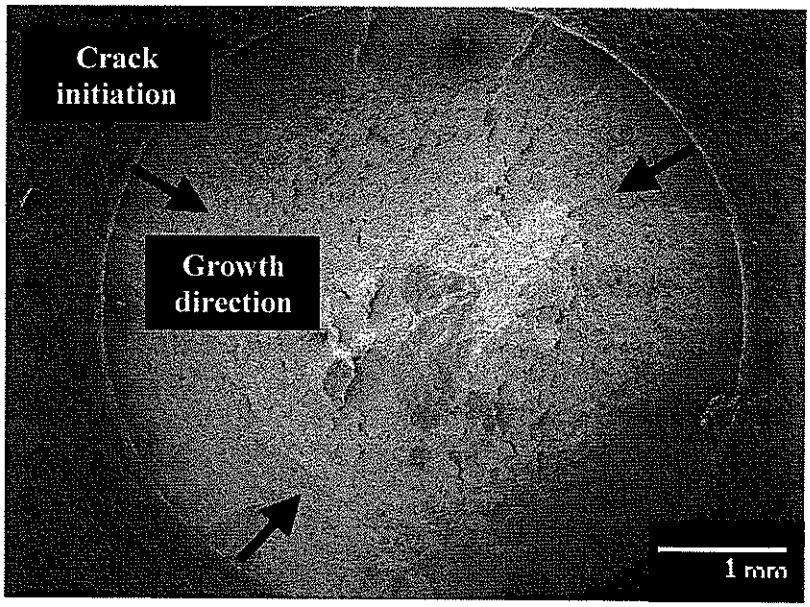


Figure 4.19 Macroscopic View of Long Life Fatigue Sample (R=0.7 #10)

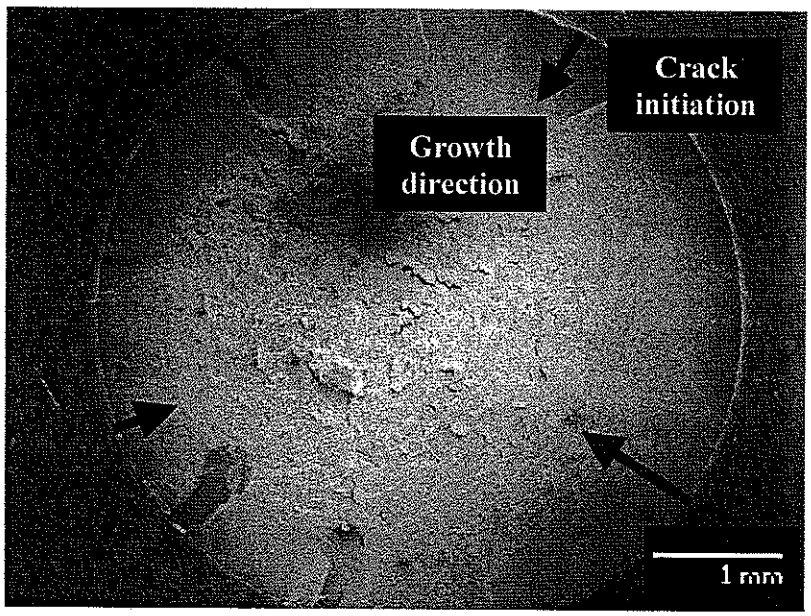


Figure 4.20 Macroscopic View of Long Life Fatigue Sample (R=0.8, #5)

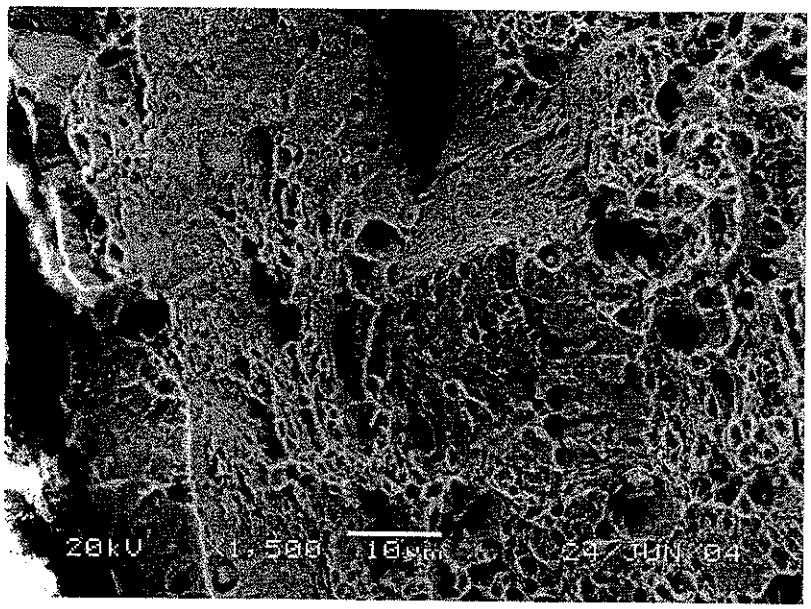


Figure 4.21 Microscopic View of Rim Region of Notched Monotonic Tension Sample

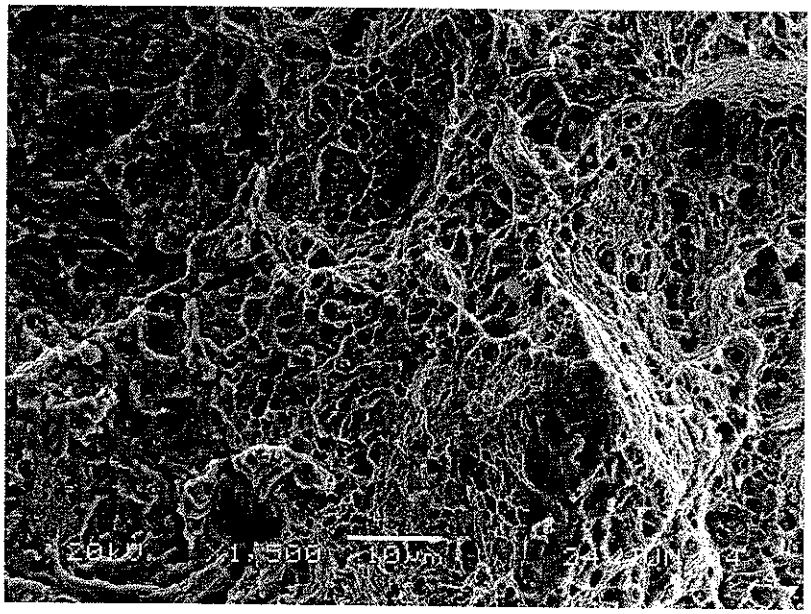


Figure 4.22 Microscopic View of Rim Region of Short Life Fatigue Sample
(R=0.8, #6)

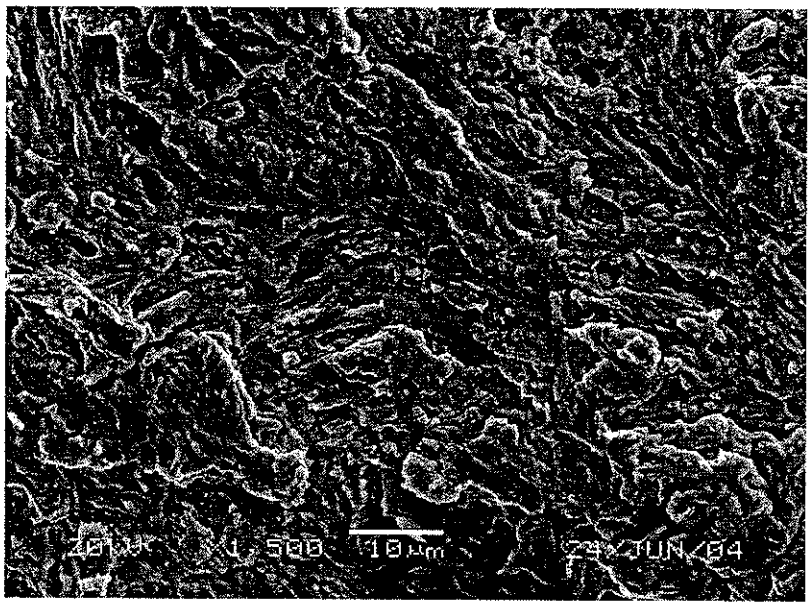

Figure 4.23 Microscopic View of Rim Region of Long Life Fatigue Sample
(R=0.8, #5)

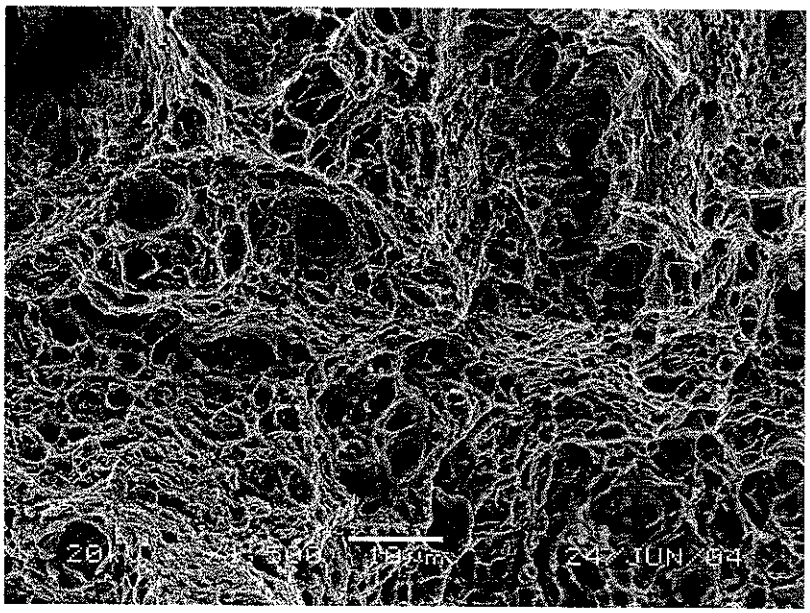

Figure 4.24 Microscopic View of Final Fracture Region of Notched Monotonic Sample

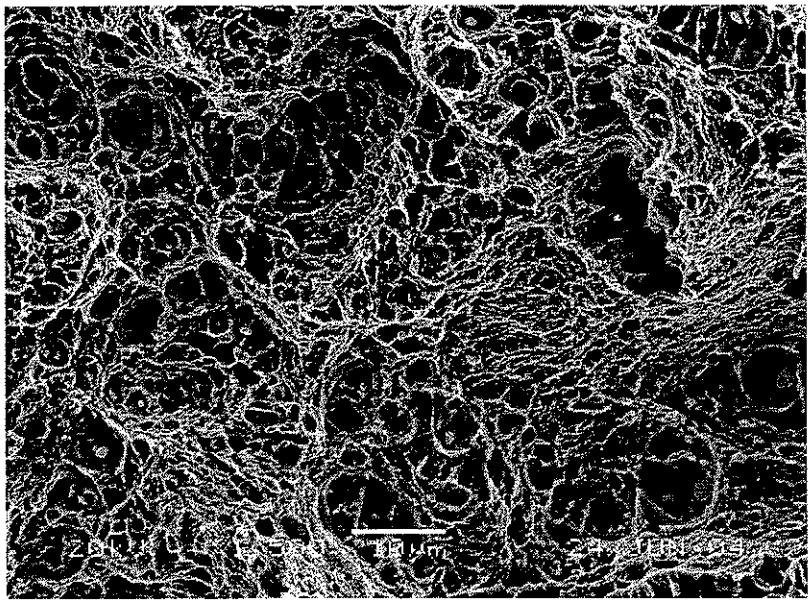

Figure 4.25 Microscopic View of Final Fracture Region of Short Life Fatigue Sample (R=0.8, #6)

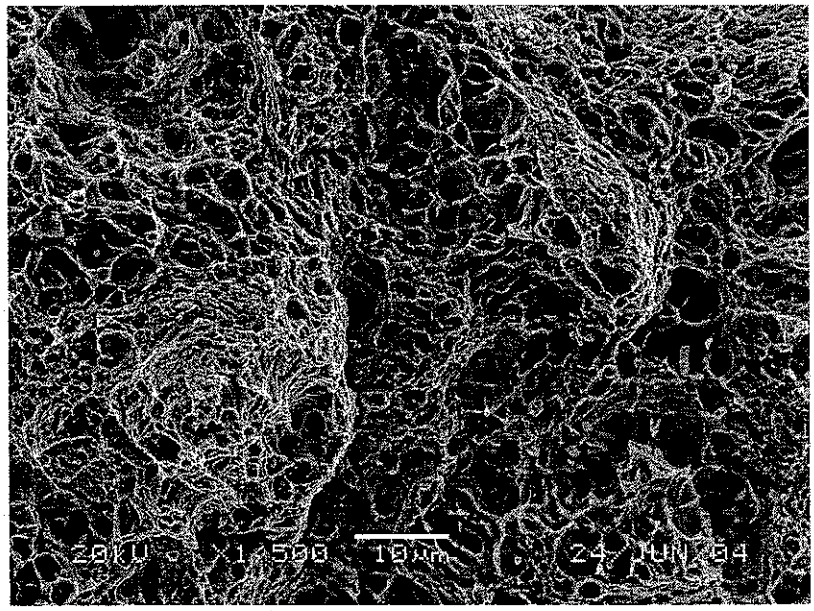


Figure 4.26 Microscopic View of Final Fracture Region of Long Life Fatigue Sample (R=0.8, #5)

# CHAPTER FIVE

# FATIGUE LIFE CALCULATIONS AND DISCUSSION

The primary objective of this study is to evaluate the validity of fatigue life prediction models in high mean stress, high R ratios applications. In this chapter, the stress-life and strain-life methods of fatigue analysis, detailed in Chapter Two, are used to predict the lives of the sharply notched samples. The predictions are compared to those experimentally determined in Chapter Four. Based on the comparison a discussion is presented that provides guidance on the methods of correct application, and the limitations and strengths of each method for use in high mean stress applications.

The stress concentration factors of the sharply notched specimens are first determined in Section 5.1 since their use is necessary in both the stress-life and strain-life methods. Sections 5.2 and 5.3 provide details of the S-N and ε-N life calculations respectively and give a comparison between the calculations and the experimental results. Finally, Section 5.4 provides the conclusions of this chapter.

## 5.1 Determination of Stress Concentration Factors

The sharp 60° V-shaped notch with a 0.25mm root radius introduces a large elastic stress concentration. For the sharply notched specimen subjected to a uniaxial load, there are two elastic stress concentration factors that need to be defined. Referring to the notation in Fig. 2.2, one factor, $K_{t22}$, addresses the local stress in the direction of applied load ($\sigma_{22}$), and the other factor, $K_{t33}$, addresses the local stress in circumferential direction ($\sigma_{33}$). These concentration factors are defined as,

$$K_{t22} = \frac{\sigma_{22}}{S}, \tag{5.1}$$

and

$$K_{t33} = \frac{\sigma_{33}}{S}. \tag{5.2}$$

In Eqs. (5.1) and (5.2), S is taken as the net section nominal stress. There are three methods of determining these elastic stress concentration factors. These include applying closed formed equations, preparing a linear finite element model of the test specimen, and finally performing experimental measurements.

The axial stress concentration factor was first calculated using the approximate formulae provided by Noda and Takase [40]. The value of $K_{t22} = 3.72$ was given by their approximate formulae. However, the approximate formula for the circumferential stress concentration factor was not available in their paper.

In order to determine both stress concentration factors of the sharply notched specimen, an elastic finite element analysis (FEA) was performed. Commercial software ABAQUS 6.3 [41] was used to perform the finite element analysis. Specifically it was used to draw the geometry of the model, mesh the model, apply the boundary conditions, and calculate the notch root stresses. Due to the symmetry in geometry and loading, the circumferentially notched round bar was modeled by using the axisymmetric two-dimensional model shown in Fig. 5.1.

As shown in Fig. 5.1, the section was divided into several partitions before meshing. The critical notch root area was partitioned into an approximate 0.25x0.25mm square region. Two kinds of elements were used in this finite element model, 3-noded

linear axisymmetric triangles and 4-noded bilinear axisymmetric quadrilaterals. Since a very high stress gradient exists around the notch root, a fine mesh was required in that region to obtain accurate results. Four-noded bi-linear axisymmetric quadrilateral elements having $1x10^{-3}$ mm edge length were used to mesh the notch root region; the other portions in this model were meshed using 3-node linear axisymmetric triangle elements. The mesh scheme for this FEA model is shown in Fig. 5.2.

As shown in Fig. 5.1, a uniform tensile stress was applied to the upper edge of the section to simulate the applied load. The boundary conditions applied to the lower edge restricted displacement in 2 direction and rotations about the 1 and 3 axes. To calculate the elastic stress concentration factors, an ideal linear material law was assigned to this finite element model. The elastic modulus (E=207 GPa, Table 4.1) used in the finite element model was taken from the experimental data. The stress distribution of the elastic FEA is shown in Fig. 5.3. The stress values at the notch tip node were taken as the local maximum stresses, which are the interpolated values from the integration points of the notch tip element. According to Eqs. (5.1) and (5.2), the elastic stress concentration factors in the axial and circumferential directions were calculated to be $K_{t22} = 3.64$ and $K_{t33} = 1.14$, respectively.

Finally, an attempt has been made to determine the elastic stress concentration factors using the experimental measurements. To do so, the notch root axial strain, $\varepsilon_{22}$, and circumferential strain, $\varepsilon_{33}$, obtained from the optical measurements before yielding, were substituted into the Hooke's law given as,

$$\varepsilon_{22} = K_{t22}S/E - \nu(K_{t33}S)/E$$
$$\varepsilon_{33} = K_{t33}S/E - \nu(K_{t22}S)/E \tag{5.3}$$

In Eq. (5.3), $\nu = 0.3$ is the Poisson ratio of this material. It should be noted that the local yield stress was calculated according to von Mises yielding criterion with the stress concentration factors determined by FEA. This calculation was necessary to insure that the experimental strain data used in Eq. (5.3) were obtained before yielding. The circumferential strains were found to be fluctuating about zero instead of increasing linearly with the applied loads below yielding point. Thus, the elastic stress concentration factors were calculated only using axial strain values assuming circumferential strain values were zeros. The stress concentration factors were found from one monotonic tension test as $K_{t22} = 3.61$ and $K_{t33} = 1.08$. The other test yielded $K_{t22} = 3.32$ and $K_{t33} = 0.99$.

Table 5.1 presents the stress concentration factors obtained from the aforementioned three methods and the percentage differences among these values referring to the experimental results. As can be seen from Table 5.1, three methods provide close results with a maximum 7.2 % difference of $K_{t22}$ and a 9.6 % difference of $K_{t33}$. In this research, the stress concentration factors calculated using the elastic FEA are used instead of those experimentally determined. The FEA results were used since the goal is to solely evaluate the analytical solution methodologies and the experimental results are often not available in design.

## 5.2 Stress-Based Models

There are two steps involved in determining the fatigue life of notched specimens using the S-N method. The first step is to determine the parameters in Basquin's equation; the second step is to combine the mean stress correction models with Basquin's equation to calculate the fatigue lives.

Basquin's equation (Eq. (2.32)) based on reversals, $2N_f$, was used in the life calculation since the parameter values of b and $\sigma_f'$ were obtained by the fully reversed fatigue tests described in Section 3.3.3 and these values are given in Table 4.3. For notched members, Basquin's equation needs to be modified to account for the notch effect. It is estimated that the fatigue strength of notched member is equal to that of smooth member at one reversal and that fully reversed fatigue strength of notched member is $S_f/K_f$ at long life ($10^6 \sim 10^8$) [3]. The modified Basquin's equation for notched member under fully reversed loading conditions thus can be given as,

$$S_{Nf} = \sigma_f'(2N_f)^{b_0}. \tag{5.4}$$

In Eq. (5.4), $S_{Nf}$ is the fully reversed fatigue strength of notched member at $N_f$ cycles and $b_0$ is the slope of the notched S-N curve in a log-log scale. In order to determine the value of $b_0$, it is assumed that the fully reversed fatigue strength of notched member is equal to $S_f/K_f$ at $10^6$ cycles as,

$$S_f/K_f = \sigma_f'\left(2\times10^6\right)^{b_0}. \tag{5.5}$$

In Eq. (5.5), $S_f = 505$ MPa was calculated by Eq. (2.32) with $N_f = 10^6$ and $K_f = 3.09$ was found by Eq. (2.7). Thus the value of $b_0$ was found to be –0.1491. It should be noted that wrong published data was used in [12].

The S-N mean stress correction models detailed in Section 2.1 were used to perform the fatigue life calculations of the sharply notched specimens under high mean stress and high R ratio conditions. To do so, the S-N mean stress correction models including the Modified Goodman (Eq. (2.2)), Gerber (Eq. (2.3)), and Morrow (Eq. (2.4)) models were combined with the modified Basquin's equation (Eq. (5.5)). Since Cook and Gunn's equations were developed to take into account the notch effect, they can be applied to calculate the fatigue lives of notched members by directly replacing $S_f$ with Basquin's equation Eq. (2.32).

The results of the life calculations using the S-N models are listed in Table 5.2, including the Modified Goodman, the Gerber, the Morrow, Cook's, and Gunn's models. It should be noted that the Modified Goodman (Eq. (2.2)) and Gerber (Eq. (2.3)) models could not be used for many of the life calculations since the applied $S_m$ is greater than $S_u$ and thus the models resulted in physically meaningless negative values for $S_f$. Slightly modified versions of the Modified Goodman and Gerber models have been proposed [10-12]. The modification involves simply replacing $S_u$ with $S_{un}$ in each mean stress correction model. These calculations were also conducted and are presented in the table.

The true fracture strength used in the Morrow model (Eq. (2.4)) was taken as $\sigma_f = 1620$ MPa [11]. Similar to the Goodman and Gerber models, the Morrow model also could not be used for life calculations when the applied $S_m$ is greater than $\sigma_f$. In

addition, since the nominal mean stress applied to many specimens was beyond the range of validity of Cook and Gunn's models, the life calculations were performed when they were possible.

The experimental lives were plotted against the calculated lives in a log-log scale at R=0.8 and R=0.7 in Figs. 5.4 and 5.5 respectively. The diagonal lines in these plots indicate the condition where the experimental life is exactly the same as the calculated life. It indicates the experimental life is greater than the calculated life if data points are located above the diagonal line, and vice versa.

It can be seen from Table 5.2 and Figs. 5.4 and 5.5 that all of the existing S-N models could not provide accurate life predictions for the sharply notched specimens under high mean stress and high R ratios conditions where large scale plastic deformation exists. As shown in Table 5.2, the fatigue lives of two samples at R=0.8 and three samples at R=0.7 are calculated using the Modified Goodman and Gerber models, where the applied mean stresses are lower than the ultimate strength. The calculated lives by the Modified Goodman model are one to four orders of magnitude different from actual lives. The Gerber model calculated lives are within three orders of magnitude difference from actual lives. The slightly modified versions of the Modified Goodman and Gerber models, replacing $S_u$ with $S_{un}$ in these equations, provide better life predictions for all samples for both R ratios with less than two orders of magnitude difference from actual lives. The sample fatigue lives where the applied mean stresses are less than $\sigma_f$ are calculated using the Morrow model and the calculated lives are up to four orders of magnitude different from actual lives. As can been seen in Table 5.2 and Figs 5.4 and 5.5, Gunn's model provides better prediction compared with Cook's equation. The Gunn's

model calculated lives are within two orders of magnitude difference from actual lives, while Cook's model presents over three orders of magnitude difference.

As mentioned in Section 2.2.1, a biaxial stress state exists at the notch root. An attempt was made to perform the S-N life calculations considering the biaxial stress state condition at the notch root. Specifically, $S_a$ and $S_m$ in the S-N mean stress correction models were replaced by the von Mises equivalent quantities at the notch root. However, the life calculations could not be performed since the calculated equivalent mean stresses were found to be greater than the notched ultimate strength. Negative values of $S_f$ were calculated and thus deemed meaningless. It should be noted that this method of calculation should yield better results than that obtained neglecting the circumferential stress.

### 5.3 Strain-Based Models

In Chapter Two, it was emphasized that two steps are required in the application of the strain-life method of fatigue analysis. Specifically the elastic-plastic notch root strain and stress history must first be obtained. The results can then be used in a strain-life model to predict the number of cycles a component can withstand before a crack initiates at a notch root. In this section, an evaluation of the relevant formulae, presented in Chapter Two, is conducted by comparing the results of the strain-based formulae to those obtained in the high mean stress experiments.

### 5.3.1 Evaluation of Elastic-Plastic Notch Root Strain and Stress Histories

As mentioned in Section 2.2.1, there are three methods for determining the elastic-plastic notch root strains and stresses that are necessary for performing a strain-based fatigue life calculation. These include experimental techniques, numerical techniques such as the finite element method, and approximate analytical techniques. Since approximate analytical techniques provide the simplest method of solution, they are most conducive for use in design environments. In this section, the approximate analytical techniques, described in Chapter Two, are applied to simulate the notch root elastic-plastic behavior of the high mean stress specimens tested. The results obtained are compared to those obtained using the finite element method and to the experimental results detailed in Chapter Four.

The FEA model used for elastic-plastic notch root strain-stress analysis was the same as that used to determine the elastic stress concentration factors. However, for the nonlinear elastic-plastic FEA, the monotonic constitutive law obtained from the monotonic tension test of the smooth specimen was used (Fig. 5.6). Since the monotonic stress-strain curve is very flat after the yielding point, the elastic-plastic portion was replaced by a straight line to simplify the complex nonlinear calculations. Figure 5.6 shows the simplified bi-linear material law used in the FEA model.

From the monotonic tension and fatigue tests of the sharply notched specimens, it was found that the circumferential strains were fluctuating about zero up until yielding. After the notch root material yielded, the circumferential strains increased with the applied loads and up to 5% of the axial strains at the ultimate load. In addition, the nonlinear elastic-plastic FEA shows that the ratio of the circumferential strain to axial

strain increases with the applied load and is less than 6% when the ultimate load is reached. In order to simplify the notch root stress and strain calculations, the circumferential strains can be neglected and it is assumed that the fatigue crack initiation is dominated by the axial strains. As a result, a plane strain assumption (Eq. (2.14)) can be made to represent the stress and strain states at the notch root. It should be noted that the plane stress assumption inaccurately neglects the circumferential stress ($\sigma_{33}$) in the sharply notched specimens. However, this assumption was inaccurately made in [12] to conduct the strain-based life calculations on geometrically identical notched bodies. As can be seen in Fig. 5.7, the notch root strains predicted using the methods in [12] for the initial loading are far from the experimental and FEA results when the stress ratio (the nominal stress to the yielding stress, $S/S_y$) is greater than 0.9. It should be noted that the applied maximum nominal stresses are greater than $0.9S_y$ for most of the tests performed in [12] that results in large-scale errors of life calculations.

The extended versions of Neuber's (Eq. (2.21)) and ESED (Eq. (2.22)) methods for the plane strain case were used to calculate the notch root stresses and strains. The multiaxial forms [19] did not need to be applied. The modified stress-strain relation, used in Eqs. (2.21) and (2.22), was obtained using the method in [18] to alter the uniaxial stress-strain relation given in Section 4.1.1 for the plane strain condition. The parameters, $K^* = 1577$ MPa and $n^* = 0.0307$, in the modified stress-strain relation were determined using a linear regression analysis as described in Section 4.1.1. The modified elastic modulus was calculated as $E^* = E/(1-\nu^2) = 227$ GPa, where E=207 GPa from Table 4.1.

The stress ratio ($S/S_y$) versus notch root axial strain curves, under monotonic loading conditions, obtained by experimental (average of two monotonic tension tests), FEA, and approximate analytical approaches are shown in Fig. 5.8. It can be observed that the curves obtained by FEA and experiment follow the same trend although a numerical gap exists. This difference may be due to the fact that the sharp notch root can be ideally modelled by FEA but impossible to be machined in reality. In addition, the smaller notch root strains obtained by the optical deformation measurement device may have been partly due to the fact that they were the average values of a very small area at the notch root. However, the notch root strains in the FEA were taken as the notch tip node strain values, where the highest strain exists. Comparing the two curves obtained by Neuber's rule and the ESED method in Fig. 5.8, the former overestimates, whereas the ESED method underestimates the notch root strains obtained using FEA until $S = 1.4S_u$. It can be observed that the ESED method provides a good correlation with the FEA results when the stress ratio is less than 1.25. However, the ESED method tends to give much smaller notch root strains than those obtained from FEA when the stress ratio is greater than 1.25. The ESED method provides a 55% difference referring to FEA results at the ultimate load. One reason is that large plastic deformations occur around the notch portion at high nominal stresses that makes the fundamental assumption of the simplified methods (localized plasticity) invalid. The other reason is that the material stress-strain curve cannot simulate the necking effect. It should be noted that these methods do predict a band approaching to notched ultimate strength, within which the FEA results fall. The average values of notch root strains predicted by Neuber's rule and the ESED method are also plotted against the stress ratios in Fig. 5.8. In addition, the strains, obtained using the

Hoffmann and Seeger method (Eqs. (2.26) - (2.31)) with the assumption of zero circumferential strain ($\varepsilon_{33} = 0$), were also plotted in Fig 5.8. The $K_p$ used in Eqs. (2.27) and (2.28) was determined by the same FEA model with an elastic perfectly-plastic material law. Though it was developed to specifically address the condition of net section yielding, the Hoffmann and Seeger method yields a more conservative prediction than the ESED method under the plane strain case.

In conclusion, the ESED method combined with the modified material stress-strain curve for the plane strain case gives the best prediction of the notch root elastic-plastic strains. It should be noted that the better prediction obtained from the ESED method may be for this specific geometry only. More generally, Neuber's rule and the ESED method when used together, predict a band within which the experimental notch root strains fall. As a result, the average value, in the middle of the band, may be used in design. The Hoffmann and Seeger results may be used as comparable data.

In order to perform the fatigue life calculations using the ε-N models, the local stress and strain values during cyclic loading need to be determined. Similar to the modified monotonic stress-strain curve for the plane strain condition, the modified cyclic stress-strain curve for the plane strain case was obtained by altering the cyclic stress-strain relation and is given in the Ramberg-Osgood form as,

$$\varepsilon = \frac{\sigma}{E^*} + \left(\frac{\sigma}{K^{*'}}\right)^{1/n^{*'}}, \tag{5.6}$$

where $K^{*'} = 2018\,\text{MPa}$, and $n^{*'} = 0.1386$.

It is assumed that the notch fatigue behavior of member may not be controlled by the local maximum stress but rather average stress acting over a finite volume of the material in the notch root region [3]. The fatigue notch factor which takes into account the stress gradient and localized plastic deformation at notch root, was suggested to replace the stress concentration factor in the strain-life fatigue analysis [16]. Thus the fatigue notch factor was used in the local stress and strain calculations in this study.

In order to account for the material softening effect, the cyclic stress-strain relation was used to calculate the local maximum stress and strain values during cyclic loading. Thus, the local maximum stress and strain at the notch root were determined by combining, for example, the ESED method (Eq. (2.19)) with the modified cyclic stress-strain equation as,

$$\begin{cases} \dfrac{\sigma_{max}^2}{E^*} + \dfrac{2\sigma_{max}}{n^{*'}+1}\left(\dfrac{\sigma_{max}}{K^{*'}}\right)^{1/n^{*'}} = \dfrac{(K_f S_{max})^2}{E^*} \\ \varepsilon_{max} = \dfrac{\sigma_{max}}{E^*} + \left(\dfrac{\sigma_{max}}{K^{*'}}\right)^{1/n^{*'}} \end{cases} \quad (5.7)$$

The local stress and strain ranges at the notch root were calculated by replacing stress and strain in Eq. (5.7) with their corresponding ranges and yielded,

$$\begin{cases} \dfrac{\Delta\sigma^2}{E^*} + \dfrac{4\Delta\sigma}{n^{*'}+1}\left(\dfrac{\Delta\sigma}{2K^{*'}}\right)^{1/n^{*'}} = \dfrac{(K_f \Delta S)^2}{E^*} \\ \Delta\varepsilon = \dfrac{\Delta\sigma}{E^*} + 2\left(\dfrac{\Delta\sigma}{2K^{*'}}\right)^{1/n^{*'}} \end{cases} \quad (5.8)$$

After the maximum stress and the ranges of strain and stress were determined for cyclic loading, the notch mean stress and notch strain amplitude could be calculated using Eqs. (5.9) and (5.10), respectively. It should be noted that Neuber's rule (Eq. (2.16)) was applied in the exact same manner as above for the ESED method to determine the notch mean stress and notch strain amplitude.

$$\sigma_m = \sigma_{max} - \Delta\sigma/2 \tag{5.9}$$

$$\varepsilon_a = \Delta\varepsilon/2 \tag{5.10}$$

As mentioned in Section 4.3.2, after the initial loading into the elastic-plastic region, the notch root material only experienced elastic deformation in subsequent loading and unloading cycles under high mean stress and high R ratio conditions. Thus the local stress ranges can be simply calculated by,

$$\Delta\sigma = K_f \Delta S. \tag{5.11}$$

Then the local strain amplitudes were directly determined using Hooke's Law,

$$\varepsilon_a = K_f \Delta S/2E. \tag{5.12}$$

The local mean stress thus can be calculated by combining Eqs. (5.9) and (5.11). In Eq. (5.9), the local maximum stress was determined by substituting the notch root

maximum strain obtained by the optical measurements into the cyclic stress-strain relationship (Eq. (4.1)). Since the cyclic creep or ratcheting occurred that resulted in a non-constant maximum strain at notch root of the testing sample, the maximum strain was taken as the average values of the recorded strains before visually detectable cracks initiated at the notch root.

### 5.3.2 Strain-Life Models

In this study, the fatigue lives of the sharply notched specimens were calculated by substituting the local stress and strain values into the mean stress strain-life models as given in Eqs. (2.35)-(2.37). The fatigue properties, $\sigma_f'$, $\varepsilon_f'$, b, and c used in the strain-life models were taken from the fully reversed strain-controlled fatigue tests. All the parameters are given in Table 4.3.

Table 5.3 presents the calculated lives of the sharply notched specimens using the local stresses and strains obtained from the ESED method and experimental strain data (considering the elastic deformation after initial loading at the notch root), along with actual lives, specimen numbers, and stress R ratios. Large differences exist between the Manson-Halford model and the other two mean stress correction models. The SWT and Morrow models give much better predictions than the Manson-Halford method.

The experimental results are plotted against the calculated lives using the ESED method for the sharply notched samples at R=0.8 and R=0.7 in a log-log scale in Figs. 5.9 and 5.10 respectively. In order to show the effects in life calculations using different notch stress-strain prediction methods, the calculated lives using Neuber's rule and the average of the two methods are also plotted in Figs. 5.9 and 5.10. As can be seen in Figs.

5.9 and 5.10, the lives calculated by the Manson-Halford model show large differences from the actual lives. However, when the experimental lives increase, the calculated lives using the Manson-Halford model tend to move close to the diagonal lines. This indicates that the Manson-Halford model gives better life predictions for long life samples than does for short life samples. The calculated lives obtained using the Morrow and SWT models are much closer to the experimental lives and less than one order of magnitude difference. The Morrow model gives a conservative prediction when fatigue life is greater than $5\times10^3$ cycles for both stress R ratios. The SWT model also provides conservative calculated lives except for the long life samples, such as #5 and #16 for R=0.8 and #10 for R=0.7. In general, the Morrow model offers better predictions than the SWT model.

As can be seen in Figs 5.9 and 5.10, the calculated lives using Neuber's rule are conservative compared with those calculated using the ESED method since Neuber's rule predicts larger notch stresses and strains than the latter. The calculated lives by the average notch stress and strain values are shorter than those determined using the ESED method. Since the average notch stress and strain values are smaller than those obtained by Neuber's rule, the calculated lives using the average values are longer to those obtained by Neuber's rule.

The calculated lives using experimental strain data and the ESED method are plotted together against the actual lives in a log-log scale in Figs. 5.11 and 5.12 for R=0.8 and 0.7 respectively. It can be seen in these figures that the calculated lives from experimental strain data and the ESED method are very close to each other for the Morrow and SWT models. The Manson-Halford model gives better prediction using

experimental strain data than using the ESED method, but the calculated lives are still far from the actual lives.

### 5.4 Summary and Discussion

Based on the life calculations, it can be concluded that the conventional S-N mean stress fatigue life models, such as the Modified Goodman, Gerber and Morrow models, cannot be used to predict the fatigue lives of the sharply notched specimens under high mean stress and high R ratio conditions since they do not take the plastic deformation into account. Although Cook and Gunn's models were developed to account for the plastic deformation of notch members, they either became invalid or yielded meaningless results under high mean stress and high R ratio conditions. Since the calculated equivalent mean stresses were found to be greater than the notched ultimate strength, the multiaxial forms of the S-N methods cannot be applied for the sharply notched specimens under high mean stress and high R ration conditions.

Among these three mean stress ε-N models, the Morrow model gave the best prediction with errors less than a factor of three and the SWT model had errors less than a factor of five. However, the Manson-Halford model yielded large errors up to four orders of magnitude since it tends to account for too much mean stress effect at short lives where mean stress relaxation may occur at high plastic strains [25].

In the ε-N life calculations, one of the potential error sources is from the extrapolation of the cyclic stress-strain curve. Due to the buckling effect at high strain amplitudes, the maximum strain amplitude used to develop the cyclic stress-strain relation was 1%. But the maximum strains in fatigue life calculations using the ε-N

models were up to 7.7%. Furthermore, the approximate analytical model used to determine the local stress-strain history also introduced errors especially at high stress levels.

It has been well documented that the total fatigue life consists of the initiation and propagation stages. The ε-N models are developed to correlate the local stress and strain with initiation life where detectable cracks exist. As mentioned in Section 4.3.2, fatigue cracks were found at the notch root from the ARAMIS© pattern images of the testing samples before final failure. The remaining lives after cracks existed at the notch root were about 20-30% of total lives that contributed to the conservative predictions by ε-N models for most specimens compared to the actual fatigue lives.

| Results / Method | $K_{t22}$ | $K_{t33}$ | % Difference From Experimental | |
|---|---|---|---|---|
| | | | $K_{t22}$ | $K_{t33}$ |
| FEA | 3.64 | 1.14 | 4.9 % | 9.6 % |
| Approximate Formulae [40] | 3.72 | N.A. | 7.2 % | N.A |
| Experimental Average | 3.47 | 1.04 | 0 % | 0 % |

Table 5.1 Stress Concentration Factors of Sharply Notched Specimen

| No. | R ratio | $S_m$(MPa) | $S_a$(MPa) | Modified Goodman ($S_u$) (cycles) | Modified Goodman ($S_{un}$) (cycles) | Gerber ($S_u$) (cycles) | Gerber ($S_{un}$) (cycles) | Morrow (cycles) | Cook (cycles) | Gunn (cycles) | Actual Life (cycles) |
|---|---|---|---|---|---|---|---|---|---|---|---|
| #11 | 0.8 | 1868 | 208 | N.A | 1 | N.A | 38 | N.A | N.A | N.A | 1857 |
| #6 | 0.8 | 1868 | 208 | N.A | 1 | N.A | 38 | N.A | N.A | N.A | 3737 |
| #2 | 0.8 | 1770 | 197 | N.A | 5 | N.A | 261 | N.A | N.A | N.A | 5817 |
| #3 | 0.8 | 1672 | 185 | N.A | 30 | N.A | 1336 | N.A | N.A | N.A | 11411 |
| #9 | 0.8 | 1573 | 175 | N.A | 139 | N.A | 5165 | 0[a] | N.A | N.A | 13687 |
| #12 | 0.8 | 1475 | 164 | N.A | 568 | N.A | 17731 | 0 | N.A | N.A | 20613 |
| #14 | 0.8 | 1278 | 142 | N.A | 7483 | N.A | 161546 | 75 | N.A | N.A | 36535 |
| #16 | 0.8 | 1082 | 120 | 4 | 84340 | 272 | 1233977 | 4869 | 40 | 1485 | 62412 |
| #5 | 0.8 | 885 | 98 | 5445 | 974605 | 210304 | 9413965 | 153519 | 84 | 3789 | 115804 |
| | | | | | | | | | | | |
| #17 | 0.7 | 1764 | 311 | N.A | 0 | N.A | 13 | N.A | N.A | N.A | 1165 |
| #7 | 0.7 | 1672 | 295 | N.A | 1 | N.A | 58 | N.A | N.A | N.A | 2800 |
| #8 | 0.7 | 1486 | 262 | N.A | 22 | N.A | 705 | 0 | N.A | N.A | 5895 |
| #15 | 0.7 | 1300 | 229 | N.A | 258 | N.A | 5812 | 2 | N.A | N.A | 10144 |
| #4 | 0.7 | 1114 | 197 | 0 | 2498 | 2 | 38999 | 116 | 10 | 141 | 18560 |
| #13 | 0.7 | 929 | 164 | 67 | 24541 | 2990 | 260666 | 3210 | 16 | 353 | 33136 |
| #10 | 0.7 | 743 | 131 | 8220 | 276838 | 198803 | 1949373 | 71662 | 30 | 997 | 57577 |

a: Calculated life less than one cycle

Table 5.2 Life Calculations using the S-N Method

| No. | R | $S_m$(MPa) | SWT (cycles) | | Morrow (cycles) | | Manson and Halford (cycles) | | Actual Life (cycles) |
|---|---|---|---|---|---|---|---|---|---|
| | | | ESED | Experiment | ESED | Experiment | ESED | Experiment | |
| #11 | 0.8 | 1868 | 3749 | 3157 | 5026 | 5086 | 2 | 14 | 1857 |
| #2 | 0.8 | 1770 | 4614 | 2702 | 5813 | 4244 | 4 | 4 | 5817 |
| #3 | 0.8 | 1671 | 5957 | 3849 | 6897 | 5707 | 7 | 15 | 11411 |
| #9 | 0.8 | 1573 | 7630 | 6105 | 8157 | 8514 | 13 | 74 | 13687 |
| #12 | 0.8 | 1475 | 10339 | 11433 | 9950 | 13327 | 25 | 225 | 20613 |
| #14 | 0.8 | 1278 | 22149 | 21761 | 16273 | 19089 | 123 | 420 | 36535 |
| #16 | 0.8 | 1082 | 63398 | 70612 | 32875 | 50472 | 954 | 4865 | 62412 |
| #5 | 0.8 | 885 | 271345 | 229402 | 103555 | 101827 | 14352 | 16607 | 115804 |
| | | | | | | | | | |
| #17 | 0.7 | 1868 | 1318 | 925 | 2430 | 2441 | 2 | 68 | 1165 |
| #7 | 0.7 | 1770 | 1559 | 1119 | 2811 | 2813 | 3 | 70 | 2800 |
| #8 | 0.7 | 1573 | 2289 | 1917 | 3899 | 4221 | 7 | 121 | 5895 |
| #15 | 0.7 | 1377 | 3644 | 3196 | 5717 | 6184 | 18 | 145 | 10144 |
| #4 | 0.7 | 1180 | 6773 | 6032 | 9306 | 9643 | 69 | 229 | 18560 |
| #13 | 0.7 | 983 | 16228 | 17073 | 18045 | 21351 | 412 | 1240 | 33136 |
| #10 | 0.7 | 787 | 63487 | 62850 | 52583 | 61465 | 5275 | 9785 | 57577 |

Table 5.3 Life Calculations using the ε-N Method

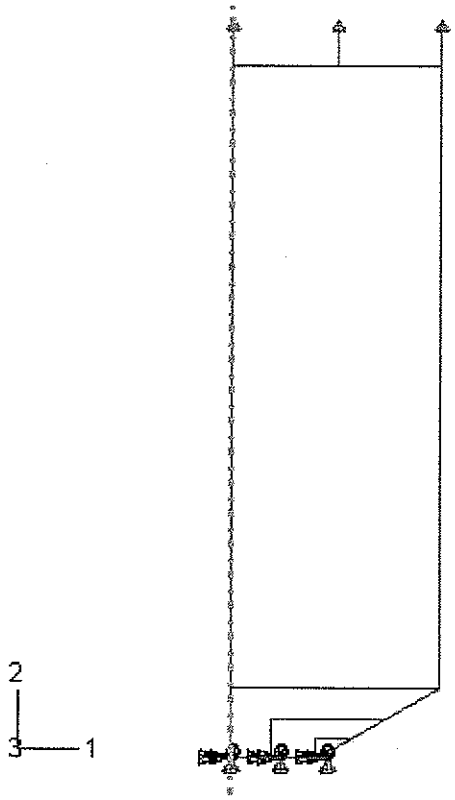


Figure 5.1 Load and Boundary Conditions of FEA Model

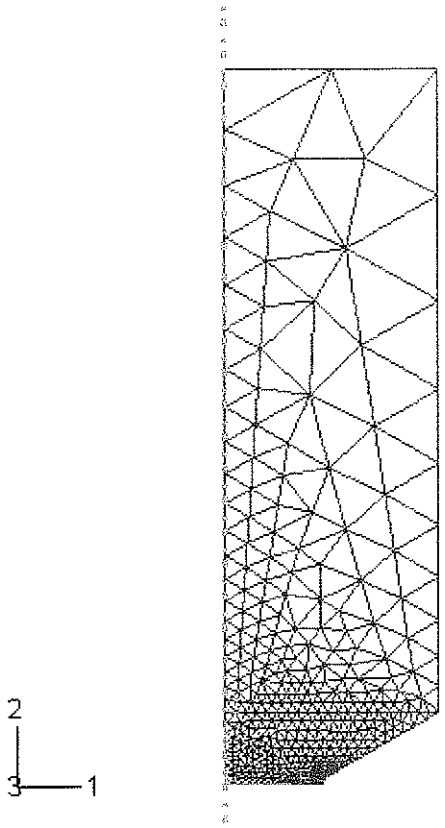


Figure 5.2 FEA Model Mesh Scheme

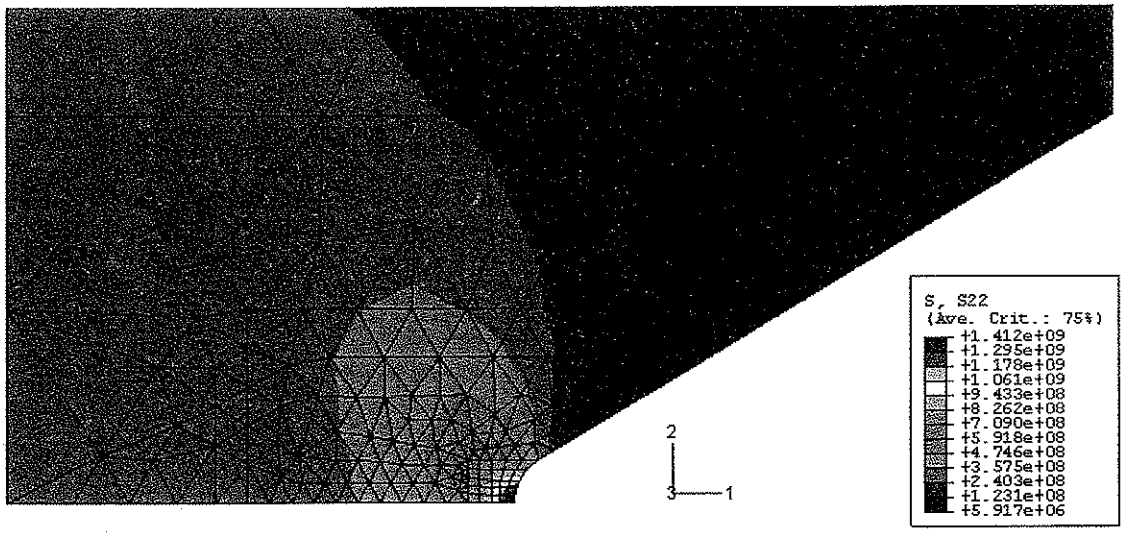


Figure 5.3 Stress Distribution Plot of FEA

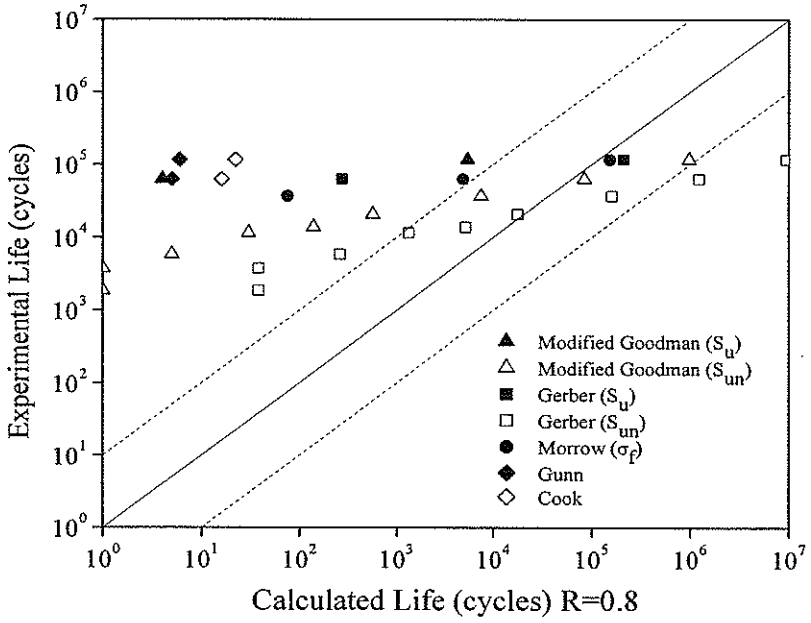


Figure 5.4 Comparison of Experimental Lives versus Calculated Lives (R=0.8, S-N)

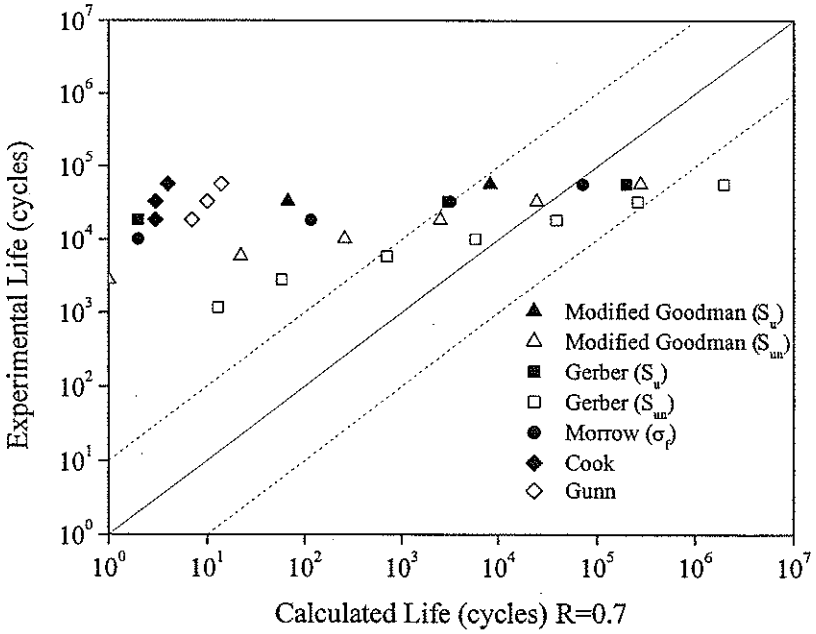


Figure 5.5 Comparison of Experimental Lives versus Calculated Lives (R=0.7, S-N)

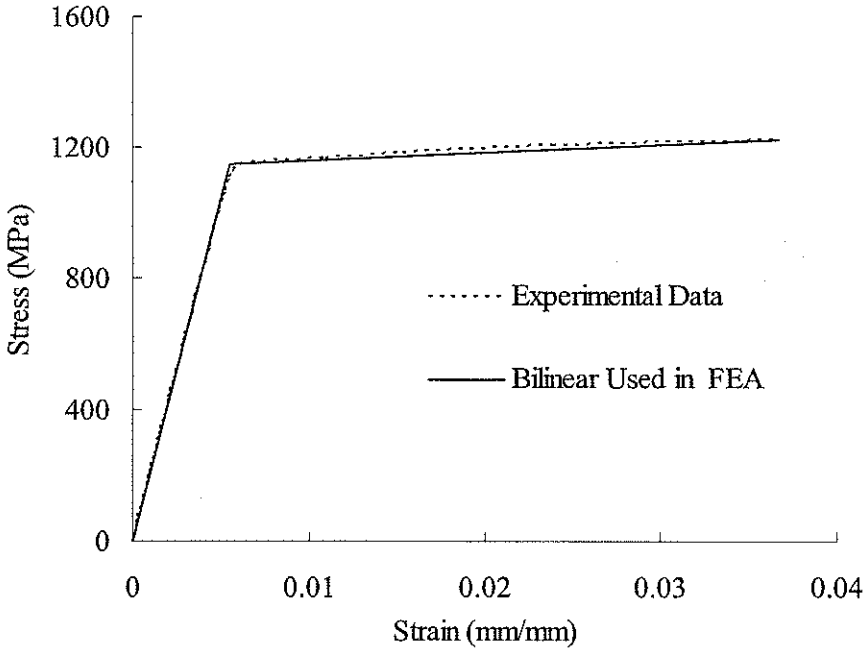


Figure 5.6 Approximate Material Law Used in FEA

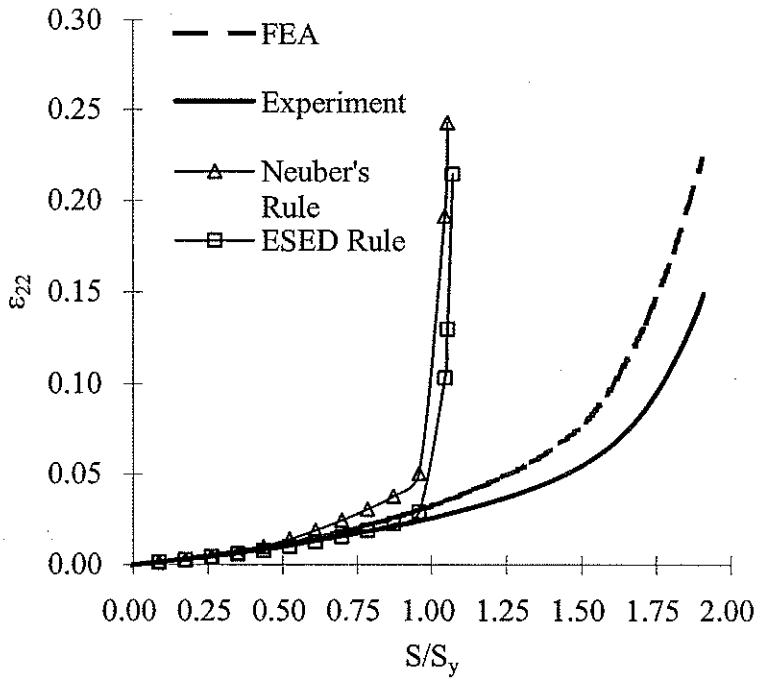


Figure 5.7 Notch Root Strain Predictions Using the Methods in [12]

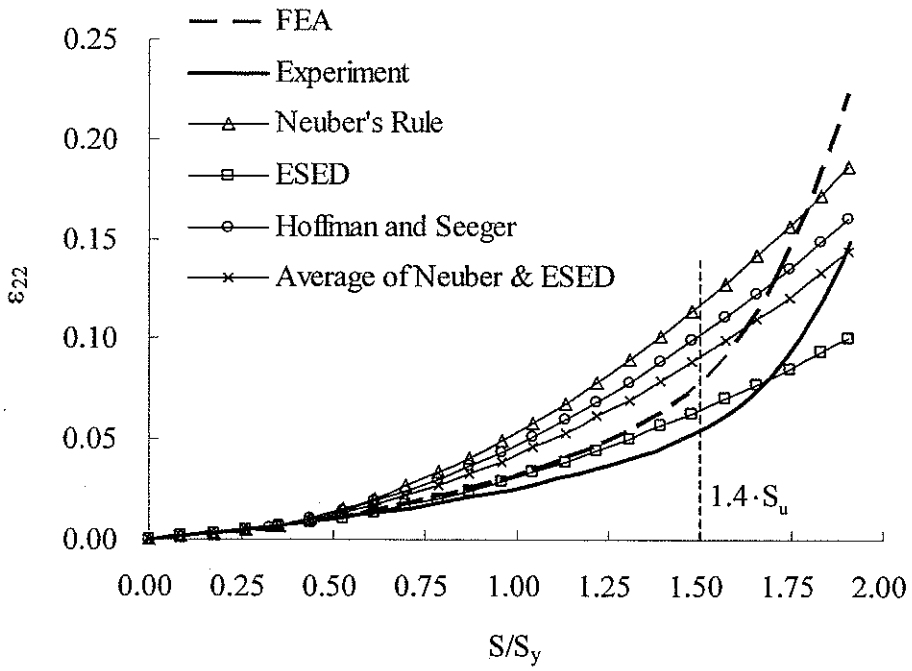


Figure 5.8 Notch Root Strain Predictions

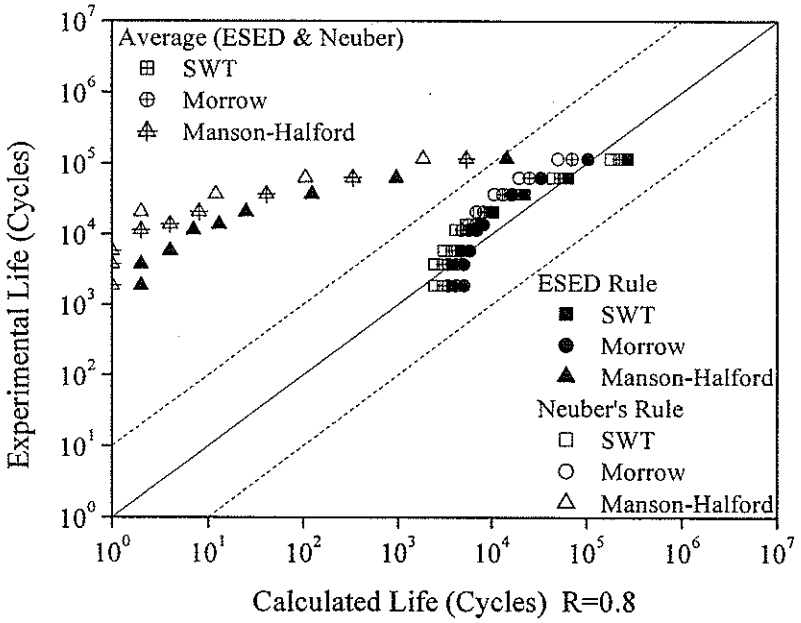


Figure 5.9 Comparison of Experimental Lives versus Calculated Lives using Analytical Approximate Method (R=0.8, ε-N)

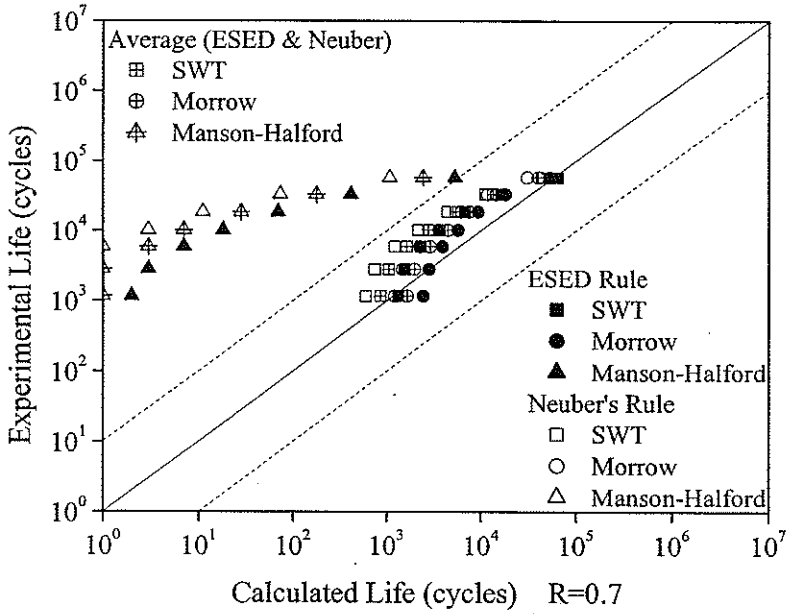


Figure 5.10 Comparison of Experimental Lives versus Calculated Lives using Analytical Approximate Methods (R=0.7, ε-N)

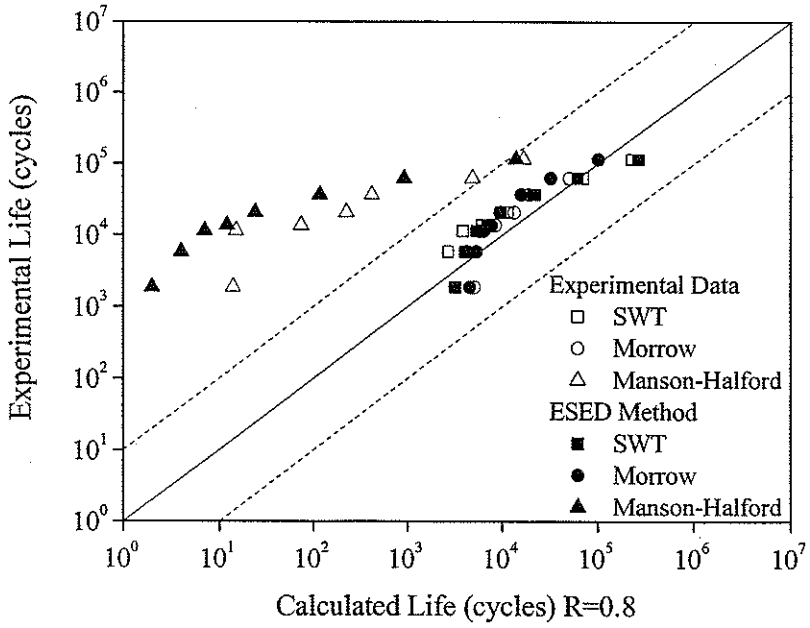


Figure 5.11 Comparison of Experimental Lives versus Calculated Lives using Experimental Data (R=0.8, ε-N)

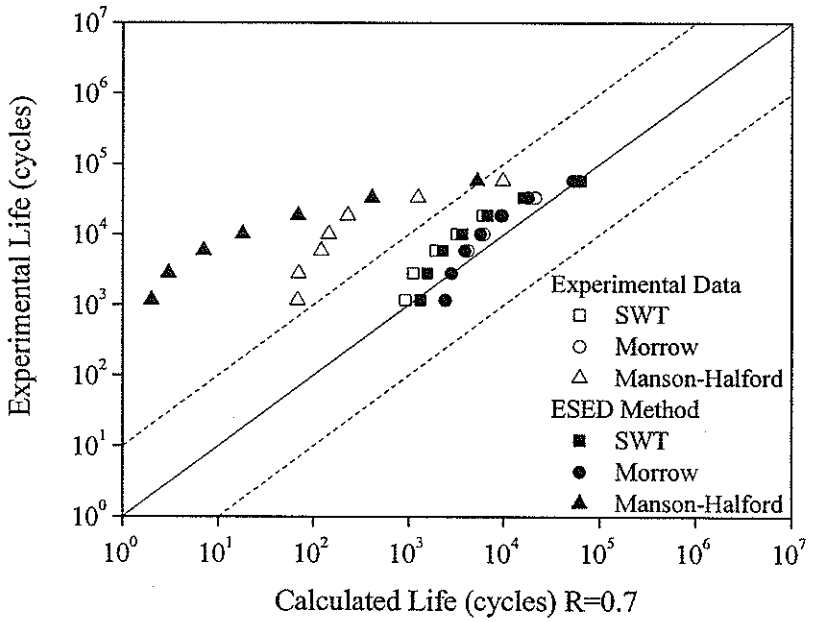


Figure 5.12 Comparison of Experimental Lives versus Calculated Lives using Experimental Data (R=0.7, ε-N)

# CHAPTER SIX

# SUMMARY, CONCLUSIONS, AND RECOMMENDATIONS

## 6.1 Summary and Conclusions

Motivated by the need in practice, this work sought to investigate the influence of high mean stress and high R ratio on the fatigue behavior of components. Specifically, this work aimed to determine whether the conventional fatigue life methods could be applied to high mean stress and high R ratio applications, a regime in which they were not previously validated. Furthermore, the SEM examinations were preformed to study the morphology of fractured notched specimens. The work consisted of an extensive literature review emphasizing the work done in the loading regime under consideration and an experimental program aimed at determining whether the conventional fatigue life methods can be applied. The work finally provided a comparison between experimental and numerical results.

The literature review emphasized that most previous work had presented high mean stress data and had not attempted to analytically predict fatigue life. The work that had been done on analytical fatigue life prediction had analyzed few of the S-N models and had concluded that they were not applicable to high mean stress and high R ratio conditions. Due to experimental and model application problems, their ε-N analysis was inconclusive.

The experimental program of this work consisted of performing monotonic tension tests on smooth and sharply notched specimens to determine the material properties of the Rc 37 SAE 1045 steel material used, and to analyze the notch root

material behavior. The program subsequently consisted of performing fatigue tests on smooth specimens at R=-1 to determine the cyclic material properties needed in life calculations. Finally, the experimental program consisted of performing two sets of tests on sharply notched specimens at R=0.7 and R=0.8.

In monotonic tension tests revealed that the Rc 37 SAE 1045 steel material used exhibits a ductile behavior and the stress strain curve is very flat after yielding. Due to the deep V-shaped notch geometry, a triaxial stress distribution exists in the plane of the notch even under uniaxial loading conditions. This results in the notched specimen having a much higher ultimate strength than that of the smooth specimen. The notch strengthening ratio was determined to be 1.8. Using the optical deformation measurement device, the nominal stress versus notch root strain curves were plotted until the specimen fracture. This was used in the evaluation of the approximate analytical techniques for determining the notch stress and strain.

The fatigue properties of the SAE 1045 steel with hardness Rc 37 were obtained experimentally by performing fully reversed ($R = -1$) strain-controlled fatigue tests. The total strain amplitudes used in the strain-control fatigue tests ranged from 0.3%-1%. It was found that buckling occurred at high strain amplitudes, greater than 1%. The transition fatigue life, $2N_t$, was found about 1415 reversals for this material with a total strain amplitude of 0.0083 mm/mm. The stabilized hysteresis loops at half life of each testing sample were used to generate the cyclic stress-strain curve. It was found that the material exhibited cyclic softening behavior that results in a 33% reduction of yield stress.

The stress-life curves of the sharply notched specimens were plotted for both stress ratios, R=0.7 and R=0.8, based on the applied alternating stress and maximum stress. The $S_a$-N and $S_{max}$-N curves for both stress ratios have similar and steep slopes.

The cyclic creep/ratcheting was investigated by monitoring the notch root maximum strains of the sharply notched specimens during the high R ratio fatigue tests. From the curves of maximum strain versus applied cycles, it was observed that cyclic creep/ratcheting occurs at both stress ratios for short-life specimens where fatigue lives are less than $10^4$ cycles. However, these curves are very flat up to about the half life for long-life specimens, and then the notch root maximum strains increased with applied cycles. Hysteresis loops of the sharply notched specimens appear as straight lines instead of open loops due to the small stress range values under high mean stress and high R ratio conditions. This indicates that the notch root material, due to the small alternating stresses, experienced elastic deformation during the cyclic loading and unloading.

Fracture surfaces of the high mean stress fatigue samples were examined by using SEM. Two different fracture modes were observed on the fracture surfaces, dimple rupture and fatigue fracture. The fracture surfaces of the monotonic tension and the short life ($<10^4$) high R ratio cyclic test specimens were very similar to each other where dimple ruptures were predominant. Fatigue striations were found at the rim region of fracture surfaces of long life samples. However, the crack propagation lives were small compared to the total lives for long life samples. This indicates that the ε-N models may be the most appropriate method to use in fatigue analysis of components under high mean stress since it is a crack initiation model.

The elastic stress concentration factors of the sharply notch specimen were determined using elastic FEA, closed formed equations, and experimental measurements. The FEA results were used in this work since the goal is to solely evaluate the analytical solution methodologies. Due to a biaxial stress state at the notch root, two stress concentration factors, $K_{t22}$ and $K_{t33}$ were determined to address the local stresses in axial and circumferential directions respectively.

Life calculations were performed using the conventional S-N mean stress models, such as the Modified Goodman, the Gerber, and the Morrow Models. In addition, Cook and Gunn's equations were also used to calculate the fatigue lives. Comparing the actual lives to those obtained from the stress-life prediction models, it is shown that all of these models yielded meaningless results and cannot be used to predict the lives of the sharply notch specimens under high mean stress and high R ratios conditions. Although the multiaxial S-N model should yield better results than that neglecting the circumferential stress, the calculations could not be performed since the calculated equivalent mean stresses were found to be greater the notched ultimate strength.

To perform the life calculations using ε-N models, the different approximate analytical approaches were first used to define the elastic-plastic notch root strains and the results were compared with FEA and experimental data. It was found that the ESED method provided better results than Neuber's rule or Hoffmann and Seeger model, but the results may be unique to this geometry. Although the Hoffmann and Seeger model was developed to account for large-scale yielding, it necessitates a non-linear FEA for application. It is felt that Neuber's rule and the ESED method could be used together in design since they do predict a band within which the FEA results fall. The strain-life

models including the Morrow, Manson-Halford, and SWT models were used for life calculations. Among the three mean stress strain-life models, the Morrow and SWT models gave good correlation with actual lives. On the contrary, the Manson-Halford model took too much mean stress effect at high plastic conditions and resulted in large errors in life calculations. Though the Morrow and SWT models exhibited a good agreement with experimental data, errors existed at short-life specimens with very high mean stresses, where the cyclic creep/ratcheting occurred. Furthermore, the local stress-strain history determined from the extrapolated Ramberg-Osgood relation also introduced errors especially at high mean stress levels.

### 6.2 Recommendations for Future Work

1 Fully reversed strain-controlled tests should be conducted at higher strain amplitudes, greater than 1%, to obtain more accurate fatigue properties.

2 Further investigation into the cyclic creep/ratcheting that occurs at high mean stresses would be required to incorporate such effects into ε-N life prediction models.

3 The influence of high mean stress and high R ratio on different materials may be investigated.

4 Crack growth tests should be performed to investigate the crack growth behavior under high mean stress and high R ratio conditions.

5 The fatigue behavior of components under high mean stress and high R ratios should be investigated under variable amplitude loading conditions.

# REFERENCES


1. Forrest, P.G., "Fatigue of Metals," Pergamon Press Ltd., London, 1962.

2. Bell, W. J. and Benham, P. P., "The Effect of Mean Stress on Fatigue Strength of Plain and Notched Stainless Steel Sheets in the Range from 10 to $10^7$ Cycles," Symposium on Fatigue Tests of Aircraft Structures: Low-Cycle, Full-Scale, and Helicopters, STP No. 338, American Society for Testing and Materials, Philadelphia, PA, 1962, pp. 25-46.

3. Stephens, R. I., Fatemi, A., Stephens, R. R., and Fuchs, H. O., "Metal Fatigue in Engineering," 2nd ed., Wiley-Interscience, New York, 2000.

4. Landgraf, R.W., "The Resistance of Metals to Cyclic Deformation," Achievement of High Fatigue Resistance in Metals and Alloy, ASTM STP 467, ASTM, West Conshohocken, PA, 1970, pp. 3.

5. Basquin, O. H., "The Exponential Law of Endurance Tests," Proc. ASTM, Vol. 10, Part 11, 1910, ASTM, West Conshohocken, PA, pp. 625-630.

6. Pilkey, W. D., "Peterson's Stress Concentration Factors," 2nd ed., John Wiley and Sons Inc., New York, 1997.

7. Cook, N. H., "Mechanics and Materials for Design," McGraw-Hill, New York, 1985.

8. Gunn, K., "Effect of Yielding on The Fatigue Properties of Test Pieces Containing Stress Concentrations," Aeronaut, Q., 1955, Vol.6, No. 4, pp.227-294.

9. Burguete, R. L. and Patterson, E. A., "The Effect of Mean Stress on The Fatigue Limit of High Tensile Bolts," Proc Instn Mech Engrs, Part C: Journal of Mechanical Engineering Science, Vol. 209, pp.257-262, 1995.

10. Vantiger T., "The Influence of High R ratio on Notched Fatigue behavior of 1045 Steel with three Different Heat Treatments," Masters Thesis, The University of Iowa, May 2001.

11. Karadag, M., "The Influence of High R Ratio on Smooth Fatigue Behavior of1045 Steel With Three Different Heat Treatments," Masters Thesis, The University of Iowa, May 2001.

12. Pals, T., "The Influence of High R Ratio on Sharply Notched Fatigue Behavior of 1045 Steel With Three Different Heat Treatments," Masters Thesis, The University of Iowa, May 2002.

13. Morrissey, R. J., McDowell, D. L., and Nicholas, T., "Frequency and Stress Ratio Effects in High Cycle Fatigue of Ti-6Al-4V," International Journal of Fatigue, Vol. 21, 1999, pp.679-685.

14. Maxwell, D. C., and Nicholas, T., "A Rapid Method for Generation of Haigh Diagram for High Cycle Fatigue," Fatigue and Fracture Mechanics, Vol. 29, ASTM STP 1332, Panontine, T. L. and Sheppard, S. D. Eds., American Society for Testing and Materials, West Conshohocken, PA, 1999, pp. 626-641. H. Neuber, "Theory of Stress Concentration for Shear-Strained Prismatical Bodies with Arbitrary Nonlinear Stress-Strain Laws," J. Appl. Mech., Trans. ASME, Vol. E28, 1961, pp. 544.

15. Neuber, H., "Theory of Stress Concentration for Shear-Strained Prismatical Bodies with Arbitrary Nonlinear Stress-Strain Laws," J. Appl. Mech., Trans. ASME, Vol. E28, 1961, P. 544.

16. Topper, T. H., Wetzel, R. M., and Morrow, J. D., "Neuber's Rule Applied to Fatigue of Notched Specimens," J. Materials, JMSLA, Vol. 4. No.1, 1969, pp. 200.

17. Molski, K. and Glinka, G., "A Method of Elastic-Plastic Stress and Strain Calculation at a Notch Root," Mat. Sci. Eng., Vol. 50, 1981, pp. 93-100.

18. Dowling, N., Brose, W. R., and Wilson, W. K., "Notched Member Fatigue Life Predictions by the Local Strain Approach," Fatigue under Complex Loading, Vol. 6 of Advances in Engineering, R. M. Wetzel (editor), Society of Automotive Engineers, Warrendale, PA, 1977, pp 55-84.

19. Singh, M. N .K., "Notch Tip Stress Strain Analysis in Bodies Subjected to Non-Proportional Cyclic Loads," Ph.D. Thesis, The University of Waterloo, Ontario, 1998.

20. Hoffmann, M. and Seeger, T., "A Generalized Method for Estimating Elastic-Plastic Notch Stresses and Strains, Part 1: Theory," Journal of Engineering Materials and Technology, Vol. 107, 1985, pp. 250-254.

21. Hoffmann, M. and Seeger, T., "A Generalized Method for Estimating Elastic-Plastic Notch Stresses and Strains, Part 2: Applications," Journal of Engineering Materials and Technology, Vol. 107, 1985, pp. 255-260.

22. Coffin, L. F., Jr., "A Study of the Effects of Cyclic Thermal Stresses on a Ductile Metal," Trans. ASTM, Vol. 76, 1954, pp. 931-950.

23. Manson, S. S., "Behavior of Materials under Conditions of Thermal Stress," Heat Transfer Symposium, University of Michigan Engineering Research Institute, 1953, pp. 9-75.

24. Morrow, J., "Fatigue Design Handbook," Advances in Engineering, Vol. 4, Society

of Automotive Engineers, Warrendale, Pa., 1968, Sec. 3.2, pp. 21-29.

25. Bannantine, J. A., Comer, J. J., and Handrock, J. L., "Fundamentals of Fatigue Analysis," Prentice Hall, New Jersey, 1990.

26. Manson, S. S. and Halford, G.R., "Practical Implementation of the Double Linear Damage Rule and Damage Curve Approach for Treating Cumulative Fatigue Damage," International Journal of Fracture, Vol. 17, No. 2, 1981, pp. 169-172.

27. Smith, K. N., Watson, P., and Topper, T. H., "A Stress-Strain Function for the Fatigue of Metals," Journal of Materials, Vol. 5 No. 4, Dec. 1970, pp.767-778.

28. Xia, Z., Kujawski, D. and Ellyin, F., "Effect of Mean Stress and Ratcheting Strain on Fatigue Life of Steel," International Journal of Fatigue, Vol 18, No. 5, 1996, pp 335-341.

29. ASM Handbook. "Properties and Selection: Irons, Steels, and High-Performance Alloys," ASM International, Vol. 01, Materials Park, OH, 1991, pp. 140-194.

30. Standard E 08, "Standard Test Methods for Tension Testing of Metallic Materials," 2000 Annual Book of ASTM Standards, Vol. 03.01, American Society for Testing and Materials, West Conshohocken, PA, 2000, pp. 56-98.

31. Standard E606, "Standard Practice for Strain-Controlled Fatigue Testing," 2000 Annual Book of ASTM Standards, Vol. 03.01, American Society for Testing and Materials, West Conshohocken, PA, 2000, pp. 525-539.

32. Shigley, J. E. and Mischke, C. R., "Mechanical Engineering Design," 5th ed., McGraw Hill, New York, 1989.

33. VEE OneLab User's Guide, 1st March, 2000, Agilent Technologies Inc.

34. Standard E1012, "Standard Practice for Verification of Specimen Alignment Under Tensile Loading," 2000 Annual Book of ASTM Standards, Vol. 03.01, American Society for Testing and Materials, West Conshohocken, PA, 2000, pp. 725-732.

35. The Optical Deformation Measurement Device Instruction Manual, "Deformation Measurement Using the Grating Method," 2001, GOM mbH, Braunschweig.

36. Landgraf, R. W., Morrow, J., and Endo, T., "Determination of the Cyclic Stress-Strain Curve," J. Mater., Vol. 4, No. 1, 1969, pp. 176.

37. Dowling, N.E., "Mechanical Behavior of Materials: Engineering Methods for Deformation, Fracture and Fatigue," 2nd ed., Prentice-Hall, Inc., 1999.

38. ASM Handbook. "Fractography," ASM International, Vol. 12, Metals Park, OH, 1987.

39. Donald J. Wulpi, "Understanding How Components Fail," American Society For Metals, July 1985.

40. Noda, N. A. and Takase, Y., "Stress Concentration Formulae Useful for Any Shape of Notch in A Round Test Specimen Under Tension and Under Bending," Fatigue Fract.Engng Mater Struct , Vol. 22, pp.1071-1082.

41. ABAQUS/CAE User's Manual 6.31, 2003 ABAQUS, Inc.